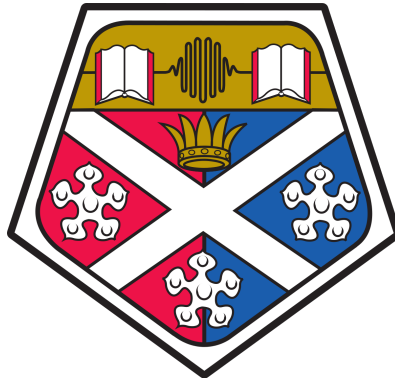


Chip-Scale Atomic Magnetometer Based on Free-Induction-Decay

Dominic Hunter

A thesis presented for the degree of
Doctor of Engineering



Department of Physics
University of Strathclyde

2019

This thesis is the result of the author's original research. It has been composed by the author and has not been previously submitted for examination which has led to the award of a degree.

The copyright of this thesis belongs to the author under the terms of the United Kingdom Copyright Acts as qualified by University of Strathclyde Regulation 3.50. Due acknowledgement must always be made of the use of any material contained in, or derived from, this thesis.

Signed: 

Date: April 4, 2019

Abstract

This thesis describes the implementation of an optically pumped caesium magnetometer containing a 1.5 mm thick microfabricated vapour cell with nitrogen buffer gas, operating in a free-induction-decay configuration. This allows us to monitor the free Larmor precession of the spin coherent Cs atoms by separating the pump and probe phases in the time domain. A single light pulse can sufficiently polarise the atomic sample; however, synchronous modulation of the light field actively drives the precession and maximises the induced spin coherence. Both amplitude- and frequency-modulation have been adopted producing noise floors of $3.4 \text{ pT}/\sqrt{\text{Hz}}$ and $15.6 \text{ pT}/\sqrt{\text{Hz}}$, respectively, within a Nyquist limited bandwidth of 500 Hz in a bias field comparable to the Earth's ($\sim 50 \mu\text{T}$). We investigate the magnetometers capability in reproducing time-varying magnetic signals under these conditions, including the reconstruction of a 100 pT perturbation using signal averaging.

Additionally, we discuss a novel detection mode based on free-induction-decay that observes the spin precession dynamics in-the-dark using Ramsey-like pulses. This aids in suppressing the systematic effects originating from the light-atom interaction during readout, thus vastly improving the accuracy of the magnetometer whilst maintaining a sensitivity that is competitive with previous implementations. This detection technique was implemented further to measure the spin relaxation properties intrinsic to the sensor head, useful in determining the optimal buffer pressure that extends the spin lifetime and improves the sensor's sensitivity performance.

Acknowledgements

First and foremost, I would like to extend my sincerest gratitude to my academic supervisor *Erling Riis* for providing me with the opportunity to explore this deeply interesting project; his advice and support throughout has been invaluable and allowed me to develop as a scientist and a professional. The work presented here and resulting publications would not have been possible without his constant guidance.

I would like to sincerely thank my industrial supervisor *Terry Dyer* who has been a great resource and a pleasure to work with. He has always been available to deliver his advice when necessary in a supportive and constructive manner. The belief that both supervisors have shown with regards to my research was crucial in my success as an EngD student and an intern at Texas Instruments (TI), and I thank them both for their roles in this endeavour. I would also like to extend my gratitude to *Savino Piccolomo* for his contribution to the project and help during the initial stages.

I would like extend my appreciation to TI for their funding and support throughout the duration of the project, and providing me with the internship opportunity in Dallas. This allowed me to grow both personally and professionally, and was a truly rewarding experience. I would like to thank all my colleagues at TI for their support during the internship. In particular, I would like to thank *Ann Gabrys* who was a great mentor during my time at TI. Also, I would like to extend my appreciation to *Juan Herbsommer*, and *Ricardo Jiménez-Martínez* for their assistance and many valuable discussions.

I would like to acknowledge all my colleagues at the University of Strathclyde for creating such an enjoyable working environment. It has been a privilege to work with so

many talented individuals who are always available to help when needed. In particular, I would like to thank *Jonathan Pritchard*, *Paul Griffin*, and *Stuart Ingleby* who have been an invaluable resource in the department.

Finally, I would like to thank my family and friends who have always been supportive of my decision to pursue a career in physics. Completing this EngD has been an extremely rewarding, and challenging, experience that has been made easier by those close to me. I would like to give a special thanks to my fiancée who has never hesitated to embark on this adventure with me even during the most difficult times.

Contents

Abstract	i
Acknowledgements	ii
Table of Contents	iv
List of Figures	vii
List of Acronyms	x
1 Introduction	1
2 General Magnetometry Theory	12
2.1 Light-Atom Interactions	12
2.1.1 Energy structure of an alkali-metal atom	12
2.1.2 Absorption cross-section	14
2.1.3 Optical resonance lineshape	16
2.1.4 Optical pumping	19
2.2 Microfabricated Vapour Cell Technology	22
2.2.1 Vapour cell fabrication	22
2.2.2 Buffer gas effects	24
2.2.3 Spectroscopic testing	26
2.3 Atomic Interactions with Static Magnetic Fields	27
2.3.1 Larmor precession	27
2.3.2 Zeeman effect	29

Contents

2.4	Spin Relaxation	33
2.4.1	Depolarising mechanisms	33
2.4.2	Light narrowing	37
3	Free-Induction-Decay Magnetometry	41
3.1	Principles of Operation	42
3.2	Experimental Set-up	44
3.3	Signal Processing	47
3.3.1	FID signal sampling	47
3.3.2	Discrete Fourier transform	49
3.3.3	Reliability of the fitting routine	50
3.3.4	Noise estimation	52
3.3.5	Cramér-Rao lower bound: frequency estimation	55
3.3.6	Zero-crossing frequency extraction	58
3.3.7	Damping rate estimation	63
3.4	Detection of Spin Precession	64
3.4.1	Optical polarimetry	64
3.4.2	Absorptive vs. dispersive measurements	67
3.4.3	Light shift systematics	69
3.5	Optical Pumping	72
3.5.1	Modulation techniques	72
3.5.2	Optimisation of pumping parameters	75
3.5.3	Potential systematics based on operating conditions	78
3.6	Frequency-Modulation Scheme	80
3.6.1	Experimental set-up	80
3.6.2	Pump frequency optimisation	82
3.7	Sensitivity Analysis: AM vs. FM	83
4	Waveform Tracking with a FID Magnetometer	87
4.1	Experimental Methodology	88
4.2	Waveform Reconstruction of AC Magnetic Signals	90

Contents

4.3	Technical Considerations	94
4.4	Unshielded Operation	96
5	Suppression of Operational Systematics	100
5.1	Probing In-The-Dark	101
5.1.1	Principle of operation	101
5.1.2	Optical pumping spin dynamics	105
5.1.3	Light-shift suppression	109
5.1.4	Sensitivity analysis	113
5.2	Measurement of Intrinsic Spin Lifetime	116
5.2.1	Ground state coherence measurement techniques	116
5.2.2	Buffer gas pressure estimation	120
5.2.3	Transverse relaxation rate measurements	121
6	Conclusion and Outlook	126
	Appendices	130
A.1	Alkali number density	130
B.1	Reduced dipole matrix element	131
B.2	Numerical approximation of the Voigt profile	132
C.1	Signal Noise Estimation Algorithm	133
C.2	Cramer-Rao Lower Bound	134
	Bibliography	135

List of Figures

1.1	Simple atomic magnetometer design	9
2.1	Energy structure of Cs: D_1 and D_2 transitions	13
2.2	Voigt profile and validity of numerical approximation	18
2.3	Optical pumping of a spin-1/2 system	20
2.4	Fabrication of MEMS Cs cells	23
2.5	Effect of buffer gas on optical spectrum	25
2.6	Spectroscopic testing of MEMS Cs cells	26
2.7	Breit-Rabi diagram	30
2.8	Spin-exchange collisions	35
2.9	Repumping of $F = 3$ hyperfine manifold	39
3.1	FID magnetometer principles of operation	42
3.2	Modulation techniques	43
3.3	Schematic of experimental arrangement	45
3.4	Photograph of laboratory	46
3.5	Simulated FID signal corrupted by additive white Gaussian noise	48
3.6	Fitting quality of experimental FID traces to DS model	51
3.7	FID signal train: noise estimation	53
3.8	Noise estimation algorithm test	55
3.9	Cramér-Rao lower bound comparison	57
3.10	Zero crossings: detecting spurious contributions	59
3.11	Zero crossings: interpolation procedure	60

List of Figures

3.12	Zero crossings: sensitivity comparison with fitting routine	61
3.13	Damping rate estimation with exponential envelopes	63
3.14	Balanced polarimetry noise suppression	66
3.15	Comparison between optical rotation and transmission based detection .	67
3.16	Sensitivity performance of detection techniques	68
3.17	AC Stark shift frequency detuning dependence	70
3.18	Synchronous vs. single-pulse optical pumping	73
3.19	Single-pulse modulation: pump duration dependence	74
3.20	Pump power dependence	76
3.21	Synchronous modulation: duty cycle dependence	77
3.22	Spin polarisation build-up	78
3.23	Systematics induced by variations in optical pumping conditions	79
3.24	VCSEL data	81
3.25	FM pump frequency optimisation	83
3.26	Example FID traces acquired using AM and FM	84
3.27	Sensitivity comparison: AM vs. FM	85
4.1	Sensitivity to time-varying magnetic signals	90
4.2	Measurement of 100 pT field oscillation	91
4.3	Demonstration of detector linearity	92
4.4	FID magnetometer frequency response	93
4.5	Measurement of strong oscillating fields: FM effects	95
4.6	Unshielded magnetic field measurement	97
5.1	Dual modulation experimental set-up	102
5.2	Probing in-the-dark principle of operation	103
5.3	Optical pumping effects on angle of spin vector	106
5.4	FID signal dependence on frequency detuning	108
5.5	Reconstruction of precession signals at varying readout intensities	110
5.6	Probing in-the-dark intensity dependence	111
5.7	Suppression of probe systematics	112

List of Figures

5.8	Probing in-the-dark sensitivity analysis	114
5.9	Measurement of γ_{20} : extrapolation to zero-light power	117
5.10	Measurement of γ_{20} : probing in-the-dark	119
5.11	Optical spectra of MEMS Cs cells	120
5.12	Intrinsic relaxation rate temperature dependence	122
5.13	Intrinsic relaxation rate buffer gas pressure dependence	124

List of Acronyms

- AC** Alternating current. 7
- AM** Amplitude-modulation. 41
- AOM** Acousto-optic modulator. 45
- CRLB** Cramér-Rao lower bound. 42
- CSAM** Chip-scale atomic magnetometer. 8
- DC** Direct current. 45
- DFT** Discrete Fourier transform. 49
- DS** Damped sinusoidal. 49
- EOM** Electro-optic modulator. 46
- FFT** Fast Fourier transform. 50
- FID** Free-induction-decay. 6
- FM** Frequency-modulation. 41
- FPGA** Field-programmable gate array. 59
- FWHM** Full width at half maximum. 17
- LM** Levenberg-Marquardt. 27

List of Acronyms

MCG	Magnetocardiography.	1
MEG	Magnetoencephalography.	1
MEMS	Microelectromechanical systems.	9
NMR	Nuclear magnetic resonance.	42
OPM	Optically pumped magnetometer.	1
PBS	Polarising beam splitter.	9
PID	Proportional-integral-derivative.	81
PITD	Probing in-the-dark.	101
RF	Radio frequency.	46
RMS	Root mean square.	48
RSD	Root spectral density.	42
SERF	Spin-exchange relaxation-free.	5
SNR	Signal-to-noise ratio.	3
SQUID	Superconducting quantum interference device.	5
TIA	Transimpedance amplifier.	67
VCSEL	Vertical-cavity surface-emitting laser.	3
ZC	Zero-crossing.	59

Chapter 1

Introduction

Magnetic field detection has been practised for many centuries, particularly in navigation with the implementation of compasses. The first magnetometry instrument was invented by Carl Friedrich Gauss in 1832 and consisted of a bar magnet suspended from a gold fibre that was originally used to measure the Earth's magnetic field [1]. Technology has advanced considerably since then with devices such as Hall probes, fluxgates, and magnetometers based on proton precession or the Overhauser effect now commercially available [2]. Optically pumped magnetometers (OPMs) enable far superior accuracy and sensitivities than many previously adopted systems and are highly versatile with various operational schemes available, each possessing their own unique characteristics and strengths that can be tailored toward target applications. Sensitive detection of ultra-low magnetic fields is of great importance in many areas of fundamental and applied research including the analysis of biological signals such as magnetocardiography (MCG) [3] or magnetoencephalography (MEG) [4], non-destructive testing of materials [5], geomagnetic and archaeological prospecting [6], space exploration [7], and experiments seeking the fundamental symmetries of Nature [8].

OPMs provide an extremely sensitive method of magnetic field detection, utilising interactions of resonant light with a magnetically sensitive atomic vapour [9]. Advancements in optical pumping techniques aid in maintaining long-lived spin polarisation in the ground state manifold, such that the coherent spins can undergo Larmor precession which quantifies the response of an atomic medium to an external magnetic field

\vec{B} [10]. The respective interaction with the atoms magnetic moment $\vec{\mu}$ can be thought of classically as the precession of the component of angular momentum transverse to \vec{B} at the angular frequency ω_L . This can also be interpreted quantum mechanically as the Zeeman shift induced by the magnetic field where $\omega_L/2\pi$ is equivalent to the frequency spacing between magnetic sublevels. The magnitude of the magnetic field, $|\vec{B}| = B_0$, can then be inferred directly from the precession rate of the polarised spins in the following way,

$$\omega_L = \gamma|\vec{B}|, \quad (1.1)$$

where the gyromagnetic ratio γ is a known conversion factor dependent on the atomic species. The spin dynamics associated with the precession and relaxation can also be viewed as an oscillation and decoherence of atomic population among the ground state Zeeman sublevels. This alters the absorptive and dispersive properties of the medium that can be measured precisely by monitoring variations in the intensity or polarisation of light transmitted through the sample.

Developments in microfabricated vapour cell technology and the introduction of robust, scalable, inexpensive, tunable diode lasers have assisted in prolonging ground state relaxation times to that necessary for precision metrology [2]. This has stimulated numerous, unexplored, applicable domains that remained elusive to competing technologies incompatible with miniaturisation. Millimetre-sized vapour cells can be constructed using fairly standard methods; however, microfabrication requires highly developed production techniques well-known to the semiconductor industry [11]. Silicon wafer technology provides a reliable, consistent, and high-throughput method of constructing vapour cells that can be easily integrated into a packaged device, in comparison to traditional glass-blown cells [12]. The miniaturised nature of microfabricated magnetometers introduces numerous advantages, such as reduced power consumption, portability, and low fabrication cost, whilst maintaining a higher level of performance than existing technologies of similar size and power requirements [13]. In particular the high-volume, wafer-based production yields an order of magnitude reduction in pro-

duction costs without sacrificing device performance. Although many glass-blown cells can be operated at room temperature, effectively removing the need for heating that is required in miniaturised cells to achieve an appreciable absorption, they are limited in terms of manufacturability and also scalability, resulting in poor spatial resolution if applied to potential sensor networks [14]. Also, effective heat-loss management can dramatically reduce the power required to heat these microfabricated devices to as low as 11 mW [15]. Vertical-cavity surface-emitting lasers (VCSELs) tend to be the light source implemented in chip-scale manufacturing, primarily as they are scalable, consume low power, and can be tuned resonantly with the D-lines of caesium (Cs) or rubidium (Rb) which are the most commonly used alkali-metals in OPMs. Potassium (K) can also be a useful working substance as the Zeeman resonances are more easily resolved thus produce correspondingly smaller heading errors [1]. Sensitive chip-scale magnetometers are particularly desirable in medical imaging applications where magnetic source localisation is performed with sensor arrays.

There are numerous performance characteristics that dictate a sensor's capability in specified applications. The most renowned is the sensitivity as this determines the smallest magnetic field variation resolvable by the magnetometer. Noise can degrade a magnetometer's precision which is often limited by technical sources, for instance, intensity or polarisation fluctuations in the light source, and background magnetic field variations. Technical noise typically has a $1/f$ frequency dependence with noise peaks localised at 50 or 60 Hz, and associated harmonics, arising from the power lines and surrounding equipment. From a phenomenological perspective, the magnetometer sensitivity is dependent on the signal-to-noise ratio (SNR) and linewidth of the magnetic resonance hence it is important to ensure noise contributions are minimised [16]. The SNR can also be enhanced by interacting with more atoms, realised experimentally by increasing the vapour density or using large cell volumes. This also improves the fundamental sensitivity limit that is ultimately governed by quantum-mechanical effects such as fluctuations in the measurement of atomic spin projection. The atom

shot-noise-limited precision is given by the expression [17],

$$\delta B_{sn} \approx \frac{1}{\gamma} \sqrt{\frac{\gamma_2}{N\tau}}, \quad (1.2)$$

where γ_2 is the relaxation rate of the spins proportional to the magnetic resonance linewidth, N is number of atoms, and τ is the total measurement time. The magnetic field resolution given in Eq. (1.2) can be expressed in units of sensitivity by dividing by the square root of the measurement bandwidth, defined as $f_{bw} = 1/2\tau$. It is immediately observable that one should try and maximise the spin-coherence lifetime and number of atoms involved in the interaction to improve the sensor resolution. Another source of quantum-mechanical fluctuation is concerned with the probing light used to readout the precession signal, known as photon shot noise. If the spin precession is detected by monitoring optical rotation in the plane of transmitted light polarisation, then the uncertainty in the measured rotation angle scales as,

$$\delta\varphi \approx \frac{1}{2\sqrt{N_{ph}}}, \quad (1.3)$$

where N_{ph} is the total number of photons incident on the detection system [18]. It can be seen that higher light levels reduce this noise; however, will simultaneously increase the magnetic linewidth through power broadening and potentially degrade the sensitivity performance. Also, having large optical intensities incident on a photodiode generates high currents that increase the shot noise level in the detection electronics. It should be noted that intensity, or polarisation, noise in the light source materialise as fictitious variations in the magnetic field caused by light shifts that could limit the sensor resolution, especially at elevated light intensities [19]. In the absence of other technical noise sources, optimal operation would require lowering the photon noise level to below the atom shot noise limit. OPMs have been operated close to these fundamental limits, one example showing SNRs in excess of 10^5 in a 1 Hz measurement bandwidth [20].

The inherent properties of the sensing element are crucial in determining the magnetometer's performance and its compatibility toward potential applications. For exam-

ple, some areas of research require a high sensitivity or accuracy, extended bandwidth, reduced size and portability, or a low-cost device which is all contingent on the vapour cell. Sensitive magnetometry measurements require polarising an atomic ensemble to induce phase coherence into the spin system. This can be difficult especially in miniaturised devices as depolarising collisions with the vapour cell walls actively destroys built-up coherence. To circumvent this issue one can apply cell coatings, such as paraffin, allowing thousands of collisions prior to depolarisation. These substances do have certain fabrication and operational limitations, especially at elevated temperatures; however, this is still an actively researched field [21]. Alternatively, an inert buffer gas can be added to slow down atomic diffusion thus prolonging the spin-coherence lifetime. This also induces collisional broadening of the resonance spectrum that considerably alters the optical pumping dynamics as many atomic states can be pumped and probed simultaneously, analogous to many early magnetometry experiments that implemented broadband light sources. Additional buffer gas substances introduce further contributions to spin relaxation through collisions with the gas molecules thus the pressure can be adjusted to balance these competing effects and maximise the coherence lifetime for a given cell geometry. Spin depolarisation can also originate from alkali-alkali collisions that exist in two types: spin exchange that preserves the total atomic spin, and the less frequent spin-destruction collisions that completely randomise the atomic polarisation. In optimising magnetometer performance one can utilise mechanisms that suppress spin exchange, such as the well-known spin-exchange relaxation-free (SERF) or light-narrowing phenomena enabling considerable sensitivity enhancement.

The leading high-precision magnetometer for weak magnetic field detection in recent times has been the superconducting quantum interference device (SQUID); however, the most sensitive OPMs operating in the SERF regime compete well with their SQUID counterparts, recording a best sensitivity of $160 \text{ aT}/\sqrt{\text{Hz}}$ [22]. Small-scale vapour cells promote certain problems in OPMs as the sensitivity scales with the number of atoms used to perform the measurement as seen in Eq. (1.2). The high atomic density necessary for optimal performance induces additional relaxation contributions from the increased alkali-alkali collisions, thereby affecting the sensitivity of the device [23]. SERF

magnetometers eliminate this effect by suppressing spin-exchange collisions, when operating near zero magnetic field at high atomic densities, that aids in maintaining narrow magnetic resonance linewidths. However, a shielded environment or active field compensation is necessary to null the ambient field that would otherwise saturate the sensor, as well as significant power requirements for cell heating. SERF sensors are fundamentally limited by spin-destruction collisions, hence the extensive use of Rb and K with their smaller collisional cross-sections in comparison to Cs [1]. The resulting narrow magnetometer linewidth will dramatically improve the sensitivity at the expense of a considerably limited bandwidth (typically < 100 Hz) compared to other microfabricated atomic sensors with relaxation rates in the kHz range.

The sensitivity of many OPM systems is limited by spin-exchange collisions; therefore, Cs is often the choice of atomic species in OPMs due to its simple resonance structure and higher vapour pressure that lowers the power requirements. Total field sensors including the free-induction-decay (FID) [24], Bell-Bloom [25], and M_x [20] implementations, have a relatively large dynamic range enabling operation in Earth-field conditions at pT-level resolution depending on the vapour cell dimensions. This is suitable for measurements of cardiomagnetic activity which resemble the strongest fields of medical interest, around one million times weaker than geomagnetic fields [26]. MCG maps allow non-invasive and contact-free detection of abnormalities in the myocardium for early detection of arrhythmias and other cardiovascular diseases, which are currently the most common cause of death in developed countries [26]. Analysing brain signals requires the highest precision sensors currently available and is utilised to diagnose conditions such as epilepsy or, alternatively, to study neural responses from auditory and visual stimuli [27]. In the past, SQUIDs have been predominantly utilised in MEG measurements as they demonstrate sensitivities of around $5 \text{ fT}/\sqrt{\text{Hz}}$ in the frequency band applicable to biomagnetic study, typically limited by the electrically-conductive radiation-shielding of the liquid-helium dewars used for cryogenic cooling [28]. The application of OPMs in biomedical science is especially encouraging as they can operate above room temperature unlike their cryogenic predecessors allowing one to place the sensor closer to the source, resulting in potential SNR enhancements. SERF mag-

netometers have recently been employed to record brain stimuli [29], and have also produced human [3] and fetal [30] MCGs to a remarkable standard.

The bandwidth of an atomic magnetometer determines how quickly the device can respond to rapidly fluctuating fields, and dictates its ability to reliably track a time-varying magnetic signal. There are a number of factors that can affect the bandwidth depending on the particular experimental arrangement, data acquisition, and signal processing techniques employed. Fundamentally, the bandwidth will be limited by atomic depolarisation such that the sensor's frequency response follows a low-pass filter behaviour with a rolloff frequency proportional to the spin decoherence rate [27]. Hence, there is a distinct tradeoff between the magnetometer sensitivity and bandwidth that provides a degree of tunability in the sensor. The measurement bandwidth is often governed by the magnetometer's sampling rate as time must be spent acquiring a signal and extracting the precession frequency. Thus, any fluctuations in the field during this period will be averaged in a way that is dependent on the nature of the data and how it is processed. The bandwidth is usually tailored for the field fluctuation of interest so that the sensitivity is optimal; for example, high-sensitivity SERF magnetometers employed in medical applications will have reduced bandwidths of around 100 Hz [29].

Many atomic magnetometry schemes operate in the continuous-wave regime where the spin preparation (pump) and detection (probe) stages are performed simultaneously with a single laser beam. Of particular recent interest are scalar pulsed magnetometers [31–33] in which the magnetic field is estimated directly from the frequency of the recorded FID experienced by the spin-polarised atoms. This modality does not rely on additional hardware such as a concurrent drive, phase detection, or feedback loops to obtain the absolute strength of the magnetic field. As a result FID OPMs not only offer a simple device design but also exhibit superior accuracy compared with the commonly used driven architectures, which are prone to systematic errors due to their auxiliary instrumentation. Commercial atomic magnetometers will have a specified tolerance that accounts for any systematic shifts that may affect the measurement accuracy. For most OPMs, the AC Stark effect causes a characteristic shift in the Larmor frequency as a consequence of the light-atom interaction during readout. Also, many scalar sen-

sors operating in Earth’s field conditions will be subject to heading errors that induce an orientational dependence on the sensor output. Systematics can also drift over time due to technical noise sources thus mitigating these effects is extremely important in applications requiring measurements over long time intervals, such as geological surveys. OPMs that utilise lock-in detection typically require an initial estimation of the field before sweeping across the magnetic resonance. This can be quite difficult in an unshielded environment where the ambient fields are unpredictable and prone to fluctuations. The FID mechanism is desirable as it can be implemented in a single-pulse regime in which the magnetic field information is readily extracted from the observed transient oscillation without any prior knowledge of the field. This obviates the need for demodulation and tracking of the modulation frequency. An alternative approach is to utilise synchronous optical pumping whereby the light field is modulated at the Larmor frequency, as adopted by Bell and Bloom [34]. A sensitivity of $1 \text{ pT}/\sqrt{\text{Hz}}$ has been shown with an all-optical Bell-Bloom magnetometer using independent pump and probe beams in a sensing volume of 16 mm^3 [25]. These OPMs are inherently scalar sensors, contrary to fluxgate magnetometers, and do not provide information regarding the field orientation. Vector atomic magnetometers do exist although typically require triaxial coil assemblies to extract the vector components [1]. Alternatively, one can increase the complexity of the system by applying multiple laser beams in a magnetically silent configuration [35]. Unfortunately, sacrifices have to be made to gain directional information in comparison to scalar measurements thus these OPMs are better served for applications in which this is not a critical factor.

One of the primary contributions of this work was to investigate the optimal performance of Texas Instrument’s microfabricated Cs vapour cells as magnetic field sensors, to aid in prototyping a chip-scale atomic magnetometer (CSAM). The envisioned CSAM can be represented by the simple design shown in Fig. 1.1 that comprises a selection of components that are mass manufacturable. For example, a solitary VCSEL could be mounted at the base of the structure, above which a quarter-wave plate is stacked to alter the light polarisation for optimisation of the optical pumping and detection processes. This is followed by a MEMS Cs cell containing heater tracks to

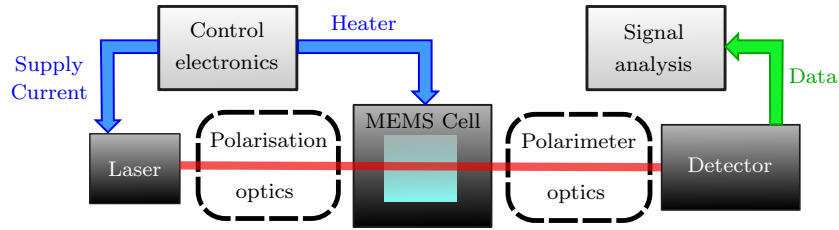


Figure 1.1: Schematic illustrating a potential design for a portable atomic sensor. The MEMS cell containing alkali vapour is millimetre scale, accompanied by a laser source (e.g. VCSEL) and miniaturised optics for conditioning of the beam. More complex polarimetry optics can be used to enhance detection sensitivity.

control the cell temperature and generate sufficient atomic density. Detection will require a minimum of one photodiode to observe transmission of the light propagating through the cell. Alternatively, the sensor precision could be improved by monitoring optical rotation in the light polarisation using a polarising element such as a linear polariser. The sensitivity can be enhanced further by adding a polarising beam splitter (PBS) and second photodiode to enable differential detection which rejects common-mode noise; however, this does increase the fabrication cost and complexity. Based on the results gained throughout this thesis, it is fair to surmise that a cm-scale packaged device with sensitivities approaching the single pT-level is possible. Also, with Texas Instrument’s expertise in automation the fabrication process can be made extremely efficient with pick-and-place machines allowing a sensitive and reproducible sensor that can be manufactured in high volumes at a reduced cost.

This thesis has been structured into four main segments. Chapter 2 introduces some of the theoretical principles underlying the functionality of atomic magnetometers based on MEMS cells. This includes an analysis of the spectroscopic properties associated with the microfabricated Cs vapour cells utilised in this work, aiding in assessing the sensor heads compatibility for magnetometry. We also describe some of the critical processes relating to system operation including optical pumping, Larmor precession, and spin relaxation. Chapter 3 provides details on the OPM employed throughout this thesis which is based on the FID mechanism, with particular emphasis placed on signal processing and sensitivity optimisation. A review of the principal results from

Chapter 1. Introduction

this chapter can be found in [24], by Hunter *et. al.* Chapter 4 focusses primarily on characterising the sensor’s bandwidth and demonstrates the techniques capabilities in reconstructing time-vary magnetic signals on top of a strong bias field, similar to that of the Earth’s. This work was the product of a 4-month internship at Texas Instruments who were the industrial partner in a collaboration with the University of Strathclyde; the majority of the experimental findings are detailed in [31], by Hunter *et. al.* Finally, Chapter 5 proposes a novel technique utilising Ramsey-like detection to accurately measure spin precession without being subject to systematics instigated by the light-atom interaction. This detection mode is also utilised to measure ground state coherence in a selection of vapour cells containing different quantities of buffer gas. A manuscript presenting an overview of this detection technique is in preparation.

Publications Arising from This Work

- D. Hunter, S. Piccolomo, J. Pritchard, N. Brockie, T. Dyer, and E. Riis, “Free-induction-decay magnetometer based on a microfabricated Cs vapor cell,” *Physical Review Applied*, vol. 10, p. 014002, 2018.
- D. Hunter, R. Jiménez-Martínez, J. Herbsommer, S. Ramaswamy, W. Li, and E. Riis, “Waveform reconstruction with a Cs based free-induction-decay magnetometer,” *Optics Express*, vol. 26, no. 23, pp. 30 523-30 531, 2018.

Chapter 2

General Magnetometry Theory

Numerous atomic magnetometer configurations exist for the detection and measurement of magnetic field signals, all sharing the same fundamental principles in their operation; specifically the preparation, evolution and detection of atomic spins. We begin by providing an overview of the optical resonance structure that one would expect from an alkali-metal such as Cs, followed by a description on how light-atom interactions can be used to manipulate the atomic spins through processes such as optical pumping. The atomic response to external magnetic fields is considered in conjunction with the possible spin depolarising mechanisms that can limit the coherence lifetime. Finally, we detail the effects that a nitrogen (N_2) buffer gas has on the optical spectrum, and how the observed behaviour can be used to infer the spin relaxation dynamics inherent to the vapour cell. This analysis is performed with regards to the MEMS cells designed and fabricated at Texas Instruments that were utilised as the primary sensing element throughout the entirety of this work.

2.1 Light-Atom Interactions

2.1.1 Energy structure of an alkali-metal atom

In order to understand the fundamental principles of atomic magnetometers it is first useful to consider the energy level structure of an alkali-metal atom. They are located

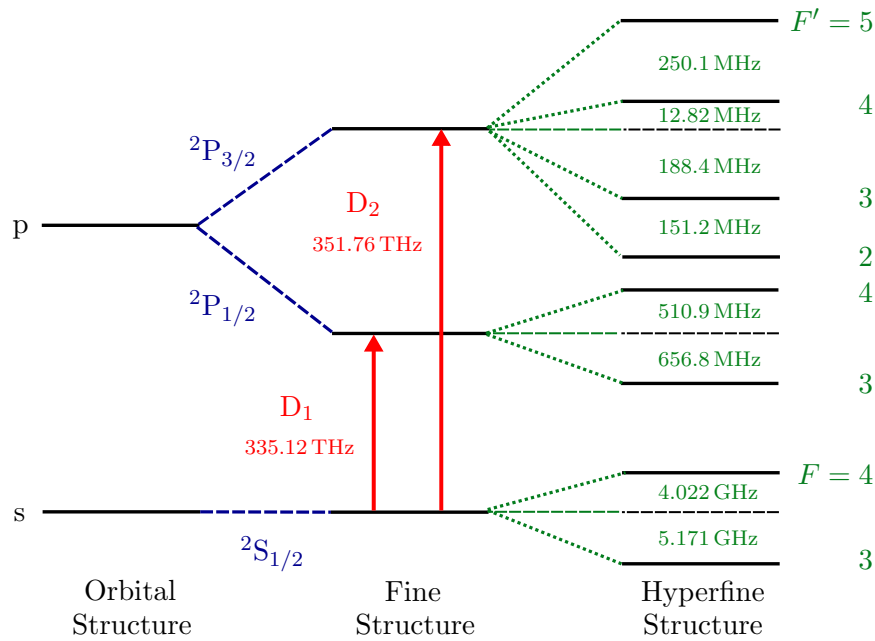


Figure 2.1: Energy structure diagram illustrating the ground and first excited states of a Cs atom. The D_1 and D_2 transitions arise due to the fine structure interaction. Coupling of the electron angular momentum with the nuclear spin results in hyperfine structure; this is denoted by the quantum number F with the additional prime symbolising an excited state. Splittings are not to scale.

in group 1A of the periodic table with a single optically active electron occupying the outermost, s, subshell in the ground state, equivalent to an orbital angular momentum $L = 0$ [36]. Electrons have half-integer spin $S = 1/2$ with the projections $m_s = +1/2$ and $m_s = -1/2$ eluding to the quantum states oriented parallel or antiparallel to an externally applied field, respectively. Addition of the orbital and spin components results in a total angular momentum $\vec{J} = \vec{L} + \vec{S}$ with the corresponding quantum number $J = |\vec{J}|$ restricted to integer values inside the range $|L - S| \leq J \leq L + S$. The standard spectroscopic notation used to specify an occupied quantum state is typically given in the form¹ $|L, S, J\rangle = (2S+1) L_J$; for example the ground state is written as $2S_{1/2}$ [36].

The spin-orbit coupling between the magnetic field generated by an orbiting electron and its intrinsic magnetic moment induces splitting of the optical spectra, known as fine structure [37]. This lifts the degeneracy of excited state multiplets with the p or-

¹The superscript $2S + 1$ is known as the spin multiplicity.

orbital separating into the sublevels ${}^2P_{1/2}$ and ${}^2P_{3/2}$, giving rise to the D₁ (${}^2S_{1/2} \rightarrow {}^2P_{1/2}$) and D₂ (${}^2S_{1/2} \rightarrow {}^2P_{3/2}$) transitions, respectively; these are extensively utilised in the optical pumping and detection processes of atomic magnetometers [38]. The interaction between the nuclear spin \vec{I} , with quantum number $I = |\vec{I}|$, and the electrons angular momentum \vec{J} leads to a more closely spaced splitting of the atomic spectra in the form of hyperfine structure with the total angular momentum $F = |\vec{F}|$ limited to integer steps within the range $|I - J| \leq F \leq I + J$. Figure 2.1 depicts the energy structure of Cs, the atomic species of choice in this work, showing the D₁ and D₂ transitions with their corresponding hyperfine structure [39]. The D₁ line is the most commonly utilised transition for magnetometry as it demonstrates superior optical pumping efficiency [1]; however, the D₂ line is occasionally used for optical detection purposes in geometries that implement separate pump and probe beams [38].

2.1.2 Absorption cross-section

Light propagating through an alkali vapour cell will experience attenuation as a consequence of the interaction with the atomic gas. This is quantified using the absorption coefficient and can be measured by monitoring the light transmitted through the medium and applying the Beer-Lambert law [40],

$$\mathcal{T} = \frac{I(z = L)}{I(z = 0)} = e^{-\alpha(\nu, T)L}, \quad (2.1)$$

where \mathcal{T} is the transmission describing the fraction of light exiting the cell, $I(z)$ is the light intensity as a function of propagation distance through the sample, $\alpha(\nu, T)$ is the absorption coefficient, and L is the total path length equivalent to the thickness of the vapour cell. As seen in Fig. 2.1, alkali vapours have multiple excitable resonances; therefore, we can rewrite the absorption coefficient as a sum of independent contributions,

$$\alpha = \sum_{F, F'} \alpha_{FF'}, \quad (2.2)$$

where $\alpha_{FF'}$ is the absorption coefficient associated with the transition $F \rightarrow F'$. The frequency dependence of the total absorption coefficient, α , becomes clear as the light will interact simultaneously with each independent transition with a weighting dependent on the frequency detuning of the laser and the strength of the interaction. The absorption coefficient is a macroscopic quantity that can be described microscopically in the form of the absorption cross-section,

$$\sigma = \frac{1}{\mathcal{N}} \sum_{F, F'} \alpha_{FF'} = \sum_{F, F'} \sigma_{FF'}, \quad (2.3)$$

where \mathcal{N} is the number density of the atomic medium. This introduces a distinct temperature dependence as seen in Appendix A.1.

The electric susceptibility, $\chi(\nu)$, is a complex quantity that describes both the absorptive and dispersive properties of the medium. For a single hyperfine transition it can be expressed in the following form [40],

$$\chi_{FF'}(\nu) = \mathcal{N} \frac{C_{FF'}^2 d^2}{2(2I+1) \hbar \epsilon_0} f_{FF'}(\Delta_{FF'}), \quad (2.4)$$

where $f_{FF'}(\nu)$ is the normalised resonance lineshape for the $F \rightarrow F'$ transition, $\Delta_{FF'} = \nu - \nu_{FF'}$ is the laser detuning from resonance, and $C_{FF'}^2 d^2$ is the transition strength with the reduced dipole matrix element $d = \langle L | \hat{d} | L' \rangle$ [39]. The absorption cross-section can be determined from the imaginary part of the electric susceptibility,

$$\sigma_{FF'}(\nu) = \frac{k}{\mathcal{N}} \text{Im}[\chi_{FF'}(\nu)], \quad (2.5)$$

where $k = 2\pi/\lambda$ is the wave number of the probe beam and λ is the wavelength. Using Eq. (B.1.5) in Appendix B.1, the reduced dipole matrix element can be related to the transition decay rate Γ_0 which is a known quantity [41]. For the Cs D₁ transition,

$$\Gamma_0 = \frac{k^3 d^2}{9\pi \epsilon_0 \hbar}. \quad (2.6)$$

Substituting Eq. (2.4) into Eq. (2.5), the absorption cross-section for the $F \rightarrow F'$ transition can be defined as,

$$\sigma_{FF'}(\nu) = \frac{C_{FF'}^2 d^2 k}{2(2I+1) \hbar \epsilon_0} f_{FF'}(\Delta_{FF'}). \quad (2.7)$$

Using the definition of the transition lifetime in Eq. (2.6) and summing over all hyperfine components, we arrive at the final expression for the total absorption cross-section given by,

$$\sigma(\nu) = \frac{9\lambda_0^2 \Gamma_0}{4\pi 2(2I+1)} \sum_{F, F'} C_{FF'}^2 f_{FF'}(\Delta_{FF'}), \quad (2.8)$$

where $I = 7/2$ is the nuclear spin of Cs, and $\lambda_0 = 894.59$ nm [42] and $\Gamma_0 = 4.56$ MHz [43] are the wavelength and natural linewidth of the Cs D₁ line, respectively. Assuming a monochromatic light source, the rate at which photons are absorbed by an atom can be described by the expression [44],

$$R_{abs} = \sigma(\nu)\Phi. \quad (2.9)$$

The photon flux Φ , in units of $\text{cm}^{-2}\text{s}^{-1}$, is given by [45],

$$\Phi = \frac{cI_0}{4\pi h\nu}, \quad (2.10)$$

where I_0 is the intensity of the incident light. The absorption of resonant or near-resonant light is crucial in atomic magnetometers as it affects processes such as optical pumping and detection that dictate the quality of an acquired signal.

2.1.3 Optical resonance lineshape

In the absence of additional broadening effects, the resonance linewidth is governed by the natural lifetime of the atomic transition $\tau = 1/(2\pi \Gamma_0)$ [1]. This natural broadening

mechanism is homogenous resulting in a Lorentzian profile,

$$\mathcal{L}(\Delta_{FF'}) = \frac{1}{\pi} \frac{(\Gamma_l/2)}{\Delta_{FF'}^2 + (\Gamma_l/2)^2}, \quad (2.11)$$

where Γ_l is the full width at half maximum (FWHM) Lorentzian linewidth. Equation (2.11) can be derived using the steady-state solution of the optical Bloch equations for a two-level atom [46].

The probability of an atom moving at a specific velocity in a sample is described by the temperature dependent Maxwell-Boltzmann distribution. Each atom will thus experience a different laser frequency as a consequence of the Doppler effect resulting in a inhomogenously broadened system that displays a Gaussian lineshape,

$$\mathcal{G}(\Delta_{FF'}) = \frac{2\sqrt{\ln 2/\pi}}{\Gamma_g} \exp\left(-4 \ln 2 \frac{\Delta_{FF'}^2}{\Gamma_g^2}\right), \quad (2.12)$$

where Γ_g is the FWHM Doppler broadened linewidth. With both natural and Doppler broadening occurring simultaneously, the atomic frequency response will be fully described by the Voigt profile which is given by the convolution of the Gaussian and Lorentzian lineshapes,

$$\mathcal{V}(\nu - \nu_{FF'}) = \int_{-\infty}^{\infty} \mathcal{G}(\nu' - \nu_{FF'}) \mathcal{L}(\nu - \nu') d\nu'. \quad (2.13)$$

Analytically, the Voigt profile is described by the expression [1],

$$\mathcal{V}(\Delta_{FF'}) = \frac{2\sqrt{\ln 2/\pi}}{\Gamma_g} w\left(\frac{2\sqrt{\ln 2/\pi}(\Delta_{FF'} - i\Gamma_l/2)}{\Gamma_g}\right), \quad (2.14)$$

where $w(x)$ contains the complex complementary error function as seen below,

$$w(x) = e^{-x^2} \operatorname{erfc}(-ix). \quad (2.15)$$

Fitting the nonlinear model provided in Eq. (2.14) is computationally challenging and time consuming. The process can be simplified significantly by utilising a numerical approximation, composed of a weighted sum of the Gaussian and Lorentzian functions as

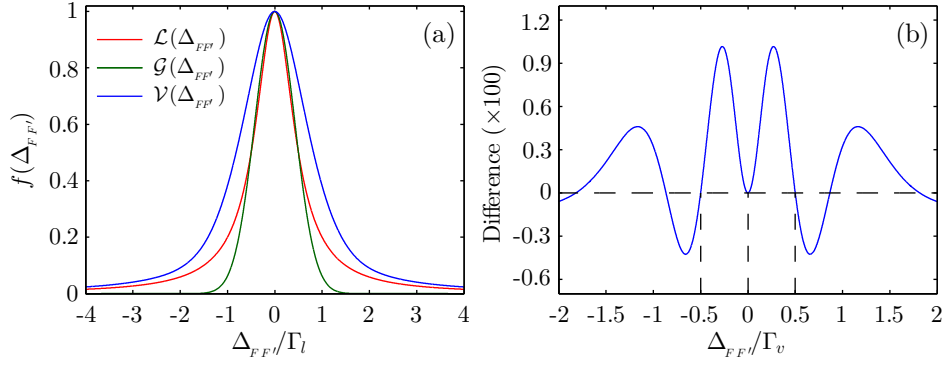


Figure 2.2: (a) Depiction of the normalised Lorentzian, Gaussian and Voigt profiles with $\Gamma_l = \Gamma_g$. The Voigt linewidth can be estimated as $\Gamma_v \simeq 1.64 \Gamma_l$ in this case. (b) Difference ($\times 100$) between the analytical and numerically approximated normalised Voigt profiles. The dashed lines have been positioned at $\Delta_{FF'} = 0$, $\Delta_{FF'} = \Gamma_v/2$ and $\Delta_{FF'} = -\Gamma_v/2$ where the error approaches a minimum close to zero.

discussed in Appendix B.2 [47]. Figure 2.2(a) shows a plot of the normalised Lorentzian and Gaussian functions, with the corresponding Voigt profile in the case that $\Gamma_l = \Gamma_g$. Under these conditions, the Voigt linewidth can be estimated as $\Gamma_v \simeq 1.64 \Gamma_l$ using the Olivero-Longbothum formula given in Eq. (B.2.4) [48]. Figure 2.2(b) shows the difference between the normalised Voigt profiles calculated using both the analytical expression provided in Eq. (2.14) and its numerical approximation. It can be seen that in this case the error approaches zero at the function maximum and half widths; these are crucial parameters that are prevalent in the analysis of experimental spectra. In fact, the maximum error in the amplitude and width will not exceed 0.55 % and 0.01 %, respectively [47].

Doppler broadening will dominate the linewidth of the transition in cases that the vapour cell is operated at or above room temperature (e.g. $\Gamma_g \simeq 392$ MHz at 85°C). Therefore, it is fair to assume a Gaussian lineshape in the absence of any collisional broadening effects. However, additional line broadening can be introduced through substances such as buffer gases which are commonplace in microfabricated vapour cells [24]. Similar to natural broadening, collisions with buffer gas atoms is considered as a homogeneous process as each atom is affected in the same way, leading to a Lorentzian profile. Thus, the convolved optical spectrum often displays a more pronounced Voigt

lineshape, and in certain instances a Lorentzian profile can be assumed if collisional broadening is the dominant mechanism.

2.1.4 Optical pumping

Polarising an atomic spin ensemble is critical in attaining high sensitivities, and this is predominantly achieved through a process known as optical pumping. To emphasise the importance of this mechanism we consider alkali atoms that are an initially unpolarised with the magnetic sublevels populated according to the Boltzmann distribution at thermal equilibrium. The thermally induced spin polarisation is given by [49],

$$P = \tanh\left(\frac{g_s \mu_B |\vec{B}|}{2k_B T}\right), \quad (2.16)$$

where g_s is the electron g-factor and μ_B is the Bohr magneton. Here we have considered only the electron spin and have ignored the nuclear components, resulting in a spin-1/2 system as illustrated in Fig. 2.3. It is possible to generate significant polarisations using cold atoms [50]; however, this would be difficult to commercialise and enforces restrictions on sensor scalability hence the extended use of thermal vapour cells. The polarisation achievable at operational temperatures for these cells through thermal effects alone is too small for magnetometry measurements. For example, a polarisation of only 10^{-7} is achieved at room temperature in the presence of the Earth's magnetic field ($\sim 50 \mu\text{T}$); therefore, the Zeeman sublevel population is essentially equally distributed.

The process of optical pumping is illustrated in Fig. 2.3 for a simple spin-1/2 system that is irradiated with σ^+ light consisting of photons with angular momentum $+\hbar$. These photons excite and transfer their angular momentum to the atoms occupying the $m_s = -1/2$ state. Once excited, the atoms will then spontaneously decay with the branching ratio of the decay channels governed by the Clebsch-Gordan coefficients² [1]. Atoms in the $m_s = +1/2$ ground state are transparent to the pumping light as there is no excited state available in which angular momentum is conserved. Thus, complete orientation of the atomic sample in the direction of light propagation would be achieved

²The addition of a quenching gas mixes the excited state population and equalises the branching ratios.

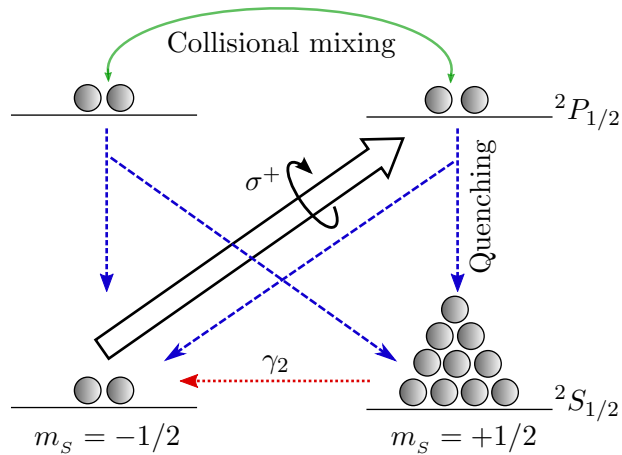


Figure 2.3: Electron spin of an alkali atom is optically pumped with resonant circularly polarised light. Atoms in the $m_s = -1/2$ sublevel are excited into the $^2P_{1/2}$ state after absorbing a photon. Collisions with buffer gas atoms mix the excited state population thus equalising the probability of spontaneously decaying into either ground state sublevel via radiation quenching. Atoms in the $m_s = +1/2$ state are transparent to σ^+ light and remain in this state unless undergoing spin relaxation that occurs at the rate γ_2 . The induced population imbalance in the ground state manifold is equivalent to polarisation being generated in the atomic sample by means of optical pumping.

in the absence of other relaxation mechanisms. Conversely, if σ^- light is used then the atomic medium would become fully spin polarised antiparallel to the beam axis. There are several mechanisms that can depolarise atoms and restrict the optical pumping efficiency. The predominant influence is transverse spin relaxation that occurs at the rate γ_2 and is an accumulation of numerous contributions that are discussed later in Section 2.4.1. Another depolarising mechanism, known as radiation trapping, arises as a consequence of absorbing unpolarised photons that are spontaneously emitted by an excited atom [51]. This becomes particularly cumbersome when operating at high atomic densities; however, substances such as nitrogen circumvent this issue by acting as a quenching gas. These types of gases are very useful as they do not chemically react with the atomic vapour and have vibrational excitations near-resonant with the alkali resonance lines, inhibiting the spontaneous decay of unpolarised photons [52].

The dynamics of optical pumping can be formulated for the simple spin-1/2 system described in Fig. 2.3 by means of the rate equations. The evolution of the occupational probabilities ρ_- and ρ_+ associated with the $m_s = -1/2$ and $m_s = +1/2$ ground states

respectively, are described by the following expressions [1],

$$\dot{\rho}_- = -a(1+s)R_p\rho_- + a(1-s)R_p\rho_+, \quad (2.17)$$

$$\dot{\rho}_+ = -a(1-s)R_p\rho_+ + a(1+s)R_p\rho_-, \quad (2.18)$$

where the optical pumping efficiency parameter, residing in the range $1/3 \leq a \leq 1/2$, is related to the probability of the decay channels and is maximal in the case of complete collisional mixing. The optical pumping rate R_p is defined as the average rate of absorption for an unpolarised atom as defined in Eq. (2.9). The model also extends to arbitrary light polarisations $\hat{\boldsymbol{\epsilon}}$ where the average photon spin \mathbf{s} is given by,

$$\mathbf{s} = i\hat{\boldsymbol{\epsilon}} \times \hat{\boldsymbol{\epsilon}}^*, \quad (2.19)$$

where $s = \mathbf{s} \cdot \hat{\mathbf{z}}$ is the component of the spin along the propagation direction with $s = -1$, $s = 1$, and $s = 0$ representing σ^- , σ^+ and linearly π polarised light respectively, and intermediate values indicating elliptical polarisation. If we assume a closed transition then the total number of atoms is constant, i.e. $\rho_+ + \rho_- = 1$, as the lifetime of the excited state is considerably shorter than that of the ground state. The average spin polarisation along the direction of beam propagation is defined as,

$$\langle S_z \rangle = \frac{1}{2}(\rho_+ - \rho_-). \quad (2.20)$$

Substituting Eq. (2.20) into Eqs. (2.17) and (2.18) then the rate of change of $\langle S_z \rangle$ can be calculated as,

$$\langle \dot{S}_z \rangle = aR_p(s - 2\langle S_z \rangle) - \gamma_2\langle S_z \rangle, \quad (2.21)$$

where we have accounted for transverse relaxation at the rate γ_2 occurring as a consequence of several collisional and externally induced decoherence mechanisms. Equation

(2.21) has the solution,

$$\langle S_z \rangle = s \frac{aR_p}{2aR_p + \gamma_2} \left(1 - e^{-(2aR_p + \gamma_2)t} \right). \quad (2.22)$$

The electron spin polarisation along the beam axis is defined as $P_z = \langle S_z \rangle / S$ where $S = 1/2$ is the electron spin. This will tend toward the equilibrium value,

$$P_z = s \frac{2aR_p}{2aR_p + \gamma_2}. \quad (2.23)$$

Equation (2.23) allows an estimation of the total spin polarisation that is generated as a consequence of optical pumping at the rate R_p whilst competing against the effects of spin relaxation. The vapour cells utilised in this work contain N_2 that acts as a buffer and quenching gas, thus we assume that $a = 1/2$ as collisional mixing will equalise the branching ratios of the decay channels [1]. A more extensive model would account for all 32 Zeeman sublevels of the D_1 line that would be described by the evolution of a 32×32 density matrix [53]. Neglecting the excited state levels would be a valid approximation as the atoms spend most of their time in the ground state manifolds; however, the model is still computationally intensive to solve even with this simplification.

2.2 Microfabricated Vapour Cell Technology

2.2.1 Vapour cell fabrication

The vapour cells used throughout this work were designed and manufactured at Texas Instruments. The silicon wafer structures containing the necessary caesium compound are delivered to the University of Strathclyde for spectroscopic analysis, and for use in the benchtop magnetometry system. The fabrication process involves etching a 1.5 mm thick silicon wafer, compatible with large-scale production, to form the cell cavities. The holes are created using a wet etch process producing a cavity with a trapezoidal cross-section; the sides are etched in the $\{111\}$ crystal direction whereas the bottom resides in the $\{100\}$ plane resulting in an angle of 35.3° with respect to the vertical direction. Glass is bonded to one side and the cells are filled with a caesium

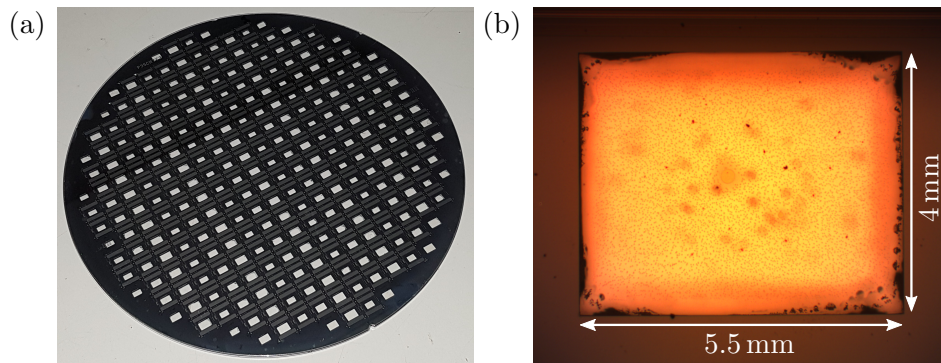


Figure 2.4: (a) An example of a 1.5 mm thick silicon wafer, 8'' in diameter, containing numerous undiced cells. (b) Cavity of a typical vapour cell; condensed Cs vapour is clearly visible with azide residual mostly accumulating around the sides of the vapour cell.

azide (CsN_3) water-based solution [54]. After evaporation, a second stage of anodic bonding seals the top face of the wafer with an upper glass surface. An example of the final result is shown in Fig. 2.4(a). It can be seen that various cavity geometries can be implemented depending on the mask used during the photolithography stage of the fabrication process. Silicon manufacturing processes have been well established within the semiconductor industry; however, silicon is typically restricted by the wet etch process. On the other hand, materials such as processed glass may provide a cheaper alternative that is easier to manipulate into different geometries with drilling techniques. The difficulty arises in sealing the glass wafer; silicon can be used for this purpose although Fresnel reflection becomes more prominent due to its higher refractive index. The manufacturing process at Texas Instruments has been refined over several years which has led to an impressive yield, throughput and the ability to achieve narrow spectroscopic specifications required by clients. This, along with the low fabrication costs, improves the commercial viability of these vapour cells especially with the rising interest in atomic sensing technologies such as OPMs, atomic clocks, and gyroscopes.

Following a method suggested in the literature [54–56], the entire wafer is exposed to UV light in order to dissociate the azide into its constituents; nitrogen as a buffer gas and Cs in the metallic form. As the UV process progresses, the Cs vapour starts to saturate the cell and we observe droplets of metallic Cs condensing on the glass

walls of the cells. Figure 2.4(b) shows the presence of Cs droplets on the upper glass surface of a single cell. Crystallized azide residual is visible close to the borders of the lower glass surface. Localising azide residual to the sides is crucial in preventing light from being blocked as it traverses the cell, and aids in enhancing the SNR in both spectroscopy and magnetometry measurements. Fresnel reflection occurs when light strikes the glass windows at both sides of the cell resulting in around 8% loss in light at normal incidence. Thus, positioning the cell at a slight angle can help to improve transmission through the vapour cell and, in turn, the SNR especially if the optical power available is limited as is typically the case with VCSELs.

2.2.2 Buffer gas effects

In the presence of N₂ buffer gas the optical resonance is modified by two phenomena proportional to the pressure [57]. Firstly, homogeneous broadening due to collisions with the buffer gas molecules increases the Lorentzian linewidth,

$$\Gamma_l = \Gamma_0 + \Gamma_{N_2}, \quad (2.24)$$

where Γ_{N_2} is the total linewidth broadening. Additionally, a characteristic shift of the transition frequencies occurs which is denoted by the modified detuning,

$$\Delta'_{FF'} = \Delta_{FF'} + \Delta_{N_2}, \quad (2.25)$$

where Δ_{N_2} is a collisional induced shift. Figure 2.5 illustrates both these phenomena through various simulated absorption spectra that represent the anticipated effects of different buffer gas pressures. It can be seen that the transitions are red shifted; however, the sign and extent of this shift is dependent on the type of buffer gas molecule [57]. Also, the slightly temperature dependent ratio between these two parameters can be viewed as a characteristic of the particular buffer gas. For N₂ it is $\Gamma_{N_2}/\Delta_{N_2} \approx -2.24$ at 85 °C, which is the set temperature for the spectroscopic analyses performed in this work.

Numerous shift rates δ_{N_2} and broadening rates γ_{N_2} exist in the literature which are

γ_{N_2} (MHz/Torr)	δ_{N_2} (MHz/Torr)	$\gamma_{N_2}/\delta_{N_2}$	T_r (K)	Ref.
15.82 ± 0.05	-7.69 ± 0.01	-2.06 ± 0.007	318	[57]
16.36 ± 0.02	-7.71 ± 0.01	-2.12 ± 0.004	323	[57]
15.66 ± 0.08	-7.41 ± 0.01	-2.11 ± 0.011	333	[57]
19.51 ± 0.05	-8.23 ± 0.02	-2.37 ± 0.008	294	[58]
30.82 ± 5.71	-7.38 ± 0.11	-4.18 ± 0.776	295	[59]
14.73 ± 0.69	-8.9 ± 0.69	-1.66 ± 0.15	393	[60]

Table 2.1: List of broadening rates γ_{N_2} and shift rates δ_{N_2} measured at the reference temperature T_r . These conversions are utilised to infer the N_2 buffer gas pressure from the observed broadening and shift in the optical spectrum.

utilised as conversions for our estimation of the N_2 pressure inside the vapour cell, based on characteristics of the absorption spectrum; some examples are listed in Table 2.1 along with the corresponding reference sources. These rates are temperature dependent and follow the power laws [61],

$$\gamma_{N_2}(T) = \gamma_{N_2}(T_r) \left(\frac{T_r}{T} \right)^{\frac{1}{2}}, \quad (2.26)$$

$$\delta_{N_2}(T) = \delta_{N_2}(T_r) \left(\frac{T_r}{T} \right)^{0.82}, \quad (2.27)$$

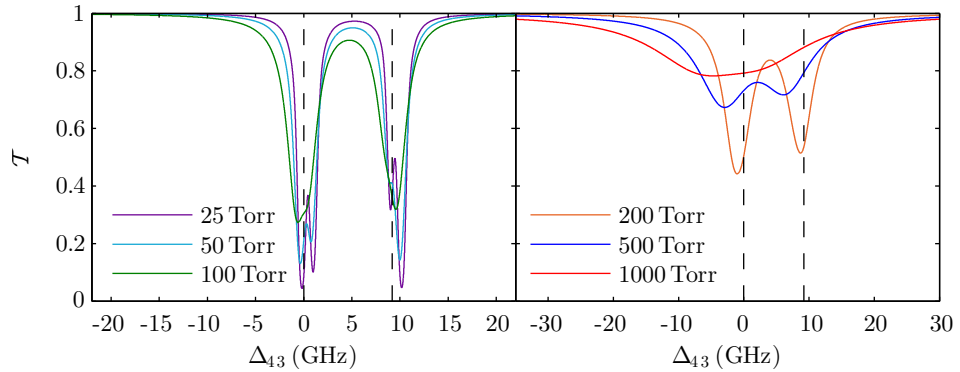


Figure 2.5: Impact of N_2 buffer gas on the optical spectrum at varying pressures. Broadening in the linewidths range from $\Gamma_{N_2} = 0.4 - 16.6$ GHz and the pressure induced shifts extend from $\Delta_{N_2} = -0.2$ GHz to $\Delta_{N_2} = -7.2$ GHz. At the pressure $P_{N_2} = 1000$ Torr, the hyperfine peaks have been merged into a single resonance. A cell of thickness 1.5 mm and an operating temperature of 85°C were assumed. The dashed lines in each plot symbolise the $F = 4 \rightarrow F' = 3$ ($\Delta_{43} = 0$) and $F = 3 \rightarrow F' = 3$ ($\Delta_{43} = 9.193$ GHz) transitions of the Cs D_1 line from left to right, respectively.

where T_r and T are the reference and set temperatures, respectively. The exponents in each relation have been determined empirically and are specific to Cs-N₂ interactions. Using Eqs. (2.26) and (2.27) and performing a weighted average of the experimental results listed in Table 2.1, the conversion rates at $T = 85^\circ\text{C}$ were calculated to be $\gamma_{N_2} = 15.72 \pm 0.02 \text{ MHz/Torr}$ and $\delta_{N_2} = -7.01 \pm 0.01 \text{ MHz/Torr}$.

2.2.3 Spectroscopic testing

We use absorption spectroscopy to deduce the amount of N₂ content within the microfabricated Cs vapour cells to obtain precise information on the azide dissociation process. The spectroscopic properties are determined by directing a low intensity linearly polarised light beam through the vapour cell as illustrated in Fig. 2.6(b). The laser intensity is kept below the resonant saturation intensity $I_{sat} \simeq 25 \mu\text{W}/\text{mm}^2$ to avoid power broadening. A reference setup was used to normalise the intensity variation of the laser and also provided a relative and absolute frequency reference using an etalon and auxiliary Cs cell. Figure 2.6(a) shows an example of an absorption signal recorded from the sensor head; it can be seen that collisional broadening has merged the

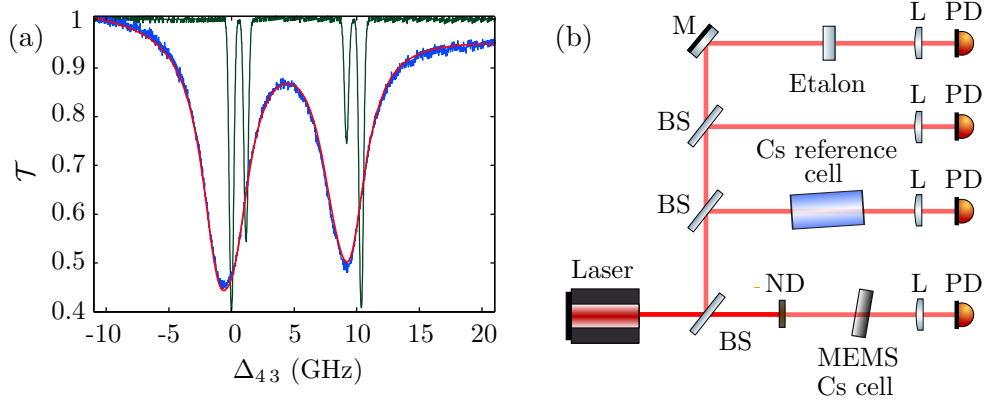


Figure 2.6: (a) Spectroscopic signal (blue) and corresponding fit to a Voigt profile (red) for the vapour cell displayed in Fig. 2.4(b). The frequency axis is scaled relative to the $F = 4 \rightarrow F' = 3$ transition; the leftmost resonance in the reference signal (green). The N₂ pressure is determined from the shift and broadening exhibited with respect to the reference spectrum. (b) Experimental set-up for the spectroscopic analysis of the microfabricated vapour cells. The laser frequency is swept through the Cs D₁ transition. (BS, beam splitter; ND, neutral density filter; L, lens; M, mirror; PD, photodiode; MEMS, microelectromechanical system.)

transitions resulting in a spectrum consisting of two resolvable and slightly overlapping resonances. The Levenberg-Marquardt (LM) fit algorithm [62] was applied to the data to extract the relevant free-parameters, primarily the broadening and shift, using the Beer-Lambert law and the absorption cross-section derived in Eq. (2.8). The linewidth broadening and shift, for the spectrum exhibited in Fig. 2.6(a), were calculated to be $\Gamma_{N_2} = 2.76$ GHz and $\Delta_{N_2} = 0.99$ GHz, respectively. The ratio of these two parameters is slightly higher than the predicted value, most likely as a consequence of imperfections introduced during the fabrication process. A buffer gas pressure of $P_{N_2} = 176$ Torr was obtained using the fitted broadening parameter, whereas a pressure of $P_{N_2} = 141$ Torr was calculated from the shift. Therefore, it is reasonable to base our final estimation of the buffer gas pressure inside the vapour cell on the weighted average of both these results which was calculated to be $P_{N_2} = 158$ Torr for this vapour cell.

Ultimately, the sensitivity of an atomic magnetometer is limited by the dimensions of the alkali vapour cell. The fabrication process can be altered to adjust the N_2 pressure based on the size of the cavity; for example, the amount of Cs azide content can be varied as well as the UV light dose to release more N_2 molecules during the dissociation process and raise the buffer gas pressure. One can also perform anodic bonding of the glass to the silicon wafer in a nitrogen atmosphere allowing linewidths exceeding $\Gamma_{N_2} > 20$ GHz, corresponding to above atmospheric pressure. The etching process can also be modified to produce different cavity volumes; however, the wall relaxation rate is mostly dependent on the smallest cavity dimension which in this case is the thickness of the vapour cell that is kept consistent at 1.5 mm.

2.3 Atomic Interactions with Static Magnetic Fields

2.3.1 Larmor precession

To demonstrate the concept of Larmor precession, we again consider a simplified spin-1/2 system that interacts with an externally applied field \vec{B} . The electronic spin couples

to the magnetic field through its magnetic moment given by,

$$\vec{\mu} = g_S \mu_B \vec{S} = \gamma_S \hbar \vec{S}, \quad (2.28)$$

where $\gamma_S = g_S \mu_B / \hbar$ is the gyromagnetic ratio of the electron, and \vec{S} is the spin operator that is expressed in Cartesian coordinates as,

$$\vec{S} = S_x \hat{x} + S_y \hat{y} + S_z \hat{z}, \quad (2.29)$$

with S_x , S_y , and S_z representing the unnormalised Pauli spin matrices. The interaction between the magnetic dipole and the field is expressed by the Hamiltonian,

$$\mathcal{H}_B = -\vec{\mu} \cdot \vec{B} = -\gamma_S \hbar \vec{S} \cdot \vec{B}. \quad (2.30)$$

The state of the atom is delineated by the wavefunction $|\psi(t)\rangle$ that can be decomposed in terms of the basis $\{|+\rangle_z, |-\rangle_z\}$ in allusion to the $m_s = +1/2$ and $m_s = -1/2$ spin states along the z -axis. The Schrödinger equation describes the evolution of this wavefunction through the interaction Hamiltonian in the following way,

$$i\hbar \frac{\partial}{\partial t} |\psi(t)\rangle = \mathcal{H} |\psi(t)\rangle. \quad (2.31)$$

The solution to Eq. (2.31) for the magnetic interaction can be given in terms of the unitary operator $U(t) = e^{-i\mathcal{H}_B t / \hbar}$ such that,

$$|\psi(t)\rangle = U(t) |\psi(0)\rangle = e^{-i\gamma_S \vec{S} \cdot \vec{B} t} |\psi(0)\rangle, \quad (2.32)$$

where $|\psi(0)\rangle$ describes the initial state of the atom. Consider the case in which the spin state is optically pumped along the x -axis such that $|\psi(0)\rangle \equiv |+\rangle_x$ in the absence of an external magnetic field. The rotation matrices can be adopted to view the system in the reference frame along the quantisation axis \hat{z} , defined by a magnetic field \vec{B} that is switched on at a time $t = 0$ immediately after pumping. The state vector can thus

be written as,

$$|+\rangle_x = \frac{1}{\sqrt{2}}(|+\rangle_z + |-\rangle_z). \quad (2.33)$$

As described in Eq. (2.32) the state will evolve under the action of the magnetic field as follows [44],

$$|\psi(t)\rangle = \frac{1}{\sqrt{2}}(e^{i\omega_L t/2} |-\rangle_z + e^{-i\omega_L t/2} |+\rangle_z), \quad (2.34)$$

where we have neglected electric field interactions that would be required to probe the atomic ensemble. Thus, the spin projection along the x -axis can be calculated as,

$$\langle S_x \rangle = \frac{1}{2} \cos(\omega_L t). \quad (2.35)$$

It can be seen that the absorption coefficient and refractive index of the sample will be modulated at the frequency ω_L , caused by Larmor precession. Therefore, the ensuing optical signal contains information about the strength of an external magnetic field when either the intensity or polarisation of the transmitted light is monitored.

2.3.2 Zeeman effect

The interaction between the magnetic field generated by an orbiting electron and the nuclear spin leads to hyperfine splitting of the atomic spectra with total angular momentum F . These hyperfine levels are composed of $2F + 1$ magnetic m_F sublevels, the degeneracy of which can be broken under the action of an externally applied field as previously discussed. Hence, the interaction Hamiltonian in Eq. (2.30) can be extended to include the contributions from the orbital and nuclear spin components in the following way,

$$\begin{aligned} \mathcal{H}_B &= \frac{\mu_B}{\hbar} (g_S \vec{S} + g_L \vec{L} + g_I \vec{I}) \cdot \vec{B} \\ &= \frac{\mu_B}{\hbar} (g_S S_z + g_L L_z + g_I I_z) B_z, \end{aligned} \quad (2.36)$$

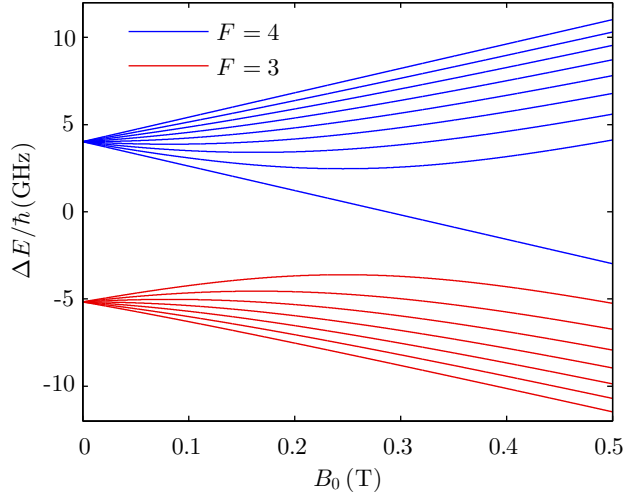


Figure 2.7: Breit-Rabi diagram describing the energy level splittings of the m_F magnetic sublevels comprising the Cs hyperfine ground states. The dependence is linear at low field strengths, known as the Zeeman effect. Small nonlinearities can occur for bias fields on the order of tens of μT , and become more apparent larger fields.

where g_S , g_L , and g_I are the electron spin, electron orbital, and nuclear g -factors which are proportionality constants that relate to the magnetic moments associated with each particles angular momentum. The values of g_S and g_I have been measured experimentally whereas g_L is approximately equal to 1 with a slight modification contingent on the nuclear mass [39]. The magnetic field has been considered to be aligned along the z -direction in this instance.

If the magnetic field strength is sufficiently low that the induced energy shift is small compared to the fine-structure splitting, then the interaction Hamiltonian can be described in terms of the total angular momentum J as follows,

$$\mathcal{H}_B = \frac{\mu_B}{\hbar} (g_J J_z + g_I I_z) B_z, \quad (2.37)$$

where the Landé g -factor g_J can be expressed in the simplified form,

$$g_J \simeq \frac{3J(J+1) + S(S+1) - L(L+1)}{2J(J+1)}. \quad (2.38)$$

The Hamiltonian can be simplified further when the magnetic field produces an energy shift smaller than the hyperfine splittings so that F is a good quantum number. This results in the energy level splitting ΔE following a linear dependence,

$$\Delta E_{|F, m_F\rangle} = \frac{\mu_B}{\hbar} g_F m_F B_z, \quad (2.39)$$

where the g -factor g_F is expressed as,

$$g_F \simeq g_J \frac{3F(F+1) + I(I+1) - J(J+1)}{2F(F+1)}. \quad (2.40)$$

This is known as the Zeeman effect and is one of the most widely utilised assumptions of atomic magnetometers. The analogous classical effect is the well-known Larmor precession, describing the rotation of a macroscopic spin vector around an external magnetic field.

Atomic magnetometers are highly sensitive devices employed in the detection of extremely weak magnetic field perturbations. Stronger field strengths can give rise to second order effects which can be described analytically by the Breit-Rabi formula [63],

$$E_{|F=I+1/2, m_F\rangle} = -\frac{\Delta E_{hfs}}{2(2I+1)} + g_I \mu_B m_F B \pm \frac{\Delta E_{hfs}}{2} \left(1 + \frac{4m_F x}{2I+1} + x^2 \right)^{1/2}, \quad (2.41)$$

where $\Delta E_{hfs} = A_{hfs}(I+1/2)$, A_{hfs} is the magnetic dipole constant, and the parameter denoted x is given by,

$$x = \frac{(g_J - g_I) \mu_B B}{\Delta E_{hfs}}. \quad (2.42)$$

The nonlinear dependence with field amplitude is noticeable even in the geomagnetic field range, and can heavily influence the response of an atomic magnetometer. It should be noted that $x \ll 1$ at bias fields close to that of the Earth's ($\sim 50 \mu\text{T}$) allowing a Maclaurin series to be applied to Eq. (2.41). Expanding to the second order terms we

find,

$$\begin{aligned}
 E_{|F=I+1/2, m_F\rangle} &= \Delta E_{hfs} \left(-\frac{1}{2(2I+1)} \pm \frac{1}{2} \right) \\
 &+ g_I \mu_B B m_F \pm \frac{(g_J - g_I) \mu_B B m_F}{2I+1} \\
 &\pm \frac{(g_J - g_I)^2 \mu_B^2 B^2}{4\Delta E_{hfs}} \mp \frac{(g_J - g_I)^2 \mu_B^2 B^2 m_F^2}{(2I+1)^2 \Delta E_{hfs}}.
 \end{aligned} \tag{2.43}$$

The precession frequency is governed by the energy spacing between adjacent m_F states; therefore, neglecting the constant terms allows Eq. (2.43) to be expressed as [1],

$$E_{|F=I+1/2, m_F\rangle} = (-g_I \mu_B \pm \mu_E) B m_F \mp \frac{\mu_E^2 B^2 m_F^2}{\Delta E_{hfs}}, \tag{2.44}$$

$$\mu_E = \frac{(g_J - g_I) \mu_B}{2I+1}. \tag{2.45}$$

Using Eq. (2.44) to calculate the energy spacing between neighbouring m_F states whilst considering only the linear component gives rise to the definition of the Larmor precession frequency,

$$\omega_L = \frac{(g_I \mu_B \pm \mu_E) B}{\hbar}, \tag{2.46}$$

where we can introduce the gyromagnetic ratio for the ground state as being $\gamma = \pm g_I \mu_B / (2I+1)\hbar$. The sign indicates an opposite phase in the precession of both hyperfine levels, and this has crucial implications in magnetometry as it causes decoherence through spin-exchange between colliding atoms in different ground states. The quadratic component in Eq. (2.44) can be thought of as breaking the degeneracy between the transition frequencies and gives rise to quantum beats that oscillate at a low frequency given by [1],

$$\omega_{rev} = \frac{\mu_E^2 B^2}{\hbar \Delta E_{hfs}}. \tag{2.47}$$

This beat frequency would have a value of $\omega_{rev}/2\pi = 3.3\text{Hz}$ for Cs in a magnetic field of $50\mu\text{T}$ thus is too low as to be resolvable using the miniaturised vapour cells considered here, with ms-timescale spin-coherence lifetimes. On the other hand, the nonlinear component can have a detrimental impact on the accuracy of the magnetometer readout through heading error which commonly features as a systematic error resulting from changes in the sensor orientation with respect to the field. The nature of this effect stems from the distortions in the resonance spectrum that manifest when the pumping direction is not perfectly aligned along the sensitive axis. The change in optical pumping conditions alters the sublevel populations and, in turn, their relative transition strengths causing asymmetries in the magnetic lineshape. The resultant shift in the precession frequency will be on the order of the quantum beat revival frequency ω_{rev} [1].

2.4 Spin Relaxation

2.4.1 Depolarising mechanisms

One of the primary contributions to spin relaxation in an optically pumped alkali vapour is the destruction of the atomic polarisation after hitting the cell walls. In this process the atoms adhere to the surface, for a characteristic adsorption time in the μs -regime, whereby fluctuations in the local magnetic field randomise their spin orientation [1]. In the absence of other species, the time of flight of an alkali atom before striking the cell surface is given by [64],

$$t_{wc} = \frac{4V}{\bar{v}A}, \quad (2.48)$$

where V and A are the volume and surface area of the vapour cell respectively, and the thermal velocity of the Cs atoms is defined as,

$$\bar{v} = \sqrt{\frac{8k_B T}{\pi m}}, \quad (2.49)$$

where m is the mass and T is the temperature. In the absence of a buffer gas, the wall collision rate for the MEMS cells considered here (see Section 2.2) would be close to $1/t_{wc} \simeq 2\pi \cdot 30 \text{ kHz}$ at a temperature of 85°C hence would be effectively unusable as a magnetic sensing element.

There are a variety of methods commonly adopted to extend this coherence time including: applying an antirelaxation coating enabling up to 2000 wall collisions before depolarisation [21], atom cooling and trapping [50], or the inclusion of an inert buffer gas that slows down atomic diffusion [65]. The latter is predominantly employed in MEMS cells due to ease of fabrication and simplicity in system operation compared to the other techniques. This extends to the vapour cells used in this work which contain N_2 to aid in minimising the relaxation rate, with the additional benefit of acting as a quenching gas to suppress reabsorption of spontaneously emitted photons through radiation trapping [51]. Atoms will experience diffusive motion in the presence of a buffer gas such as N_2 , thus the decay in spin polarisation can be solved numerically for arbitrary geometries using the diffusion equation [66]. However, a simpler analytical expression that assumes a cylindrical cell cavity is given by [67],

$$R_{wc} = \left[\left(\frac{\pi}{d} \right)^2 + \left(\frac{2.405}{r} \right)^2 \right] \frac{n_0 D_0}{\eta_{\text{N}_2}} \sqrt{\frac{T}{273.15 \text{ K}}}, \quad (2.50)$$

where d and r are the thickness and radius of the vapour cell respectively, D_0 is the diffusion constant of Cs atoms in the buffer gas (given at 1 amg^3 and 273.15 K), η_{N_2} is the buffer gas number density, and $n_0 = 1 \text{ amg}$ is the Loschmidt constant. This analytical expression serves as a useful approximation for estimating the wall relaxation rates for the MEMS vapour cells proposed here.

As well as reducing the wall relaxation rate, buffer gas atoms can also induce further relaxation through spin-destruction collisions as described by the following expression,

$$R_{\text{N}_2} = \eta_{\text{N}_2} \sigma_{\text{Cs-N}_2} \bar{v}_{rel}, \quad (2.51)$$

³An amagat (amg) is a practical unit for the number density of an ideal gas at atmospheric pressure and a temperature of $T = 273.15 \text{ K}$.

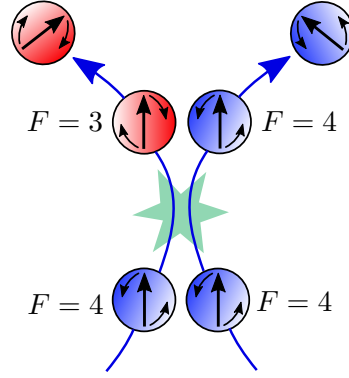


Figure 2.8: Schematic illustrating a spin-exchange collision between two alkali-metal atoms that are precessing in the presence of a magnetic field. The occupied ground state hyperfine levels, depicted by different colors, define the handedness of rotation. One of the atoms changes hyperfine state after the interaction whilst preserving the total angular momentum in the system, causing decoherence as the atoms precess in opposite directions.

where $\sigma_{\text{Cs}-N_2}$ is the effective collisional cross-section of Cs atoms in the buffer gas, and \bar{v}_{rel} is the relative thermal velocity between the two species [68]. This can be calculated using Eq. (2.49) with the reduced mass,

$$M = \frac{m_1 m_2}{m_1 + m_2}, \quad (2.52)$$

where m_1 and m_2 denote the mass of the Cs atoms and buffer gas molecules, respectively. It can be seen from Eq. (2.51) that the decoherence rate R_{N_2} increases linearly with buffer gas density, and thus demonstrates a pressure dependence. Therefore, for a particular cell geometry there exists an optimised buffer gas pressure that occurs when the wall and buffer gas induced relaxation rates are approximately equal.

As well colliding with buffer gas atoms, the alkali spins can collide with each other resulting in another possible source of depolarisation. The most common type of alkali-alkali collision is caused by spin-exchange in which the total spin of the atomic ensemble is conserved. This process is illustrated diagrammatically in Fig. 2.8. One or both of the atoms can change hyperfine state during the collision, thus a redistribution in the occupied m_F Zeeman states occurs to preserve the angular momentum [1]. This is typically the dominant source of relaxation particularly among thermal vapour cells

as there is a strong temperature dependence. The rate of spin-exchange collisions is given by,

$$R_{se} = \eta q_{se} \sigma_{se} \bar{v}, \quad (2.53)$$

where η is the Cs vapour density, σ_{se} is the spin-exchange cross-section, and q_{se} is the spin-exchange broadening factor as described in [1], by Seltzer. For Cs atoms at high magnetic fields, this factor is simply $q_{se} = \frac{7}{32}$; however, at the limit of zero field, $q_{se} \rightarrow 0$, and spin-exchange no longer affects the coherence lifetime leading us to the definition of the SERF regime.

As spin-exchange collisions are effectively suppressed in the SERF regime, the next crucial mechanism that contributes to depolarisation is spin-destruction collisions that do not preserve the total spin polarisation. The total spin-destruction collision rate between alkali atoms is represented by the relation,

$$R_{sd} = \eta q \sigma_{sd} \bar{v}, \quad (2.54)$$

where σ_{sd} is the spin-destruction cross-section, and q is the nuclear slowing down factor describing the degree to which spin coherence is maintained based on the atomic polarisation generated in the atomic ensemble e.g. $q = 1/8$ at high polarisations [1]. Spin-destruction collisions between alkali atoms are less frequent than spin-exchange as the cross-section is around two orders of magnitude smaller. Therefore, these collisions are only a concern if spin-exchange is suppressed by operating in the either the SERF or light-narrowing regimes [69, 70]. This is not the case for the magnetometry configurations discussed in this work hence spin-exchange is the dominant relaxation mechanism. Although this degrades the precision of the sensor, it also improves the magnetometer's response to rapidly varying fields and can be utilised as a method of tuning the atomic bandwidth by simply altering the cell temperature.

All of the relaxation processes discussed thus far are inherent to the sensor head itself thus the typical nomenclature is termed as “intrinsic”. We can accumulate the

effects of these individual decoherence phenomena to provide the expressions,

$$\gamma_{10} = R_{wc} + R_{N_2} + R_{sd}, \quad (2.55)$$

$$\gamma_{20} = \gamma_{10} + R_{se}, \quad (2.56)$$

where γ_{10} is the longitudinal relaxation rate comprising of contributions that will cause the spin vector to align itself along the magnetic field axis. Decoherence in the ground state manifold is described by the transverse relaxation rate γ_{20} that is composed of both the longitudinal and spin-exchange components. The terminology arises as spin-exchange only effects coherence between the Zeeman sublevels in the ground state manifold, thus acting transversely to the magnetic field direction. Equation (2.56) bestows all the necessary information to adequately characterise the spin relaxation mechanisms in a specified vapour cell, and is extremely useful in inferring the best sensitivity achievable. However, system optimisation requires consideration of operational contributions to spin depolarisation through mechanism such as magnetic field gradients and power broadening.

2.4.2 Light narrowing

Resolution is an ideal figure of merit for an atomic magnetometer, and can be expressed phenomenologically in terms of the SNR and spin relaxation rate in the following way [71],

$$\delta B = \frac{1}{\gamma} \frac{\gamma_2}{A/\sigma}, \quad (2.57)$$

where A and σ are the signal amplitude and noise level at the precession frequency. Rather intuitively, it can be seen that the sensor becomes more sensitive by lowering the decoherence rate and enhancing the SNR. Both these quantities are influenced by various experimental parameters including the frequency, intensity and polarisation of the light source, spectroscopic properties of the vapour cell, and the number of interacting atoms. Raising the vapour density by elevating the cell temperature is a common

method used to increase the signal amplitude. However, the sensitivity does not monotonically improve in the same way as the rising frequency of spin-exchange collisions can degrade the sensor precision as seen in Eq. (2.57).

The effects of spin-exchange collisions on the magnetic resonance can be understood by studying the energy level diagram in Fig. 2.9, depicting all Zeeman sublevels in the hyperfine manifolds of the Cs D₁ line. The observed populations serve to illustrate the steady state that may occur after optically pumping the sample with a strong intensity circularly polarised light beam using different frequency detunings. We are assuming a collisionally broadened optical spectrum in which only the ground state resonances are resolvable and are slightly overlapping, representative of the vapour cells utilised here. As described in Section 3.5 for a spin-1/2 system, there will be an enhancement in the magnetic quantum number by +1 after each excitation imposed by a σ^+ light beam. Eventually all of the atomic population would occupy the stretched state in the absence of other relaxation mechanisms. This picture is not strictly true as each hyperfine manifold is composed of $2F + 1$ Zeeman sublevels and there will typically be some redistribution of atomic population to lower quantum numbers, especially as the magnetic field acts transversely to the beam propagation direction [72]. More crucially, atoms that decay into the $F = 3$ ground state during optical pumping do not contribute to the magnetometer signal, and will precess in the opposite direction causing spin-exchange collisions with atoms in the $F = 4$ manifold. The destructive action of these collisions can be inhibited by operating in the SERF regime to actively eliminate this effect by working near zero-field at very high vapour densities. Unfortunately, the excessing power requirements for cell heating and limitation of low-field operation place strict restrictions on the applicability of the sensor.

An alternative method of suppressing spin-exchange relaxation has been shown using the light-narrowing phenomenon which can be utilised in Earth's field conditions and does not require the high vapour cell temperatures necessary for the SERF regime. This mode of operation can be implemented in different ways; however, the underlying premise is to repump atoms that have decayed into the $F = 3$ manifold, thus ensuring they remain within the optical pumping cycle. A greater number of

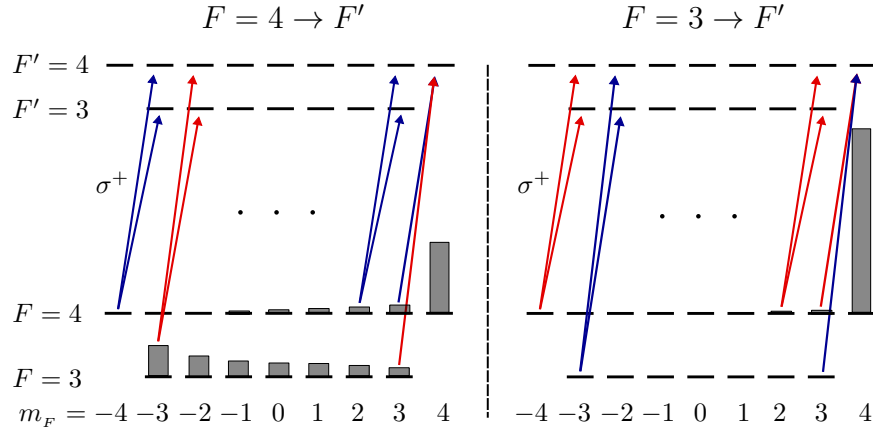


Figure 2.9: Steady state population generated by optical pumping with the laser frequency tuned to the $F = 4 \rightarrow F'$ (left) and $F = 3 \rightarrow F'$ (right) transitions of a collisionally broadened optical spectrum with overlapping ground state resonances. The blue and red arrows indicate a strong and weak light-atom interaction, respectively. The populations shown have been adapted from [70], by Scholtes *et. al.*

atoms can then be pumped into the $|F, m_F\rangle = |4, 4\rangle$ state resulting in significant signal enhancement. Most of the atoms will occupy the $F = 4$ stretched state under these conditions, thus spin-exchange is inhibited as the hyperfine levels cannot be scrambled whilst preserving angular momentum by redistributing the occupied Zeeman states as in most instances. The most efficient method of depopulating the $F = 3$ manifold is to individually pump the $F = 3 \rightarrow F'$ transition with a separate repump beam [71]. Nonetheless, light-narrowing has been achieved in a single-beam configuration using a high intensity, circularly polarised light beam in the M_x configuration [70]. This is possible as collisional broadening causes an overlapping resonance structure evident in many buffer gas vapour cells (see Section 2.2.3). As seen in Fig. 2.9, a high degree of spin polarisation can be generated in the $F = 4$ manifold by depopulating the $F = 3$ ground state when tuned closely to the $F = 3 \rightarrow F'$ transition. The atomic spins are simultaneously probed with a weak light-atom interaction as the laser frequency is adequately detuned from the $F = 4 \rightarrow F'$ resonance, thereby reducing power broadening. The efficiency of hyperfine repumping is dependent on the strength of the light-atom interaction [72], and will be highly affected by the characteristics of the light source as well as the optical resonance structure [73]. Evidence of light-narrowing has only been

Chapter 2. General Magnetometry Theory

shown for circularly polarised light of high optical intensity. Single-beam configurations based on optical rotation measurements require a linearly polarised component in detection hence elliptically polarised light is often employed as a compromise, as is the case for the magnetometry schemes considered in this work. Narrowing of the magnetic resonance has been observed for increasing light intensities; however, the dependence on light polarisation has not yet been explored.

Chapter 3

Free-Induction-Decay Magnetometry

In this chapter we present the application of the FID technique with a microfabricated Cs vapour cell by varying the strength of the light-atom interaction to independently pump and probe the atomic ensemble with a single laser beam. This is implemented using either amplitude-modulation (AM) by switching the light intensity from high to low, or alternatively applying frequency-modulation (FM) in which the laser wavelength is oscillated on and off resonance with an optical transition. A detailed review comparing the sensitivity performance of both configurations is provided in [24], by Hunter *et. al.* It should be noted that these modulation techniques are special cases of a perturbation implemented by optical pumping, and that other sources of modulation can be applied. The FM scheme is highly scalable as the modulation is controlled entirely by the VCSEL, and can exhibit similar performance to the M_x magnetometer with the added advantage of being fully optical [13]. This is particularly beneficial in applications that require multiple adjacent sensors as crosstalk is not an issue.

The signal processing methods that are applied to extract the precession rate from the damped sinusoids characteristic of FID traces are discussed in detail. Also, the concept of differential polarimetry detection in a FID setting is described as well as the efficiency of single-pulse and synchronous optical pumping. Finally, the relative

sensitivity performance in a static field of similar magnitude to that of the Earth’s is measured for both configurations. This is determined through calculation of the Cramér-Rao lower bound (CRLB) for a single FID trace, and also by examining the root spectral density (RSD) of the magnetic field tracked by subsequently extracting the Larmor frequency from each FID trace in a signal train.

3.1 Principles of Operation

FID is a well-understood phenomenon with the first optically detected signal in an alkali-metal vapour achieved by Dehmelt [74], who demonstrated that the precession of sodium atoms generated by an external magnetic field would induce a modulation in the absorption of a circularly polarised probe. This was adequately described using the Bloch formalism with the evolving macroscopic magnetisation altering the absorption coefficient of the atomic vapour. The FID mechanism is also conveniently utilised in numerous nuclear magnetic resonance (NMR) experiments that manipulate nuclear, rather than electronic, spins [75]. Analogies in the model, observed data, and signal-

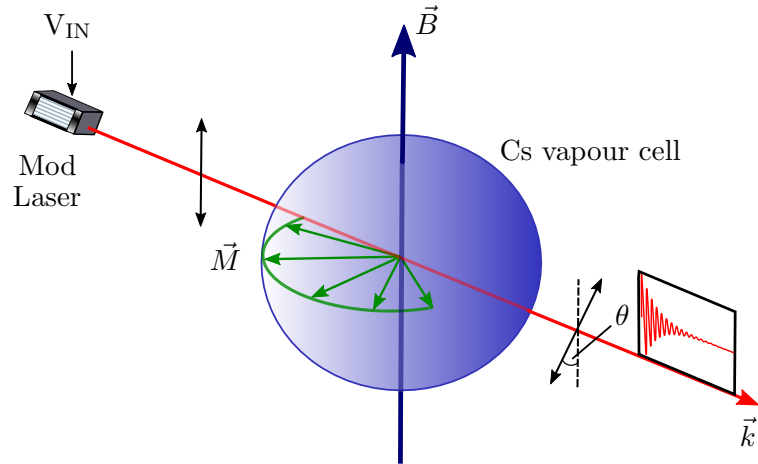


Figure 3.1: Experimental model conveying the basic mechanisms behind the FID magnetometer. In the AM scheme, the laser intensity is modulated to alter the absorption coefficient. A strong light-atom interaction builds up spin polarisation for a pumping time T_p during the pump phase. The interaction strength is then lowered for a probe duration T_r and the time-dependent optical rotation angle is monitored. Alternatively, the laser frequency can be modulated as in the FM implementation.

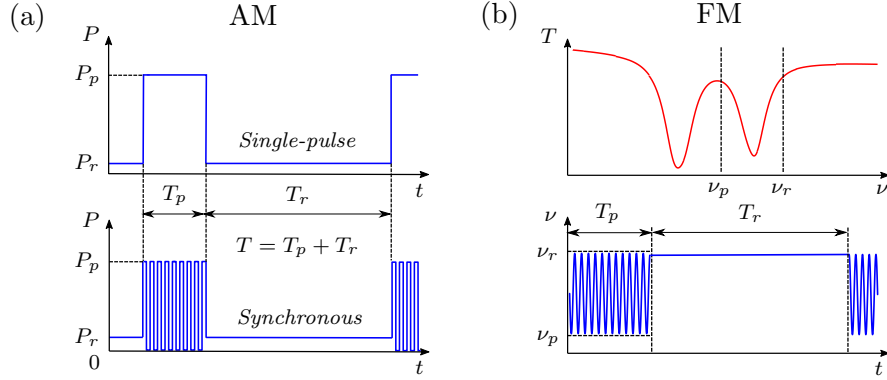


Figure 3.2: (a) Diagram illustrating switching of the laser power from high to low in the AM scheme. Two possible modulation inputs (single-pulse or synchronous) can be applied to the modulator with a single pump-probe cycle occurring at the driving frequency $f_d = 1/T$. (b) Spectroscopic signal illustrating the pump ν_p and probe ν_r frequencies used in the FM implementation. Laser frequency is sinusoidally modulated over the $F = 3 \rightarrow F'$ transition in the synchronous regime. A single pulse can also be applied by setting ν_p to the centre of the resonance peak.

processing techniques can all be drawn from this highly recognised field.

The physical principles behind the FID magnetometer are conveyed in Fig. 3.1 encompassing both the AM and FM configurations. Optical pumping with circularly polarised light generates a population imbalance in the Zeeman levels of the hyperfine ground state, which classically is analogous to the creation of a net magnetisation \vec{M} along the direction of the laser beam. An external magnetic field will induce Zeeman splitting of the hyperfine ground states resulting in precession of the magnetisation at the Larmor frequency $\omega_L = \gamma |\vec{B}|$, where $\gamma/2\pi = 3.5 \text{ Hz/nT}$ is the gyromagnetic ratio of the Cs atomic ground state. In the AM scheme, the laser intensity is raised to a peak pump power P_p for a time T_p enabling the build-up of spin coherence in the atomic ensemble, equivalent to optical pumping. This process can be made more efficient by employing synchronous modulation where the light intensity is modulated at the Larmor frequency or one of its subharmonics [34]. The light level is then reduced to a readout power P_r for a detection time T_r to adequately monitor the precession whilst reducing perturbations through residual optical pumping. Figure 3.2(a) demonstrates the implementation of AM in a FID setting showing the two possible modes of optical pumping: single-pulse and synchronous. The magnetometer bandwidth is limited to

half the repetition rate of the sensor, also referred to as the driving frequency $f_d = 1/T$, in accordance with the Nyquist theorem.

For the FM implementation the laser frequency is sinusoidally modulated at the Larmor frequency during the pump phase as shown in Fig. 3.2(b). The centre frequency of the sinusoidal waveform was very close to the absorption peak in this case; hence, one might expect the strongest resonance to occur at a modulation frequency of $\omega_L/2$ as observed in typical Bell-Bloom configurations [13]. This is not the case as the broadened optical linewidth causes simultaneous excitation of all the hyperfine transitions, with the optimised modulation frequency residing at ω_L as discussed in Section 3.6.2. The probe is blue-detuned to the side of the $F = 3 \rightarrow F'$ resonance producing a weak light-atom coupling that is analogous to the low-intensity stage considered in the AM configuration. Optimisation of the probe frequency is fairly straightforward as it simply requires sufficient detuning from the optical resonance to avoid extensive power broadening¹.

3.2 Experimental Set-up

A schematic of the experimental arrangement, applicable to both the AM and FM implementations, is illustrated in Fig. 3.3. The sensing element consists of a micro-fabricated Cs vapour cell, the details of which are presented thoroughly in Section 2.2. The buffer gas pressure that minimises the spin decoherence rate, based on the cell geometry, was calculated to be close to 300 Torr at 85 °C. Unfortunately no vapour cells containing this quantity of nitrogen were available due to difficulties in the fabrication process; therefore, cells with pressures in the region of 150-200 Torr were used². The vapour cell temperature is controlled by passing a gated current through a resistive heating element, with measurements performed during the off state to avoid spurious magnetic field contributions. Increasing the cell temperature will improve the SNR as the atomic density rises. However, this will also reduce the spin lifetime due to the

¹Broadening of the magnetic resonance is inevitable at the probe powers used in this work. There is a trade-off between the SNR and spin decoherence rate that can be tuned with probe frequency.

²The transverse relaxation rate is an excellent indicator of the potential sensitivity achievable from a specific vapour cell.

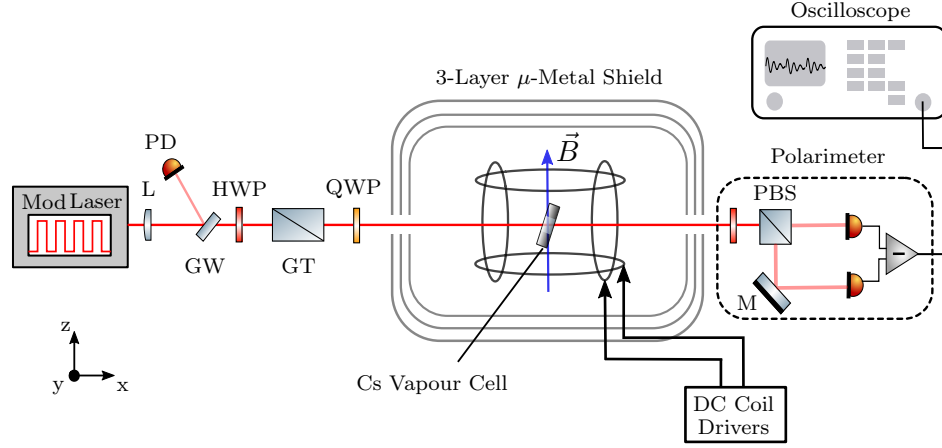


Figure 3.3: Experimental set-up for a FID magnetometer with a microfabricated Cs vapour cell containing N_2 buffer gas with typical pressures between 150-200 Torr. AM is achieved using an AOM whereas FM is achieved by modulating the injection current of a VCSEL. The direction and magnitude of \vec{B} is controlled by passing currents through each Helmholtz coil. (L, lens; GW, glass window; PD, photodiode; GT, Glan-Thompson polariser; PBS, polarising beam splitter; HWP, half-wave plate; QWP, quarter-wave plate; M, mirror.)

higher number of collisions. The counterplay of these two parameters results in the best sensitivity occurring at approximately 85°C for the thermal vapour cells and probe intensity considered here. The sensor head is placed inside a three-layer μ -metal shield, nulling the ambient magnetic field to several nT and highly suppressing technical noise contributions. A set of two-axis Helmholtz coils driven by a stable direct current (DC) supply (powered by a 12-V car battery) were designed to generate a uniform bias field, surpassing that of the Earth's ($\sim 50\ \mu\text{T}$), pointing along a user-defined direction in the x - z plane. An extended cavity diode laser (Toptica DL 100) is manually tuned to the D_1 line using the set-up shown in Fig. 2.6(b) which contains an auxiliary Cs reference cell. The fiber-coupled output is passed through a half-wave plate and Glan-Thompson polariser to ensure maximum transmission of linearly polarised light through the transmitted channel. The quarter-wave plate then introduces an adjustable circular component before illuminating the vapour cell. Laser power is varied using the first-order deflection of an acousto-optic modulator (AOM) output driven by a frequency mixer; the control voltage input is provided by a programmable arbitrary function generator

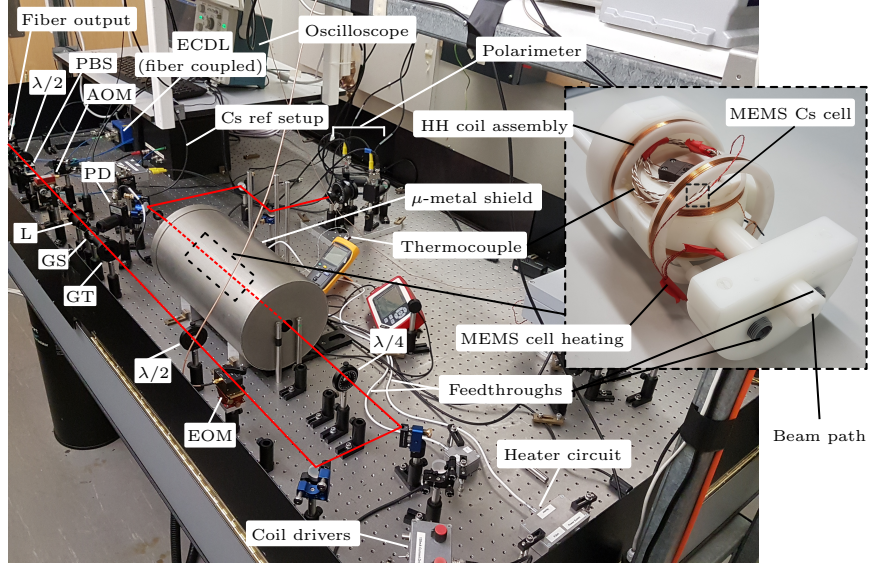


Figure 3.4: Photograph of laboratory showing the FID magnetometer in the amplitude modulated regime. An AOM modulates the laser intensity, and polarisation modulation can also be implemented with the EOM. Several optical elements are used to condition the size and polarisation of the light beam. The three layer μ -metal shield contains an assembly that heats the MEMS Cs cell and produces the measurable field. The laser frequency is tuned with a respect to a Cs reference cell. The polarimeter measures optical rotation in the light polarisation that is acquired on the oscilloscope.

(Keysight 33500B series) and the RF input is supplied by a signal generator (Marconi 2022). The diameter of the beam entering the AOM is carefully managed to optimise the dynamic range with the lowest optical power on the order of $1 \mu\text{W}$. The pump and probe powers are monitored using reflection from a glass window with a calibrated photodiode. The probe power inside the vapour cell was kept at $P_r \simeq 200 \mu\text{W}$ with a measured beam diameter of 1.8 mm. The best sensitivity was achieved at the highest peak pump power, $P_p \simeq 6 \text{ mW}$, available from the laser after losses, suggesting that this is slightly below the optimum value in terms of system performance (see Section 3.5.2). The laser frequency was tuned close to the centre of the merged $F = 3 \rightarrow F'$ absorption line of the collisionally broadened two-peak hyperfine resonance as there was a clear signal enhancement and reduction in the decoherence rate, in comparison to the $F = 4 \rightarrow F'$ transition, resulting in an improved magnetometer sensitivity.

3.3 Signal Processing

3.3.1 FID signal sampling

FID is a unique branch of atomic magnetometry as the signal processing is performed in the time domain as opposed to more commonly adopted techniques that employ lock-in amplifiers in their analyses. As this technique monitors the precession directly, it presents significant advantages in accuracy over driven systems that can be subject to systematic frequency shifts imposed by phase errors in the feedback signal [32]. The FID mechanism is intuitively modelled by the Bloch equations, describing the evolution of the macroscopic magnetisation \vec{M} precessing in the plane transverse to the external magnetic field,

$$\dot{\vec{M}} = \gamma \vec{M} \times \vec{B} - \gamma_2 \vec{M}, \quad (3.1)$$

where γ_2 is the total polarisation decay rate comprising numerous contributions including depolarising collisions with the cell walls, spin exchange, and residual optical pumping effects [68]. This is of course a vectorial model that is only representative of a spin-1/2 system and does not take into account tensor (alignment) contributions generated by the high-intensity circularly polarised light beam [76]; however, the resulting time-dependent solutions are useful as they relate closely to experimental observations. A full treatment regarding the evolution of atomic polarisation can be modelled using the density matrix formalism describing the dynamics of the atomic ground state [77]. The optical rotation angle is proportional to the degree of spin polarisation along the beam propagation direction [16], that has the solution,

$$M_x(t) = M_0 \sin(\omega_L t + \phi_0) e^{-\gamma_2 t}, \quad (3.2)$$

which is a decaying sinusoid with a frequency corresponding to the precession experienced by the Cs atoms.

In a single measurement the signal $S(t)$ from the detector is recorded at a sampling

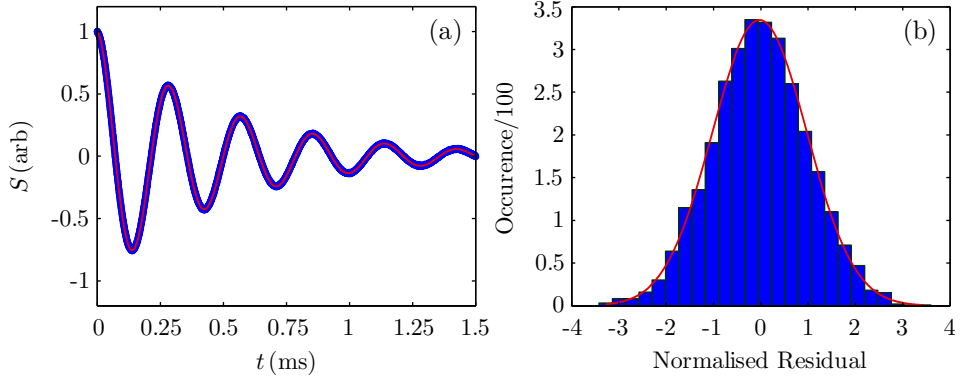


Figure 3.5: (a) Simulated FID signal (blue) corrupted with additive white Gaussian noise, and best fit (red) to a damped oscillator model using the LM algorithm. The damping rate and SNR were set to 2 kHz and 400 respectively, matching closely with experimental observations. The frequency of oscillation was 3.5 kHz. (b) Histogram of the fit residuals (blue) normalised with respect to the noise level, and associated fit to a Gaussian distribution (red).

rate f_s . This signal can be modelled as,

$$S(t) = g M_x(t) + \varepsilon(t), \quad (3.3)$$

where g is a transduction constant, $M_x(t)$ is the projection of the spins along the probe axis as described in Eq. (3.2), and $\varepsilon(t)$ represents signal noise. Data acquisition devices such as oscilloscopes convert the analogue signals generated by the detector into discrete samples; therefore, we can adjust our model to compensate for this quantisation in the following way,

$$S_n = A \sin(\hat{\omega}_L n + \phi_0) e^{-\hat{\gamma}_2 n} + \varepsilon_n, \quad (3.4)$$

where n symbolises the data point of interest, A is the sinusoid amplitude proportional to the magnetisation built-up during optical pumping, ϕ_0 is the initial phase, and ε_n is the signal noise with root mean square (RMS) error σ . The radian precession and spin relaxation rates are normalised with respect to the sampling rate as defined by the

expressions,

$$\hat{\omega}_L = \omega_L / f_s, \quad (3.5)$$

$$\hat{\gamma}_2 = \gamma_2 / f_s. \quad (3.6)$$

The damped sinusoidal (DS) signal presented in Fig. 3.5(a) was generated using the discrete model in Eq. (3.4) to conceptually visualise the anticipated evolution of the atomic spin precession. A pseudorandom number generator was employed to produce an additive white Gaussian noise sequence that emulated noise ε_n in the signal. The simulated data proves useful in identifying the resemblance of experimental observations with the theoretical model.

3.3.2 Discrete Fourier transform

A useful method to analyse any signal is to examine how its content is distributed in the frequency domain. This is performed by applying the Fourier transform that is expressed analytically as [78],

$$F(\nu) = \mathcal{F}[f(t)](\nu) \quad (3.7)$$

$$= \int_{-\infty}^{+\infty} f(t) e^{-2\pi i \nu t} dt, \quad (3.8)$$

where $f(t)$ and $F(\nu)$ are continuous functions describing a signal in the time and frequency domains, respectively. This can be generalised for the special case of a sampled signal such that $f(t) \rightarrow f(n/f_s)$, yielding the definition of the discrete Fourier transform (DFT),

$$F_k = \sum_{n=0}^{N-1} f_n e^{-2\pi i kn/N}, \quad (3.9)$$

where $f_n \equiv f(n/f_s)$, and k is an index denoting the frequency of interest e.g. $k = 0$ is equivalent to DC. The inverse DFT can be calculated as,

$$f_n = \frac{1}{N} \sum_{k=0}^{N-1} F_k e^{-2\pi i n k / N}. \quad (3.10)$$

DFTs are a powerful mathematical tool as they allow inspection of any periodicities in the signal along with the associated strength of these frequency components. For input data consisting of a sequence of real numbers, the associated DFT will likely produce a series of complex numbers of the same length. As a consequence of Euler's identity, a real sinusoid will consist of an equal contribution of negative and positive frequency components. This must be compensated for by doubling the strength of each positive component when applying a DFT as half the energy in that signal is lost to negative frequencies. It is also possible to apply the fast Fourier transform (FFT) by adjusting the length of the signal to a power of 2 which speeds up computation. This can be performed by artificially inputting zero values at the end of a data sequence to meet the specified length requirements in a process known as zero-padding.

3.3.3 Reliability of the fitting routine

The LM fitting algorithm is used extensively throughout this work to extract the relevant free-parameters from a FID signal. To demonstrate its reliability, the LM fitting routine was applied to a series of artificially generated and experimentally acquired FID signals. Simulated data was used in this instance as a means of determining the fit quality for data that is perfectly represented by the theoretical model, providing a useful comparison to experimentally acquired FID signals. One particularly useful method of assessing the quality of a fit is to calculate the reduced chi-squared statistic χ_r^2 that is minimised iteratively during the LM algorithm to extract the free-parameters resembling the best fit [62]. We can also assess if the fit residuals follow a normal distribution as is the case for the simulated data, shown in Fig. 3.5(b), and determine the fraction of points that lie within a single standard deviation of the mean. The fitting routine was applied to a total of 10,000 simulated FID traces resulting in an

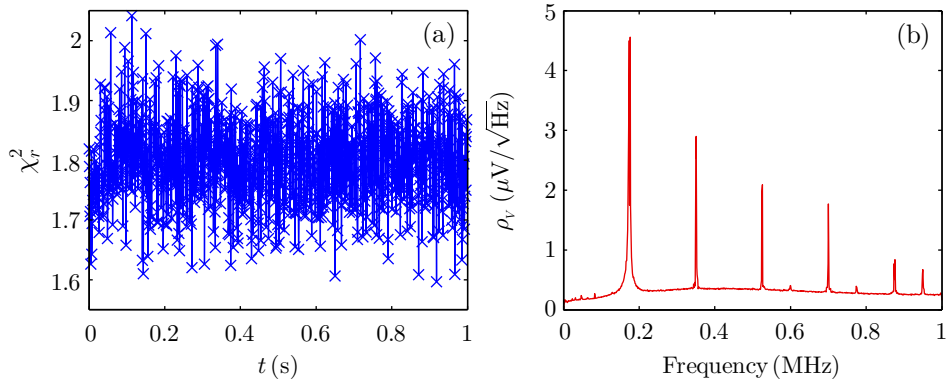


Figure 3.6: (a) Reduced chi-squared statistic (blue) calculated for a series of experimental FID traces in a signal train as a means of determining the quality of the fit. (b) Noise spectrum of the fit residuals (red) for experimentally acquired FID data. The peak at the precession frequency $\omega_L/2\pi \simeq 175$ kHz occurs as the theoretical model does not fully describe the signal lineshape. Higher order frequency components are also not accounted for.

average reduced chi-squared statistic $\chi_r^2 = 1$ with 68.3 % of the residuals residing within a single standard deviation. This corresponds exactly with the anticipated values that one would expect for simulated data using the appropriate fit model, and proves that the artificially generated noise is indeed white and equally distributed among all frequencies within the measurement bandwidth [62]. This suggests that the RMS error in the signal can be estimated from the standard deviation of the fit residuals in the time domain $\sigma = \sqrt{\text{Var}(\varepsilon_n)}$. The useful assumption that σ adequately represents the noise in each data point is valid for signals that are corrupted solely by white noise. In this case, estimation of the fit parameters and their associated errors is trivial. This is not always true for experimentally acquired data; therefore, in some instances a more vigilant approach to noise estimation is necessary.

The reduced chi-squared statistic calculated from a series experimental FID traces in a signal train using the LM algorithm is depicted in Fig. 3.6(a) to determine the appropriateness of the applied theoretical model. The average value was calculated to be $\bar{\chi}_r^2 = 1.8$ suggesting that the model does not perfectly reflect the experimental data. Further evidence of this fact is depicted in the spectrum of the fit residuals shown in Fig. 3.6(b). This spectrum was generated by averaging DFT spectra gained from

the residuals of multiple adjacent FID signals. This is possible as the residual trends remaining from the nonlinear fit are consistent in each FID trace. The residual component evident at the precession frequency $\omega_L/2\pi \simeq 175$ kHz is an indication that the lineshape of the signal is not Lorentzian as one would expect from a damped oscillator [78]. This slight distortion in the lineshape could be attributed to more complicated optical pumping dynamics present in buffer gas cells as multiple transitions can be excited simultaneously. Red-detuning the laser frequency with respect to the $F = 4 \rightarrow F'$ transition alleviates this issue somewhat; however, the achievable sensitivity degrades significantly. It is also clear that the model is not sensitive to the frequency components observed at multiples of the Larmor rate. These most likely arise due to higher order multipole moments induced in the spin polarisation during optical pumping, as a consequence of the high power elliptically polarised light beam [79,80]. Clear aliasing of frequency components that reside above the Nyquist limited bandwidth of $f_s/2$ are also observable. The higher order terms are not subject to the fitting process as they also appear in the raw signal, and are considerably smaller than the fundamental frequency component.

3.3.4 Noise estimation

Inferring the noise content within an experimentally acquired FID trace is extremely important in the analysis of that signal, especially when determining the SNR; a parameter prevalent in the evaluation of sensor performance. A particularly simple method is to calculate the differences in the response data and the nonlinear fit. This assumes the applied model is a perfect reflection of the observed data which is not always the case as depicted in Fig. 3.6(b). A more robust method is to measure the noise fluctuation of independent data points as displayed in Fig. 3.7(b). This data was formulated by subtracting the average of 10 adjacent FID traces in a signal train, presented in Fig. 3.7(a), from a single FID signal in the subset. This is an effective way of filtering out the precession to observe the noise independently. The number of FID signals used in averaging was arbitrary but should be limited to subsets not effected by low frequency drifts as this would interfere with our estimation. One must also take care in

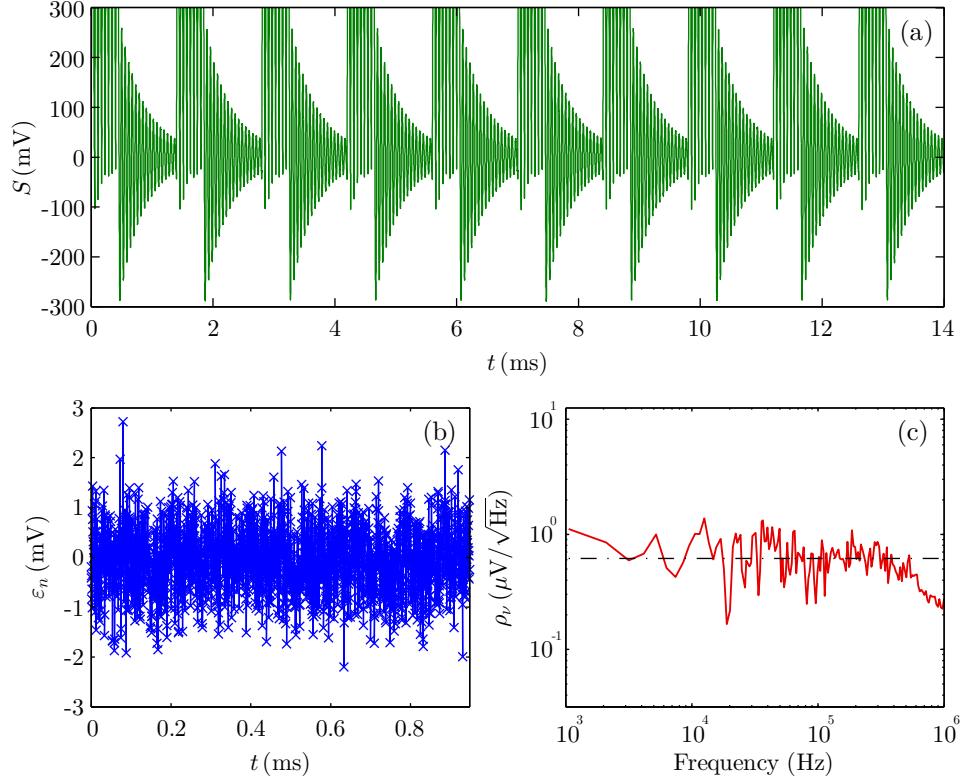


Figure 3.7: (a) Portion of a typical signal train (green) showing the first 10 FID traces. In this case, the driving frequency was set to $f_d \simeq 700$ Hz leading to signal truncation. (b) Noise data (blue) captured by subtracting the average from one of the FID traces in the subset. (c) Noise spectrum (red) associated with the time domain data. The black dashed line symbolises the noise floor, neglecting the high frequency rolloff that occurs as a consequence of the detection electronics bandwidth. This serves as an estimation of the noise level at the precession frequency, measured to be $\omega_L/2\pi = 17.2$ kHz.

the acquisition and triggering of the FID traces as slips in phase will resemble large fluctuations, resulting in a poor noise estimation. We commonly detected a beat oscillation observable in the initial phase of the FID traces when processing a signal train. This issue was easily resolved by using the modulation source as an external reference for data acquisition. A DFT was applied to convert the time domain noise data into the frequency domain providing the noise spectrum shown in Fig. 3.7(c). A simulated sinusoid was used to ensure the scaling of the DFT was correct. For better visualisation of the spectrum, the data was logarithmically binned and averaged using an arithmetic mean. It can be seen that in this example the noise level is approximately flat in the

frequency range of interest; slight rolloff is observed at higher frequencies as a consequence of the detection electronics bandwidth, which is easily adjustable.

The total RMS noise present in the signal can be estimated from the spectral density ρ_ν using the expression,

$$\sigma^2 = \int_0^{f_N} \rho_\nu^2 d\nu, \quad (3.11)$$

where $f_N = f_s/2$ is the Nyquist limited bandwidth equal to half the sampling rate. As we are concerned with discrete signals, the integral can be replaced by a summation. With regards to the spectrum in Fig. 3.7(c), it would be sufficient to assume that the RMS noise in each sample of the FID signal is adequately represented by σ and the nonlinear fit can be performed with equal weightings. In instances that this assumption is invalid, for example if amplitude noise is present in the signal, then the error weightings can be adjusted based on the standard deviation calculated for each data point from the subset of FID signals.

This approach to error estimation is robust but fairly cumbersome, and could not be applied when exposed to large amplitude or phase changes; such scenarios are common, especially in our investigation of the sensor's performance which requires varying external parameters. Amplitude noise is rarely a concern due to the excellent common-mode noise rejection of our detection system (see Section 3.4); hence, simpler techniques that apply the white noise assumption³ are often adopted. One such method is to measure the fluctuation at the end of the signal once it has fully equilibrated. This is not ideal as signal truncation optimises both the magnetometer bandwidth and sensitivity [24]. For this reason, the noise estimation algorithm provided in Appendix C.1 [61] is frequently employed as it can be applied to independent FID traces, even if truncated. One drawback is that the algorithm is predicated on discrete derivatives in the data; therefore, is only valid for signals that have sufficiently high sampling rates. This is evidenced by Fig. 3.8(a) which shows the ratio of the estimated and actual noise as a function of oscillation frequency for different sampling rates, using artificially generated FID data.

³Noise is referred to as white if it is randomly distributed with equal intensity at a range of frequencies, resulting in a constant spectral density.

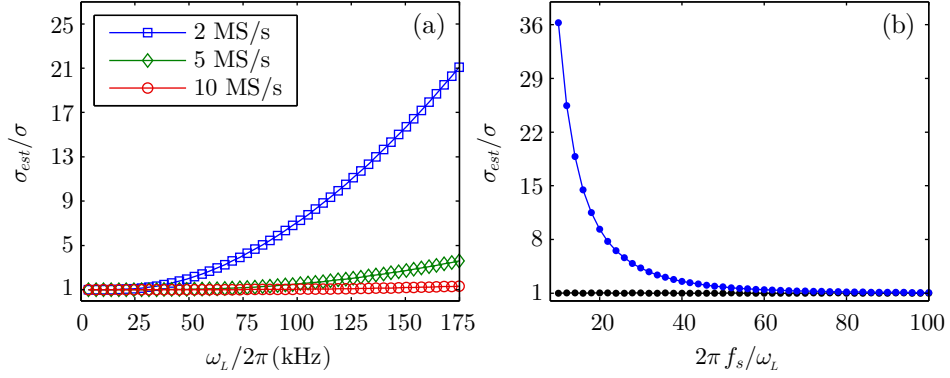


Figure 3.8: (a) Ratio of the estimated noise (using Eq. (C.1.6)) and the true noise over a range of frequencies using different sampling rates as noted in the legend. Simulated FID data was used with a SNR of 400. (b) Ratio calculated as a function of samples per cycle at a sampling rate of $f_s = 2$ MS/s. The algorithm was applied to both the data (blue) and its corresponding fit residuals (black). The ratio asymptotically approaches 1 at low frequencies for the raw data whereas it maintains a value of 1 when applied to the fit residuals.

It can be seen in Fig. 3.8(b) that the noise estimation algorithm starts to break down when the number of samples per cycle approaches less than 100 for the chosen SNR. This issue can be circumvented by, instead, applying the algorithm to the fit residuals, evidenced by the black data set in Fig. 3.8(b), which maintain a ratio of 1 over the full frequency range. Equivalently, we could have calculated the standard deviation of the fit residuals; however, the noise estimation algorithm is useful as it ignores residual trends (see Section 3.3.3) by measuring the high frequency noise in the signal. If the noise is predominantly white, then this method will provide a close approximation of the noise level at the precession frequency. This is extremely important in calculating parameter errors in the fitting routine, and also in our SNR estimation which allows an assessment of the magnetometer’s sensitivity performance.

3.3.5 Cramér-Rao lower bound: frequency estimation

The CRLB is a measure of the minimum statistical uncertainty of determining an unknown free-parameter from a signal (see Appendix C.2). The CRLB condition for an angular frequency extracted from a discrete damped sinusoid, in the limit of high

sampling rate, can be calculated as [81–83],

$$\sigma_{\hat{\omega}_L}^2 \geq \frac{24}{(A/\sigma)^2 N^3} C_2, \quad (3.12)$$

where A/σ is the SNR, N is the number of data points, and C_2 is a corrective factor that takes into account the signal decay given by [83],

$$C_2 = \frac{N^3}{12} \frac{(1 - z^2)^3 (1 - z^{2N})}{z^2 (1 - z^{2N})^2 - N^2 z^{2N} (1 - z^2)^2}, \quad (3.13)$$

where $z = e^{-\hat{\gamma}_2}$, and $\hat{\gamma}_2$ represents the normalised damping rate defined in Eq. (3.6). Converting the normalised Larmor frequency $\hat{\omega}_L$ to magnetic field provides the expression,

$$\sigma_B^2 \geq \frac{24}{\gamma^2 (A/\sigma)^2 N T_r^2} C_2, \quad (3.14)$$

where σ_B is the statistical uncertainty of measuring the field from a single FID trace. It should be noted that the correction factor approaches a minimum of $C_2 = 1$ in the case of an undamped sinusoid.

It can be readily seen from Eq. (3.14) that decoherence of the atomic spins will degrade the precision with which the field can be readily determined from a FID signal, as the correction factor C_2 rises with increasing relaxation rate. In fact, for a given damping rate γ_2 there exists an optimum detection time T_r that will minimise the CRLB condition. As a simplification, the correction factor can be written in terms of the number of decay periods $d = \gamma_2 T_r$ to provide the relation,

$$C_2 = \frac{2d^3 e^{2d} (e^{2d} - 1)}{3(1 - 2(1 + 2d^2)e^{2d} + e^{4d})}. \quad (3.15)$$

Expressing the probe time in terms of the decay number d , Eq. (3.14) can be rewritten as,

$$\sigma_B^2 \geq \frac{24 \gamma_2^2}{\gamma^2 (A/\sigma)^2 N d^2} C_2(d). \quad (3.16)$$

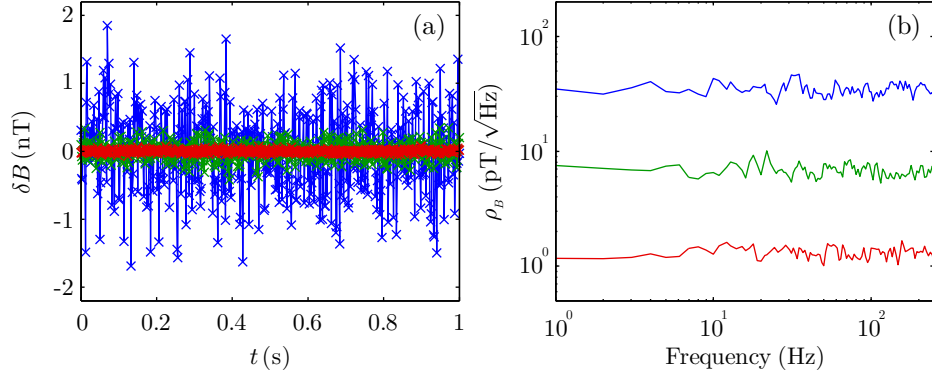


Figure 3.9: (a) Time series emulating magnetic field fluctuations generated by fitting a series of simulated FID traces to extract the precession frequency. A sampling rate of $f_s = 2$ MHz was used for a time $T_r = 1.5$ ms. The SNR's were set to 20 (blue), 100 (green), and 500 (red). The damping and precession rates were fixed at values of $\gamma_2 = 2$ kHz and $\omega_L/2\pi = 175$ kHz, respectively. (b) Noise spectra associated with the time series over a bandwidth of $f_d/2 = 250$ Hz. The noise floors were calculated to be 34.8 pT/√Hz (blue), 6.83 pT/√Hz (green) and 1.32 pT/√Hz (red).

Treating the decay rate γ_2 as a fixed parameter, it can be shown that σ_B is minimised when $d \simeq 2$ so that the optimum detection time is $T_r \simeq 2/\gamma_2$. In light of this, the best precision of extracting the field from a single FID trace is,

$$\sigma_{B_{opt}}^2 \geq \frac{6\gamma_2^2}{\gamma^2 (A/\sigma)^2 N} C_2. \quad (3.17)$$

It is possible to reduce the noise σ_B by averaging over successive magnetic field measurements extracted from a signal train; this would in turn decrease the magnetometer bandwidth. Therefore, it is useful to introduce the noise density ρ_B that is usually considered a more meaningful determination of the magnetometer performance as it contains additional information regarding the bandwidth of the measurement. It also allows one to observe the distribution of noise in the frequency domain. Assuming the noise is white, then the noise density can be expressed as,

$$\rho_B = \frac{\sigma_B}{\sqrt{f_d/2}} = \sigma_B \sqrt{2T}, \quad (3.18)$$

which is a valid assumption for noise spectra that are approximately flat. Equation (3.18) has been used extensively in our analysis of the magnetometer’s sensitivity.

There are numerous methods of extracting the frequency content from a precession signal. For example, a DFT can be applied to the time series although the optimum magnetic resonance linewidth achievable in microfabricated cells places a strict limit on the achievable frequency resolution. Also, applying the DFT to a full signal train results in numerous peaks with a frequency spacing equivalent to the repetition rate f_d , and the strongest peak occurring at a multiple of f_d closest to the precession rate. As described previously, we commonly utilise a nonlinear fit to a DS model as this is the most sensitive method of frequency extraction. Proof of this is shown in Figs. 3.9(a) and 3.9(b) which demonstrate the sensitivity of the fitting routine for different SNR’s in both the time and frequency domains. The data was collected by generating numerous simulated FID traces to emulate a signal train, and applying the fitting routine to extract the frequency from each. This produced the time series in Fig. 3.9(a) that serves to replicate magnetic field fluctuations. The time domain data was then converted using a DFT to form the noise density spectra shown in Fig. 3.9(b). Inserting the set parameters into Eq. (3.18), the CRLB sensitivities were calculated to be $38.1 \text{ pT}/\sqrt{\text{Hz}}$, $7.62 \text{ pT}/\sqrt{\text{Hz}}$ and $1.52 \text{ pT}/\sqrt{\text{Hz}}$ for SNR’s of 20, 100, and 500, respectively, which closely resemble the noise floors observed in the acquired spectra. Clearly, this demonstrates that a nonlinear fit is the most precise frequency extraction method as it can reach the CRLB condition; however, one must also consider the overall quality of the fit as this can impact both the precision, and accuracy, of the extracted frequency.

3.3.6 Zero-crossing frequency extraction

It was shown above that a nonlinear fit is the most precise method of extracting the precession frequency from a FID signal as it reaches the CRLB condition, assuming the theoretical model adequately represents the experimentally acquired data. Nonetheless, employing such complex mathematical algorithms is computationally intensive and extremely difficult to apply in hardware such as field-programmable gate arrays

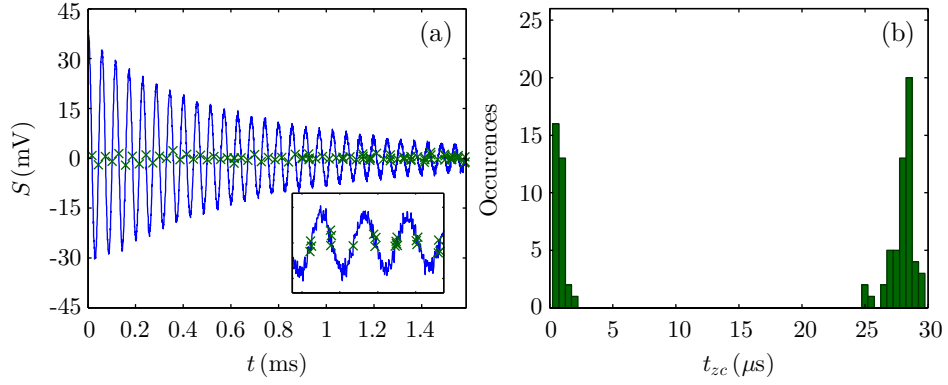


Figure 3.10: (a) FID trace (blue) acquired at a sampling rate of $f_s = 2$ MHz, and data points (green crosses) that occur immediately prior to a ZC. The inset shows numerous false instants that occur toward the end of the signal as a consequence of noise. (b) Histogram displaying the time interval between adjacent data points that are sampled before their respective ZCs. Spurious contributions arising from noise will appear at smaller time intervals allowing true ZC instants to be localised.

(FPGAs), commonly adopted for their scalability and high sampling rate capabilities. Additionally, experimental data that diverges from the applied theoretical model could result in systematic errors in the best fit parameters. Parameter correlations are also a concern, especially between the fitted frequency and initial phase that both reside within the argument of the sinusoid. For these reasons, we demonstrate the application of an alternative, model independent, zero-crossing (ZC) technique. This method is extremely useful as it is not heavily influenced by other signal parameters and can detect any frequency variations that occur within a single FID signal, alleviating the bandwidth restriction set by the repetition rate of the sensor. Unfortunately, this technique usually exhibits lower precision as only a select proportion of the acquired data is used in the analysis. However, ZC algorithms can be easily implemented on FPGAs in contrast to a nonlinear fitting routine that would require considerable computational resources and a high level of programming complexity [84,85]. This is particularly useful as oversampling could be implemented to enhance the SNR [86], thereby improving the achievable sensitivity.

The first step in the algorithm is to localise each ZC instant present in the signal, ascertained from the sign of the product between two consecutive samples S_n and S_{n+1}

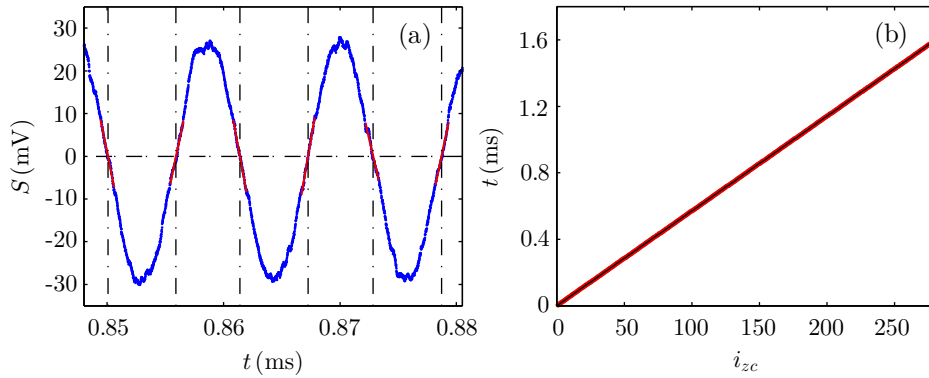


Figure 3.11: (a) Portion of a FID trace (blue) acquired at a sampling rate of $f_s = 100$ MHz, and linear fits (red) used to interpolate each ZC instant in the signal, represented by the intersections of the dot-dashed lines. (b) Time instant (red) calculated for each ZC as the signal evolves, and corresponding linear fit (black). Half the inverse of the gradient provides a measure of the Larmor frequency.

which is only negative at ZC thresholds. The presence of noise can introduce spurious counts, clearly observed at the end of the FID trace shown in Fig. 3.10(a). A low probe power was used to generate this signal to emphasise the spurious contributions that can materialise at low SNR's. These can be localised by observing the time interval between adjacent ZCs, as false counts occur at a higher frequency. This is conveyed explicitly in Fig. 3.10(b) in the form of a histogram that separates the false counts from the true ZC points. The number of semi-cycles can then be deduced from how many instants occur at large time intervals, located on the right-hand side of the histogram. False counts can be suppressed somewhat through pre-filtering of high frequency noise; however, one must be vigilant when filtering as it can significantly distort the signal. We often apply a digital bandpass Butterworth filter to the signal train post-acquisition to suppress high frequency noise, and eradicate any low frequency transients or DC offsets in the signal. The cutoff frequencies are set according to the anticipated Larmor frequency that is easily inferred by analysing the signals spectral content.

The next step requires calculating the exact instant that the signal crosses the zero-threshold, and this is calculated using linear interpolation as we are dealing with a discretised signal. The approximation that $\sin(\theta) \approx \theta$ close to the ZC is utilised, assuming that the sampling rate is adequately high with respect to the precession fre-

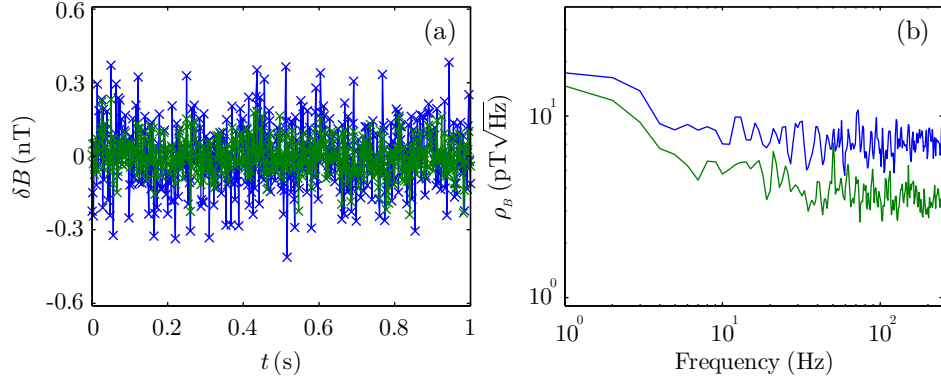


Figure 3.12: (a) Magnetic field fluctuations measured in a bias field of $25 \mu\text{T}$ from a FID signal train, acquired at the sampling rate $f_s = 2 \text{ MHz}$, using a ZC algorithm (blue) and nonlinear fitting routine (green). (b) Noise spectra generated by applying a DFT to the time domain magnetic signal. The noise floors were calculated to be $3.7 \text{ pT}/\sqrt{\text{Hz}}$ and $7.1 \text{ pT}/\sqrt{\text{Hz}}$ for data collected by the fitting routine and ZC technique, respectively.

quency to ensure its validity. As an example, performing measurements in the Earth's field (equivalent to $\omega_L/2\pi \sim 175 \text{ kHz}$ for Cs) at a sampling rate of 2 MS/s is very close to the limits of the linear approximation. Only two points per ZC instant could be used in this scenario as a consequence of the high precession rate, with the phase separation between these two discrete samples calculated to be approximately $\pi/3$. Therefore, in this instance the interpolation procedure can be performed straightforwardly using the relation,

$$t_{in} = \frac{1}{f_s} \left| \frac{S_j}{S_{j+1} - S_j} \right|, \quad (3.19)$$

where j denotes the data point immediately prior to a ZC, and t_{in} is the time between the j^{th} sample and the interpolated ZC time instant [87]. Equation (3.19) can indeed be applied to any respective FID signal, although low precession frequencies inevitably produce fewer ZC instants making for a less precise measurement. To circumvent this issue, one can apply a linear fit across a larger number of data points for each ZC, as seen in Fig. 3.11(a). The ratio of the signal length and the number of precession cycles is a measure of the sample count per cycle, and is the basis for determining the number of data points to apply in each linear fit. It is then trivial to deduce the ZC times from

the best fit parameters for each instant which should be linear with respect to the ZC number i_{zc} as seen in Fig. 3.11(b). The oscillation frequency can then be estimated from the gradient ΔT using the formula,

$$f_{zc} = \frac{1}{2\Delta T}. \quad (3.20)$$

One should be aware that the use of semi-cycles results in sensitivity to the harmonic at twice the precession frequency (see Section 3.3.3) in the time instant calculations from adjacent ZCs; however, the observed fluctuations are highly symmetric and can be averaged out. This occurs automatically in the final estimation of the frequency when calculating the gradient of the linear dependence shown in Fig. 3.11(b). Any other observable trends at lower frequencies would appear in the fit residuals, providing supplementary information regarding any frequency variations or distortions present in the signal.

The precession rate from a series of subsequent FID traces in a signal train were extracted using the ZC algorithm to assess the reliability and precision of the technique. The sensitivity performance is shown in comparison to a nonlinear fitting routine in Fig. 3.12 in both the time and frequency domains. It is clearly evident that the ZC technique is less sensitive than a nonlinear fit at equivalent sample rates. This is to be expected given the smaller proportion of data used in the analysis. On the other hand, the compatibility of ZC algorithms with high sampling FPGAs creates opportunity for sensitivity enhancement, with sampling rates above $f_s = 100$ MHz easily achievable. It is particularly noteworthy that the difference in the average bias field measured from both techniques over the 1 s time period was 12.9 pT. This is slightly greater than the average error calculated for each technique indicating that there are some systematics present, although fairly minimal in this instance. It can be seen that both methods track the pattern of low frequency drifts very well and this is reassuring considering the limitations of the applied fit model.

3.3.7 Damping rate estimation

The damping rate associated with a FID signal is an important parameter in characterising magnetometer performance in terms of both sensitivity and bandwidth (see Section 4.2). For example, we have already seen that the precision of a FID magnetometer is primarily governed by the SNR and the coherence lifetime as indicated by the CRLB condition in Eq. (3.14). As with the precession frequency, the damping rate can be estimated as a free-parameter in the DS model fit. Inaccurate predictions caused by an imperfect theoretical model and parameter correlations can be a concern, thus alternative methods can serve to verify results achieved from a nonlinear fit.

The premise of the method proposed here is shown in Fig. 3.13(a) and relies on interpolating a second order polynomial model at each peak in the damped sinusoid. Knowledge of the number of samples per cycle and the respective ZC instants (see Section 3.3.6) allows assessment of which data points to include in each polynomial fit. Each fit enables determination of the time instants, symbolised by the dashed lines in Fig. 3.13(a), and corresponding peak values. The interpolated results are then superimposed to form the signal envelopes depicted in Fig. 3.13(b). Each envelope is fit to

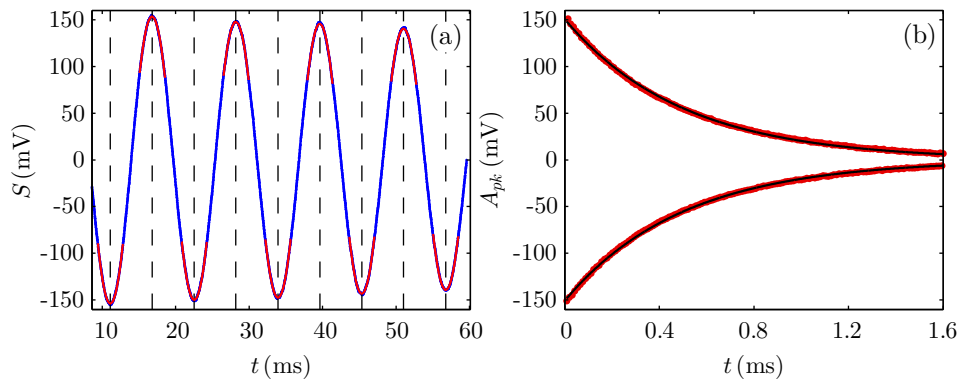


Figure 3.13: (a) Portion of a FID trace (blue) sampled at a rate of $f_s = 100$ MHz, and polynomial fits (red) used to interpolate the time instants (dashed lines) and values of each signal peak. (b) Ensuing signal envelopes (red) and associated fit to an exponential function (black). The difference in the measured decay rate for each envelope was 1 Hz.

the exponential function,

$$A_{pk}(t) = A e^{-\gamma_2 t}, \quad (3.21)$$

where A and γ_2 are the signal amplitude and relaxation rate parameters equivalent to that seen in the DS model in Eq. (3.2). A weighted average of the damping rates calculated from each envelope is performed to increase the measurement precision. Equivalently, both envelopes could be collated together by inverting the sign of one with respect to the other, and the same exponential fit function can be applied. The damping rate and associated errors were very similar using both methods thus epitomizing the symmetry of the FID trace. However, slight trends were observable in the fit residuals indicating that the damping is not completely described by the exponential function in Eq. (3.21). This is no surprise given the results of previous DS model fits that leave a residual component at the fundamental frequency as observed in Fig. 3.6(b). These residual trends could be eliminated by incorporating an additional, higher frequency, relaxation parameter of different amplitude into Eq. (3.21); however, this improvement did not extend to the DS model fit and could simply be a case of overfitting.

3.4 Detection of Spin Precession

3.4.1 Optical polarimetry

There are two main detection modes used extensively in atomic magnetometers to perform readout of the spin precession frequency. The first technique involves monitoring the light intensity exiting the vapour cell with a single photodiode in an absorptive measurement. In this configuration, circularly polarised light is optimal as it generates a higher degree of orientation in the atomic ensemble and maximises the sharp variation in the absorption coefficient experienced when reducing the laser power during readout. Numerous magnetometry configurations adopt this detection mode, particularly in miniaturised devices as only one photodiode is necessary thereby increasing simplicity and scalability of the device. The primary vulnerability of absorption based

detection is its susceptibility to intensity fluctuations that are directly imprinted into the precession signal. This drastically degrades the achievable SNR, placing a strict limit on the magnetometer's sensitivity performance. In order to circumvent this issue, a balanced polarimeter can be employed in a dispersive measurement that detects polarisation rotation in the transmitted light, induced by the component of the macroscopic magnetisation precessing transverse to the magnetic field. This modifies the birefringent properties of the sample causing the two orthogonal circular contributions of the linearly polarised component of the light beam to experience different refractive indices.

A typical polarimeter consists of a half-wave plate, a PBS oriented at approximately 45° with respect to the linearly polarised input, and two photodiodes as illustrated in Fig. 3.3. Application of the half-wave plate in the detection process enables alignment of the light polarisation to the appropriate axis of the PBS, ensuring an equal proportion of light through both channels. The intensities of the two beams separated by the transmitted and reflected ports of the PBS will follow Malus's law [1],

$$I_1 = I_0 \sin^2\left(\theta - \frac{\pi}{4}\right), \quad (3.22)$$

$$I_2 = I_0 \cos^2\left(\theta - \frac{\pi}{4}\right), \quad (3.23)$$

where $I_0 = I_1 + I_2$ is the total light intensity and θ is the polarisation angle. Subtraction of both intensity signals results in a rotation angle of,

$$\theta = \frac{I_1 - I_2}{2(I_1 + I_2)}, \quad (3.24)$$

which is valid for small rotations that adhere to the linear approximation, $\sin(\theta) \approx \theta$. There are modulated polarimetry techniques that employ a Faraday rotator and lock-in amplifier to actively suppress $1/f$ technical noise, introduced through various sources including drifts in laser frequency, intensity, or cell temperature [1]. Although effective, these techniques are only necessary when the spin polarisation is precessing slowly, as seen in devices that operate near zero-field. For the high precession rates well-suited

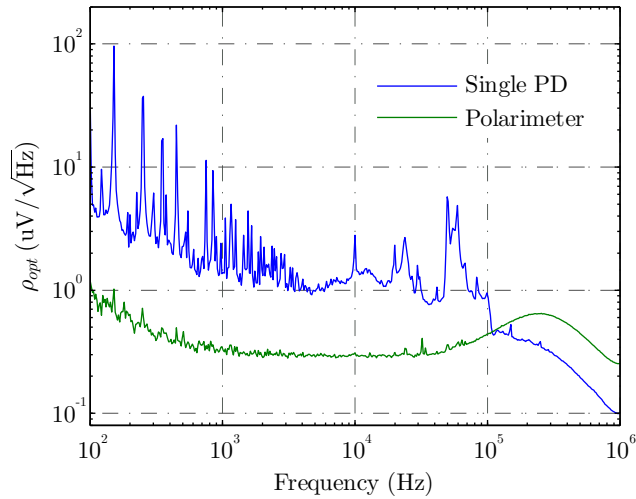


Figure 3.14: Typical optical noise spectra collected in the absence of a vapour cell using a solitary photodiode (blue) and a balanced polarimeter (green) at a laser power of $200 \mu\text{W}$. The differential measurement results in considerable noise suppression in the frequency range of interest. The increase in noise at higher frequencies is likely due to addition of uncorrelated white noise from both channels of the polarimeter.

to the FID technique, $1/f$ noise is less of a concern and can be easily suppressed with appropriate filtering.

After the light exits the vapour cell, both photodiode signals are amplified before subtraction to form the final polarimetry signal as low light levels are to be expected during the probe phase. The intensity noise measured from the polarimeter and a single photodiode at $200 \mu\text{W}$ are shown explicitly in Fig. 3.14. The impressive noise cancellation performance of the polarimeter is clear from the baseline noise level showing around a 4-fold improvement in the frequency range of interest. More importantly there is considerable suppression of numerous technical noise peaks prominent in the laser intensity signal. The elevated noise level evident at higher frequencies is a consequence of uncorrelated white noise being added in the differential measurement. This poses no problems in terms of signal analysis as a low-pass filter can be applied to condition the data post-acquisition; the nonlinear fitting routine would also help in this regard. The total RMS noise in the polarimeter was measured to be around $\sigma_\theta \simeq 71 \mu\text{rad}$; however, it is possible to reduce this noise slightly with optimal tuning of the detection bandwidth based on the precession rate by increasing the gain in the

transimpedance amplifier (TIA). The conversion of the polarimeter output to radians was inferred from an auxiliary experiment consisting of monitoring the voltage change as the polarisation angle was rotated, for a consistent probe power of $P_r \simeq 200 \mu\text{W}$ that is adopted extensively throughout this work.

3.4.2 Absorptive vs. dispersive measurements

Both absorptive and dispersive measurements were performed to demonstrate the crucial impact that balanced polarimetry has on improving the sensitivity of the FID implementation. An example signal that was acquired using absorption based detection with circularly polarised light is depicted in Fig. 3.15(a), showing the full extent

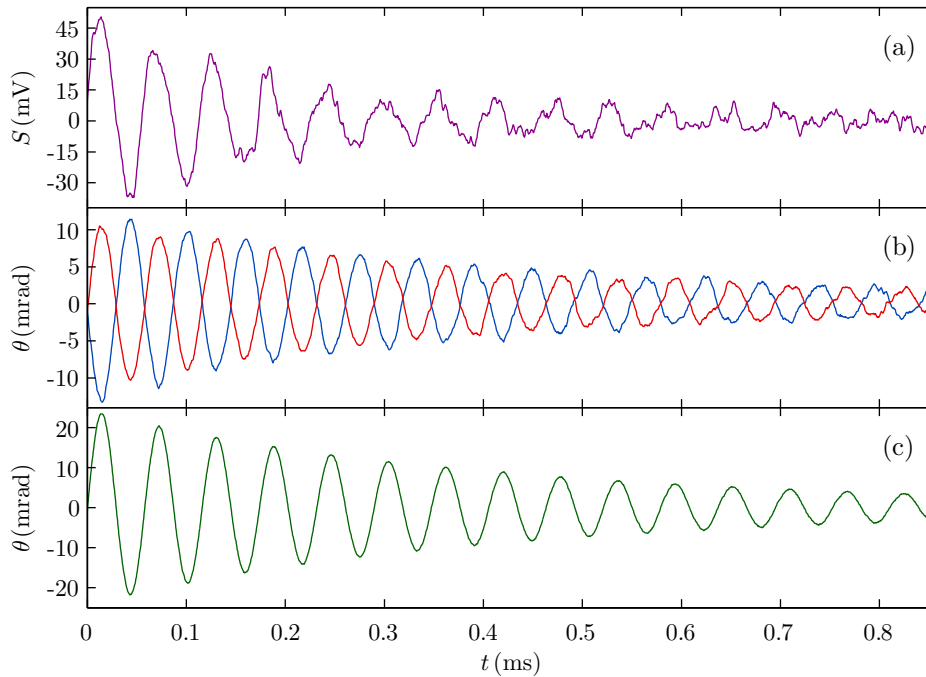


Figure 3.15: Example FID traces collected using different detection modes including (a) an absorptive measurement from a single photodiode (purple) using a circularly polarised probe, (b) optical rotation measured from the transmitted (blue) and reflected (red) ports of a PBS using an elliptically polarised probe, and (c) the difference signal (green). Approximately an 8-fold SNR enhancement was gained using differential detection in comparison to monitoring one port of a PBS. Adding the signals in (b) also results in an absorptive measurement but with a reduced SNR in comparison to the absorption signal in (a) due to the light polarisation used in each case.

of intensity noise leaking into the precession signal. Laser intensity fluctuations are inevitably converted into polarisation noise in the rotation signal, evidenced by noise present in the FID traces depicted in Fig. 3.15(b) which are the projections of the y and z components of the output lights polarisation. The SNR is far superior in the rotation signals as the dispersive measurement generates higher signal amplitude [44]. Optical rotation in the y - z plane causes a variation in the projection of one of these components at the expense of the other, resulting in the phase difference observed between the two signals. Since a single beam is employed for both the pumping and probing processes, elliptically polarised light provides an adequate balance for this detection mode; the circular component is used to prepare the atomic spins and the linear component enables detection of the evolving magnetisation through optical rotation. The degree of ellipticity in the input light will affect the efficiency of the optical pumping and detection processes and it was found that approximately an equal superposition of circular and linear polarisation was optimal [88]. One could achieve higher sensitivity by performing optical pumping and detection with independent light beams [25]. This will add an extra degree of complexity to the system which may be undesir-

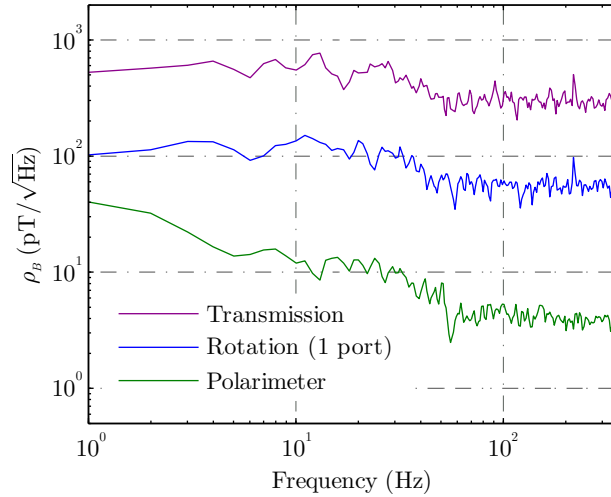


Figure 3.16: Typical magnetic field sensitivity spectra collected using different detection modes including: absorption (purple), rotation from a single PBS port (blue), and a balanced polarimeter (green). The noise floors were calculated to be $300 \text{ pT}/\sqrt{\text{Hz}}$, $56 \text{ pT}/\sqrt{\text{Hz}}$, and $4.1 \text{ pT}/\sqrt{\text{Hz}}$.

able. It can be noticed that the amplitudes of both rotation signals are not exactly equal, attributable to the elliptical polarisation of the input light coupled with the time-dependent anisotropy of the sample. If adequately balanced, a polarimeter is far more sensitive than absorption-based detection as the differential measurement results in large suppression of common-mode noise. This is clearly portrayed in Fig. 3.15(c), which shows a large degree of noise cancellation and an increase in signal amplitude when the individual outputs of the PBS are subtracted. It is also important to note that the sum of these two signals would result in an absorption measurement.

The sensitivity spectra shown in Fig. 3.16 were collected using each of the detection techniques previously discussed. In each case, the signal train was processed using the LM fitting algorithm to extract the magnetic field information from each FID trace; this was then converted into noise spectra using a DFT. The significant sensitivity improvement when detecting polarisation rotation from a single port is particularly noteworthy as only one extra linear polariser is needed. Furthermore, differential detection provides another 14-fold enhancement in magnetometer precision; however, an additional three optical components is required to implement this detection mode, thus reducing the scalability of the device and increasing the cost of fabrication.

3.4.3 Light shift systematics

One of the primary advantages in employing FID is its inherent accuracy as the spin precession is readout directly, in contrast to many devices that rely on feedback electronics [32]. Nonetheless, most magnetometry techniques, including the FID implementation, are subject to systematic shifts that occur as a consequence of the light-atom interaction during readout. This is known as the AC Stark effect, or vector light shift, and is analogous to the action of an external magnetic field in the sense that it splits the atomic energy levels. It is possible to suppress this effect; for example, one can extrapolate to the initial portion of a FID trace in a phase sensitive measurement (see Section 5.1). Another commonly adopted procedure is to detune the laser to a zero-light-shift frequency, such as a resonance peak, that typically requires actively locking on to the absorption line [89]. Here we investigate the vector light shift by measuring

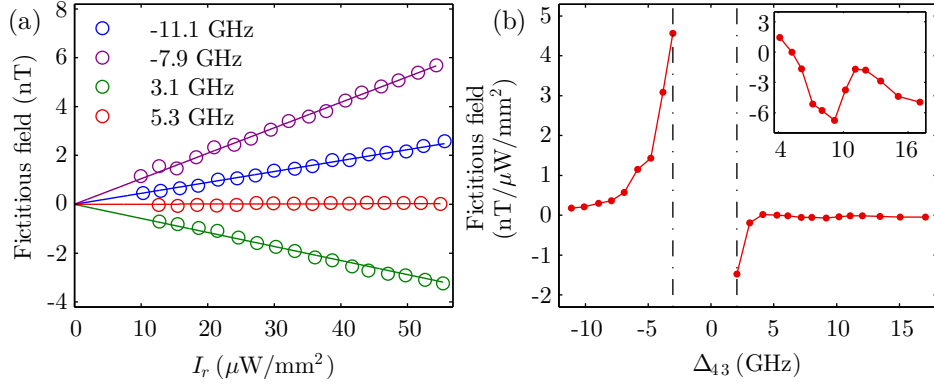


Figure 3.17: Fictitious magnetic field as a function of light intensity and detuning during readout. (a) Linear dependencies (circles) and corresponding fits (solid line) at different laser frequencies, as noted in the legend. (b) Straight line gradients (red dots) measured at detunings ranging over the D_1 line. No data was taken within the frequency range between the dot-dashed lines due to poor SNR. Inset shows a small dispersive feature that occurs close to the $F = 3 \rightarrow F'$ transition; the y -axis has been multiplied by a factor of 100.

the fictitious magnetic field experienced by the Cs atoms for varying readout powers and frequency detunings whilst employing dispersive polarimetry detection. A slight modification was made to the experimental set-up described in Fig. 3.3 to enable modulation of the light polarisation (see Fig. 5.1 for further details). This ensured circular and linear polarisations during the pump and probe stages, respectively. The linearity of the polarisation during the probe phase was verified using a PBS. The laser frequency was measured using a wavelength meter (Bristol) that has a frequency resolution of around 75 MHz. The blue shift of 80 MHz for the first-order deflection of the AOM is relatively small compared the optical linewidth of the collisionally broadened MEMS vapour cell, measured to be $\Gamma_{N_2} \simeq 3.2$ GHz. However, the shift induced by the buffer gas is not negligible and was estimated to be $\Delta_{N_2} \simeq -1.5$ GHz. Therefore, the absorption lines of the two-peak optical spectrum reside at detunings of approximately -1.1 GHz and 8.7 GHz with respect to the $F = 4 \rightarrow F' = 3$ transition of an auxiliary Cs reference cell.

Figure 3.17(a) shows the fictitious field generated as a function the probing intensity for four different laser detunings. It can be clearly seen that the fictitious field dependence is linear, and this remains valid at sufficiently low interaction strengths. The

slope is highly dependent on detuning and switches sign suggesting that zero-light-shift frequencies do exist. It can be seen that almost complete suppression of the AC Stark effect is achieved at a detuning residing at the turning point between the two resolvable transitions, as depicted by the red data set in Fig. 3.17(a). The gradient of the fictitious field dependence as a function of the detuning is shown explicitly in Fig. 3.17(b). The $F = 4 \rightarrow F'$ transition of the broadened optical spectrum lies in the frequency range separated by the dashed lines. No data was taken in this region due to the poor SNR achieved, as well as the highly nonlinear fictitious field dependencies that were observed. Nevertheless, distinctively dispersive features at either side of the dashed lines are clearly evident indicating that a zero-light-shift point does exist close to this absorption peak. Unfortunately, this is not a desirable frequency to use for achieving high sensitivities when implementing optical rotation. The nature of the observed dispersive trends will depend highly on the optical spectrum and light polarisation assuming a narrow linewidth light source such as a laser [90]. Therefore, it is no surprise that a smaller dispersive feature appears close to the $F = 3 \rightarrow F'$ transition as seen in the inset of Fig. 3.17(b). Based on these trends, it is fair to surmise that there is simultaneous interaction of multiple hyperfine transitions that contribute to the effective shift as a consequence of the broadened optical spectrum. MEMS cells containing higher buffer gas pressures, with an optical spectrum comprising of a single broadened resonance, will have a single zero-light-shift frequency at the center of the absorption peak [44]. Sufficiently detuning the laser frequency away from the $F = 3 \rightarrow F'$ resonance yields a considerably reduced effective light shift that can even be completely eliminated at a detuning of approximately 5.3 GHz for this MEMS vapour cell. It should be noted that the sensitivity performance of the magnetometer at this laser frequency is very competitive, degrading by less than a factor of two compared to the optimised frequency under the same experimental conditions.

3.5 Optical Pumping

3.5.1 Modulation techniques

It is well known that the efficiency of the optical pumping process can be improved by synchronously driving the atoms at the Larmor frequency or one of its subharmonics [34]. One can apply this driving field through various mechanisms including modulating the amplitude, frequency or polarisation of the light source, or alternatively using double-resonance techniques implementing external RF fields. In fact, there are magnetometry configurations that apply dual modulation to significantly improve both the accuracy and precision of the device [91, 92]. Although the FID technique does not require a concurrent driving field in its operation, it significantly enhances system performance and allows for a more robust sensor. One of the crucial benefits of synchronous modulation is the substantial improvement in dynamic range, with measurements above that of the Earth's field ($\sim 50 \mu\text{T}$) now easily achievable, which is essential for unshielded applications. The superior performance when implementing a concurrent drive is illustrated in Fig. 3.18 in the form of several FID traces that were generated in different bias fields using both single-pulse and synchronous optical pumping. The arbitrary waveform generator used as the voltage source for the AOM enabled both pumping techniques to be implemented in consecutive pump-probe cycles. This ensured consistency in the system parameters being applied and allowed a detailed investigation of the two optical pumping techniques. The repetition rate f_d was set low enough for the spin polarisation to fully equilibrate in attempt to avoid memory effects. It was discovered that square-wave modulation provides a larger SNR in the AM implementation as a consequence of the increased time spent at peak pump power. Concurrent drives tend to require prior knowledge of the external field; however, this is easily attainable in a FID setting by scanning the modulation frequency and maximising the signal amplitude in the time domain. Alternatively, one can utilise single-pulse optical pumping as an initial estimation of the Larmor frequency; this can then be inserted as the modulation input in a two-step feedback process. Single-pulse optical pumping was found to be more efficient at low magnetic fields where the Lar-

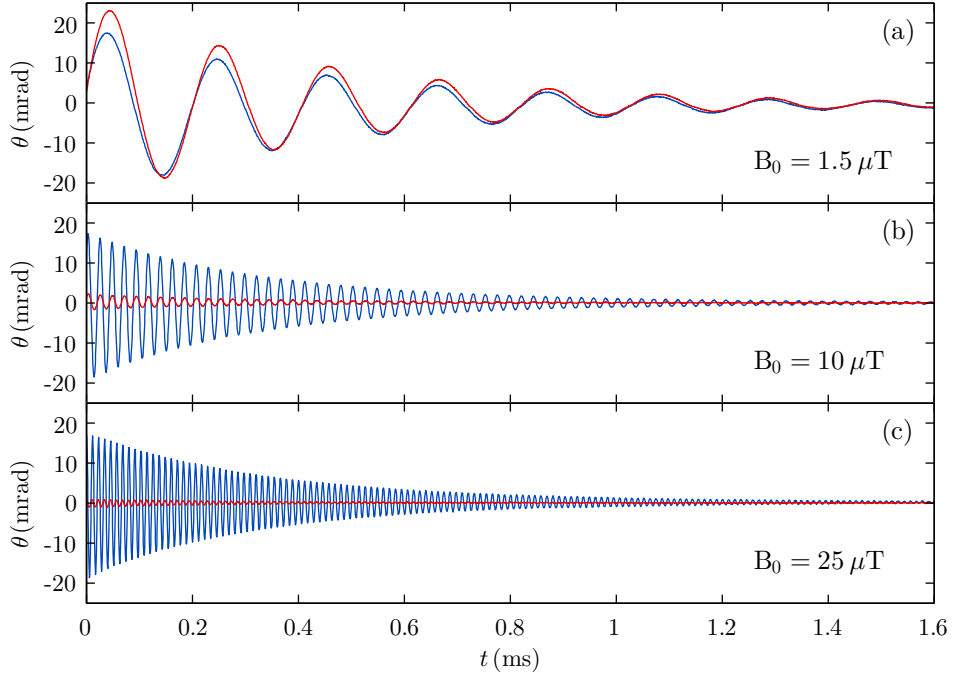


Figure 3.18: Optical rotation signal (raw data) observed using single-pulse (red) and synchronous (blue) optical pumping for bias fields of (a) $1.5 \mu\text{T}$, (b) $10 \mu\text{T}$, and (c) $25 \mu\text{T}$. The total measurement period was set to $T = 2 \text{ ms}$ showing the full decay of the atomic spin polarisation to equilibrium. The reduction in signal amplitude is clearly evident when applying single-pulse optical pumping at high bias fields.

more frequency was on the order of the relaxation rate. This is simply a consequence of the pump time T_p restricting the number of oscillations available in the synchronous regime at low frequencies. Optical pumping using a single pulse becomes increasingly inefficient at stronger bias fields, prompting a reduction in signal amplitude. These observations are consistent with the analytical solutions to the Bloch equations provided in [32], by Grujić *et. al.* Transverse magnetic fields depolarise the atomic spins; therefore, synchronously driving the precession is essential in maintaining a consistent degree of phase coherence at large bias fields and extending the dynamic range. This can be readily seen in Fig. 3.18 where the signal amplitude remains constant at higher Larmor frequencies.

Further evidence emphasising the importance of a resonant driving field is exhibited in Fig. 3.19 which illustrates the effects of varying the pump duration T_p when employing single-pulse optical pumping in a static field of $B_0 = 5 \mu\text{T}$. The pump time

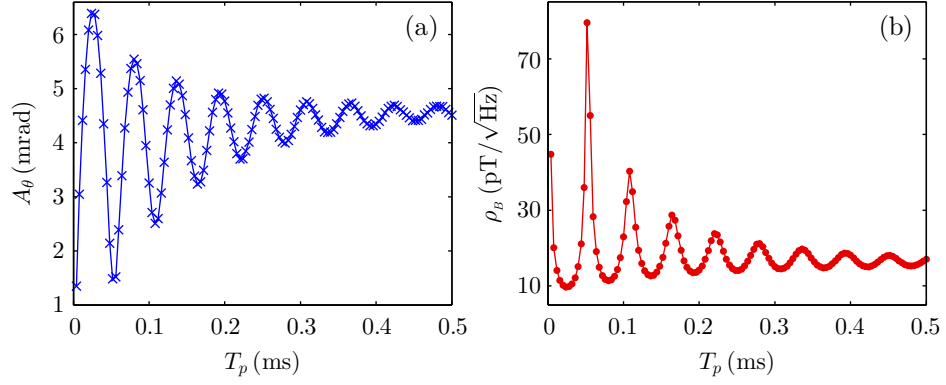


Figure 3.19: Dependence of (a) the FID signal amplitude (blue) and (b) the predicted sensitivity (red) on the pump duration when applying AM with a single-pulse at a peak pump intensity of $I_p \simeq 2.4 \text{ mW/mm}^2$, in the presence of a $5 \mu\text{T}$ static field. Data has been interpolated to supplement visualisation. The oscillatory behaviour arises as a consequence of the external bias field affecting the optical pumping efficiency for this implementation due to limitations in the optical power available.

was incrementally increased in steps of $4 \mu\text{s}$ up to a maximum of $T_p = 0.5 \text{ ms}$, and the driving frequency was set to $f_d = 250 \text{ Hz}$ to ensure that each signal fully equilibrated prior to the next pump pulse. The LM fitting routine was applied sequentially to each FID trace in the signal train which was collected for an total acquisition period of 5 s resulting in 10 repetitions for each pump time⁴. A weighted average was then applied to the best fit parameters that were gained using identical operating conditions. The dependence of the signal amplitude on pump duration is depicted in Fig. 3.19, as well as the noise density ρ_B calculated using the CRLB condition as mentioned in Section 3.3.5. It is immediately observable that there has been a reduction in signal amplitude as a consequence of the magnetic field dependence discussed previously. One would perhaps expect a steady increase in spin polarisation, proportional to the FID amplitude, until reaching saturation as the pump duration is extended; however, this is clearly not the case as the signal amplitude exhibits oscillatory behaviour. This would not occur in the limit of infinite pumping power as the spin orientation reaches saturation asymptotically in the direction of the pumping field [32]. The end result is distinct peaks in sensitivity as seen in Fig. 3.19(b) with large degradation experienced at pump

⁴This is the largest time series that could be acquired on the oscilloscope at a sample rate of 2 MHz, limited by the buffer size.

durations that are close to a multiple of the Larmor period. The dominant frequency component in each data set is also close to the Larmor rate, demonstrating the premise of employing synchronous optical pumping. The benefits of resonantly driving the system is undeniable especially given the more consistent optical pumping efficiency and relative signal enhancement, which significantly improves numerous aspects of the magnetometer’s performance.

3.5.2 Optimisation of pumping parameters

We focus on optimising the three primary parameters that influence the optical pumping efficiency in the resonantly driven system: the optical pumping power P_p , pump duration T_p , and duty cycle η of the applied square-wave modulation. There is a trade-off between the light intensity and number of interacting atoms dependent on the beam waist that effects the optimum sensitivity. Also, larger beam areas increase the susceptibility of light being blocked by azide residual in the vapour cell; hence, a beam area of approximately 2.5 mm^2 was determined empirically to yield the best results⁵. The CRLB sensitivity is an extremely useful performance indicator, correlating closely with the maximum signal amplitude as one would expect. In each experiment, an arbitrary waveform was produced serving as the voltage input to the AOM as a way of varying the parameter of interest incrementally over a predetermined range. As performed previously, the FID data was collected on the oscilloscope for 5 s and processed post-acquisition using the LM fitting algorithm to extract the relevant free-parameters, with repeating cycles of the arbitrary waveform used to form an average. The cell temperature, light polarisation, probe power, and laser frequency form a large parameter space that all impact the highest SNR that can be achieved. As discussed in Section 3.2, the optimal laser frequency typically resides close to the $F = 3 \rightarrow F'$ transition for the collisionally broadened vapour cells considered here. At this frequency detuning, a probe power of $P_r \simeq 200 \mu\text{W}$ is high enough to achieve a good SNR whilst minimising the effects of power broadening. The vapour cell temperature was optimised based on

⁵A total of 30% of light is typically lost due to Fresnel reflection and azide residual blocking the beam path under these conditions.

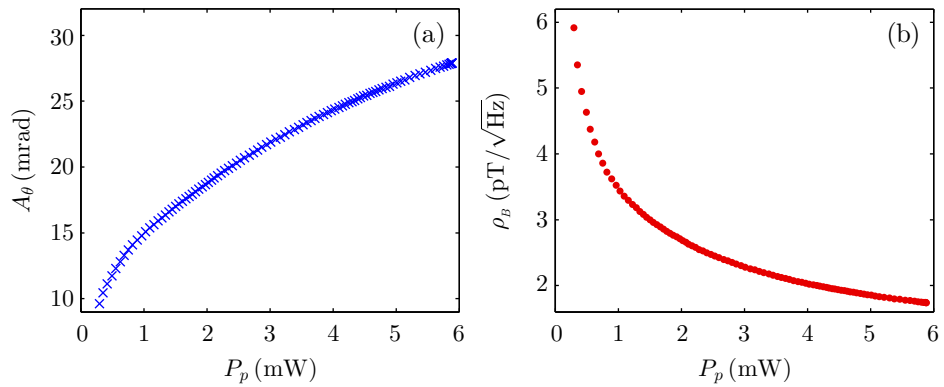


Figure 3.20: Dependence of (a) the FID signal amplitude (blue) and (b) the predicted sensitivity (red) on the optical pumping power using AM in the synchronous regime. The peak pumping power available after losses was $P_p \simeq 6$ mW which is below the optimum for this system. The beam area was kept consistent with previous experiments at approximately 2.5 mm^2 .

these chosen parameters in an auxiliary experiment and was found to reside around 85°C . As mentioned in Section 3.4.2, the optimal light polarisation is elliptical in account of the single-beam geometry.

The FID mechanism relies heavily on generating a large degree of spin polarisation in order for the atomic ensemble to evolve coherently during the detection phase; therefore, the initial signal amplitude A_θ after optical pumping provides excellent means of optimising the system. For example, it is clearly evident in Fig. 3.20(a) that further enhancement in the signal amplitude could be attained if higher optical power was available, thereby demonstrating that the sensitivity is slightly limited by the laser power. Magnetometers that employ a single-beam geometry are typically subject to significant power broadening and light shifts from strong optical pumping that degrades both the sensitivity and accuracy of the device. Advantageously, the FID technique has reduced sensitivity to these substantial systematic effects as the pumping pulses do not effect signal detection⁶. The second experimental parameter affecting the optical pumping efficiency is the duty cycle applied when resonantly switching the intensity during the pump stage. It can be readily seen in Fig. 3.21 that the duty cycle of the applied square waveform is optimal close to $\eta \sim 35\%$, which is consistent with the

⁶Light is necessary for detection; however, systematics are considerably reduced in comparison to techniques that pump and probe simultaneously at higher light power.

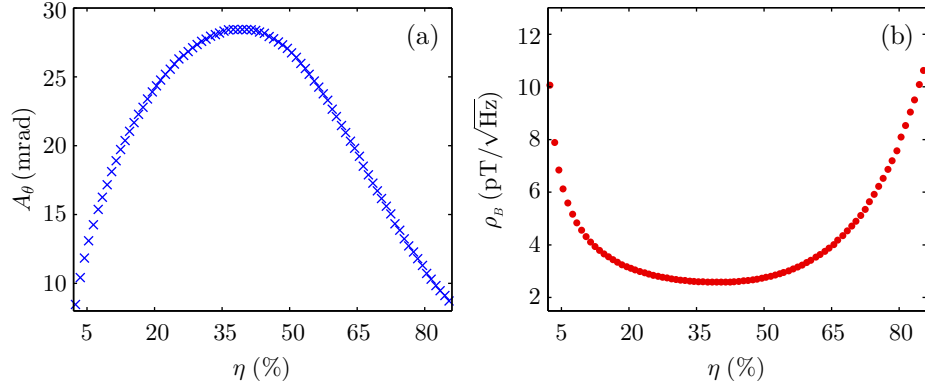


Figure 3.21: (a) FID signal amplitude (blue) and (b) the predicted sensitivity (red) as a function of duty cycle whilst employing synchronous optical pumping in the AM configuration. It can be seen that the optical pumping efficiency is optimised when the pulse intensity is high approximately $\eta \sim 35\%$ of the total pump time.

observations of Grujić *et. al.* in [32]. In light of this, we exclusively adopt this duty cycle in all the experiments utilising synchronous optical pumping with AM to obtain maximal sensitivity.

Perhaps the most crucial parameter in the optimisation of the FID magnetometer is the pumping time T_p as it effects both the sensitivity and bandwidth of the device. For example, one must allocate sufficient pumping time to generate the required spin polarisation before detection thereby restricting the bandwidth of the measurement. Also, if the sample is not optically pumped for an adequate duration then less coherence will be generated resulting reduced sensitivity. In Fig. 3.22(a), we demonstrate the build up of spin polarisation during optical pumping as the number of pulses in the synchronous regime is incrementally increased. The data processed from the signal train were fitted to the model,

$$A_\theta = a_0 (1 - e^{-R_p T_p}), \quad (3.25)$$

to determine the optical pumping rate, calculated to be $R_p = 8.2 \text{ kHz}$ [32]. The total spin polarisation of the atomic sample can then be estimated as $P \approx 0.77$ using rate equations for a simple spin-1/2 system (see Section 3.5). This takes into account the rapid collisional mixing of atoms in the excited state arising due to the presence of

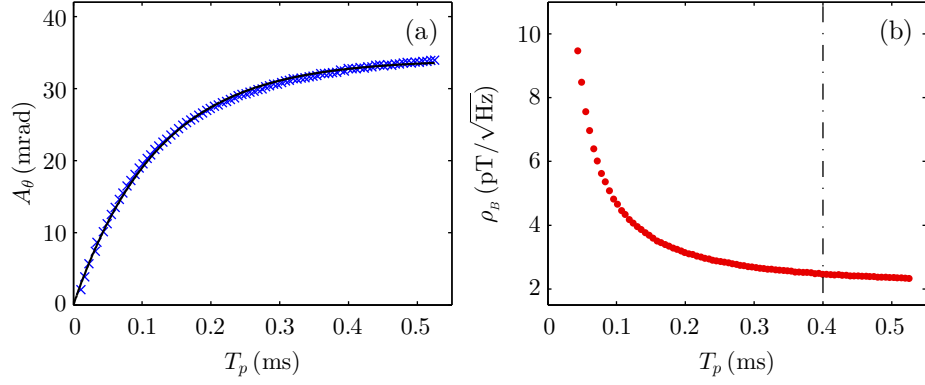


Figure 3.22: Dependence of the (a) FID amplitude (blue crosses) and (b) CRLB estimated noise density (red dots) as a function of pump duration in the synchronous regime. The black line in (a) is the associated fit to an exponential model. The number of cycles during the pump stage was swept from 1 to 100 at a driving frequency of $f_d = 200$ Hz. The dot-dashed line in (b) indicates the approximated relaxation period measured from the fitted damping parameter.

N_2 . Saturation of the spin polarisation is clearly evident at $A_\theta \simeq 33$ mrad resulting in an optimum noise density of $\rho_B \simeq 2 \text{ pT}/\sqrt{\text{Hz}}$. It can be readily seen that there is little improvement in sensitivity when the pump duration surpasses a single relaxation period as the sample has become sufficiently polarised. For this reason, we commonly adopt a pumping time of $T_p \simeq 1/\gamma_2$ in our experiments. Given the optimum probe time is approximately $T_r \simeq 2/\gamma_2$ as mentioned in Section 3.3.5, it is reasonable to conclude that the ideal driving frequency would be $f_d \simeq \gamma_2/3$ when implementing a nonlinear fitting routine in the signal analysis. In this instance the sensor repetition rate should be set to $f_d \simeq 800$ Hz based on the measured spin relaxation rate.

3.5.3 Potential systematics based on operating conditions

We have seen in detail that the precision of the FID sensor is highly dependent on the level of spin coherence generated in the atomic ensemble. Many of our experiments are performed in a bias field close to that of the Earth's ($\sim 50 \mu\text{T}$), and this has some interesting implications when considering the accuracy of the magnetometer readout. Figure 3.23 explicitly conveys the consequences that altering the optical pumping conditions has on the estimated precession rate. The most notable observation is that the

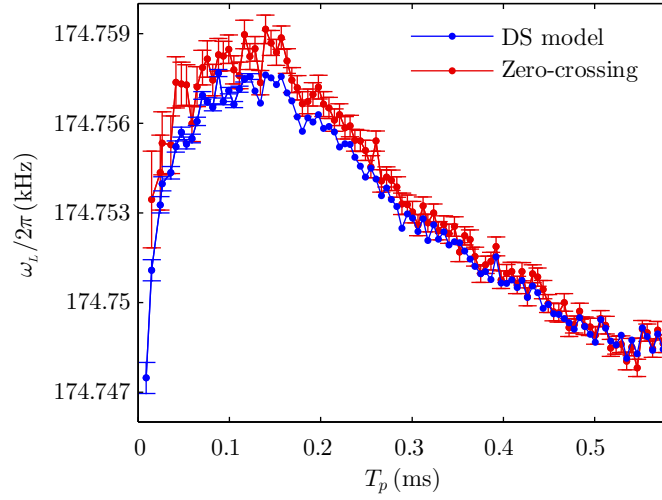


Figure 3.23: Larmor frequency measured by an amplitude modulated FID magnetometer that is resonantly pumped for different durations using two alternative frequency extraction techniques including: a fit to a DS model (blue), and a method based on ZCs (red).

measured Larmor frequency demonstrates a clear downward trend that extends over a range of approximately 8 Hz. As mentioned in Section 2.3.2, the heading error experienced by scalar magnetometers based on Cs will be on the order of the quantum beat revival frequency ($\omega_{rev} \simeq 3.3$ Hz at $50 \mu\text{T}$) which describes the contribution of the quadratic term toward the precession frequency. For example, systematic errors ranging between 1-10 nT are fairly common [2]. This undesirable feature typically arises due to a change in pumping direction altering the distribution of the ground state population, thus shifting the central frequency of the magnetic resonance by a factor on the order of ω_{rev} . Even though the orientation of the sensor remained constant in this particular case, the same logic is still applicable as the dissimilarity in the distribution of atomic polarisation for different pumping times will distort the magnetic resonance in a similar manner.

Elliptically polarised light is utilised as a compromise for efficient optical pumping and detection as a result of using a single-beam geometry and, consequently, will create a highly anisotropic distribution of atomic population among the Zeeman sublevels [76]. The value of the experienced shift due to nonlinear Zeeman splitting is contingent on

the spin polarisation induced after optical pumping and this will differ depending on the utilised system parameters. The multipole moments generated in the atomic ensemble by the elliptically polarised beam will introduce multiple harmonics to FID spectrum, the amplitude of which will change under different operating conditions. Therefore, we can not exclude the possibility that the observed systematics are a result of the frequency extraction technique itself as both the nonlinear fit and ZC frequencies may be sensitive to these higher order terms. This is completely feasible given the slight differences in Larmor frequency measured by both techniques, especially for smaller pump durations that yield lower SNR.

3.6 Frequency-Modulation Scheme

3.6.1 Experimental set-up

Aside from the microfabricated vapour cell, the AM configuration contains numerous components that are incompatible with a miniaturised design. The primary motivation for conversion to a FM implementation was to minimise the number of components necessary to characterise and operate the magnetometer whilst maintaining a high level of performance and chip-scale compatibility. The FM system was developed using components that could be easily integrated into a packaged device. The key alteration is the application of a VCSEL (Vixar) as the solitary laser source, which is housed in a TO46 can. However, these devices can be utilised in a compact die format comprising a $250\ \mu\text{m}$ square with a thickness of $150\ \mu\text{m}$. Their single mode output has a sufficiently narrow spectral linewidth as to resolve the D_1 line hyperfine structure. The VCSEL is placed inside an adjustable collimation mount with an aspheric lens to condition the divergent beam; although this is not essential in a compact system, it will improve performance especially when implementing a polarimeter as any light leakage is minimised and the same beam width falls on both photodiodes. The beam size also becomes particularly important when attempting to balance between efficient optical pumping and maintaining a large interaction volume, especially in situations where the optical power is limited as is the case here. It can be seen in Fig. 3.24(a) that the optical

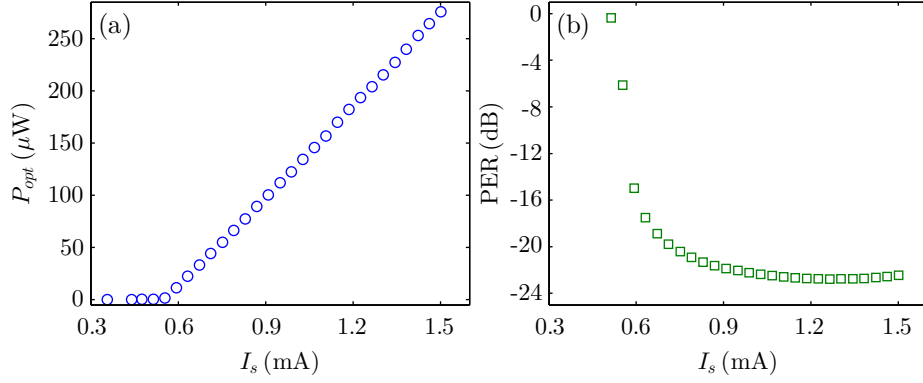


Figure 3.24: VCSEL (Vixar) characterisation showing the (a) optical power, and (b) polarisation extinction ratio as a function of supply current.

power emitted by the VCSEL demonstrates a linear dependence with supply current with an approximate gradient of $292 \mu\text{W}/\text{mA}$ and a threshold current of 0.56 mA . The polarisation extinction ratio, shown in Fig. 3.24(b), remains fairly stable across the measured operational range of supply currents suggesting that polarisation switching has not occurred, although this behaviour could be introduced at sufficiently high injection currents. The wavelength varies approximately linearly with supply current across the optical transition of interest with a slope of $0.23 \text{ nm}/\text{mA}$.

The temperature and injection current are the two adjustable parameters that modify the output wavelength of the VCSEL. The temperature is typically set to 80°C to localise the D_1 transition at an injection current of 2 mA ; the quoted temperature stability of $0.06 \text{ nm}/^\circ\text{C}$ was in good agreement with experimental measurements. Heating of the laser module is performed by a Peltier thermoelectric cooler in conjunction with the Thorlabs TED200C proportional-integral-derivative (PID) temperature controller. A temperature sensor is placed in close proximity to the collimation mount allowing measurement of the VCSEL temperature. The bulk of material used in the heating process increases the thermal time constant enabling an extremely stable temperature, which would not be the case in a chip-scale device. In this case, a more stringent PID control would be required or potentially part of the measurement process dedicated to locking onto the absorption line. The whole laser assembly is contained within an aluminium enclosure to restrict ambient temperature fluctuations and reduce electro-

magnetic interference. The Thorlabs VLDC002 VCSEL driver is utilised as a current source allowing external voltage control of the output current as well as providing damage protection including a current limit. An arbitrary function generator acts as the voltage source enabling synchronous or single-pulse optical pumping such as that used in the AM scheme. The maximum injection current for single-mode operation was implemented to improve the optical pumping efficiency.

3.6.2 Pump frequency optimisation

Here we focus on optimising the optical pumping efficiency using the FM implementation by varying the frequency detuning utilised during the pump stage. The spin ensemble is pumped synchronously at the modulation frequency $\omega_m/2\pi = 17.5$ kHz that aims to actively drive the atomic precession. An arbitrary waveform similar to that illustrated in Fig. 3.2(b) was created as a means of sinusoidally modulating the VCSEL injection current when pumping whilst maintaining a constant probe for detection. The pump frequency ν_p was varied incrementally over the full D₁ line and the frequency during readout was kept fixed at $\nu_r \simeq 22.7$ GHz with respect to the $F = 4 \rightarrow F' = 3$ transition. The laser frequency was calibrated using an auxiliary Cs reference cell, and the light power during the probe was approximately 200 μ W. AM attributed to changes in the supply current can be considered as negligible in comparison to the FM effects. The optimal pump frequency is highly dependent on the spectral properties of buffer gas MEMS cell, in this case consisting of two slightly overlapping absorption peaks (see Fig. 5.11(f)) with an estimated broadening and shift of $\Gamma_{N_2} = 3.2$ GHz and $\Delta_{N_2} = -1.5$ GHz, respectively. We performed the measurements at two different resonant bias fields such that the precession rates coincided with the fundamental and second harmonic of the modulation frequency. It can be seen from Fig. 3.25 that the observed behaviour is very different in each case. For example, there are peaks in signal amplitude as the central frequency of the sinusoidal modulation passes through the $F = 3 \rightarrow F'$ transition. The slight fluctuation in SNR observed at adjacent pump frequencies occurs as multiple hyperfine transitions are being excited simultaneously due to the merged optical resonance structure. The signal amplitude

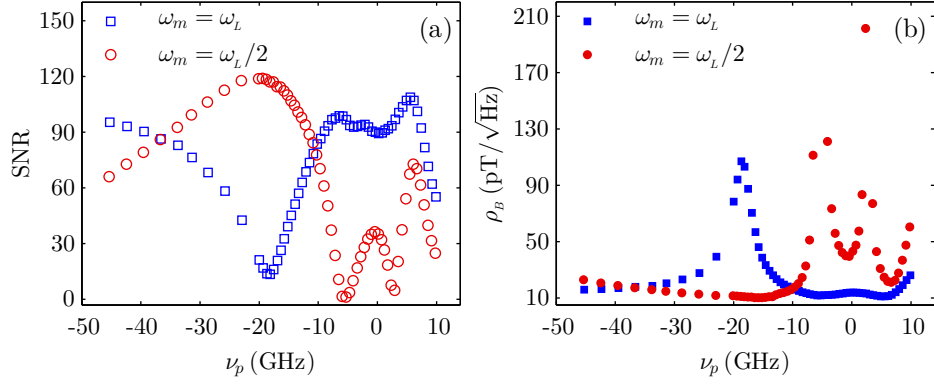


Figure 3.25: Parameter optimisation for the FM implementation with the (a) SNR and (b) CRLB sensitivity shown as a function of pump frequency detuning in the presence of a $5 \mu\text{T}$ (blue) and $10 \mu\text{T}$ (red) magnetic field. The broadening and shift of the implemented vapour cell were calculated to be 3.2 GHz and -1.5 GHz , respectively. The probe frequency was kept constant at 22.7 GHz with respect the $F = 4 \rightarrow F' = 3$ transition.

then reaches a minimum as the central pump frequency becomes resonant with the stronger $F = 4 \rightarrow F'$ transition. This reduction in signal is attributed to the atoms being resonant twice per Larmor period, thus depolarising the spins after each half cycle. This is in contrast to the case that $\omega_m = \omega_L/2$ which demonstrates the best SNR when the central frequency is tuned closely to $F = 4 \rightarrow F'$ absorption peak as the atoms are now only resonant once per Larmor period. The optimum sensitivity reached at each bias field is very similar as seen in Fig. 3.25, and this introduces some technical benefits. For example, components in chip-scale magnetometers are closely packed hence the currents driving the VCSEL will be very close to the sensor head. The ensuing spurious magnetic fields will be resonant with the precession resulting in an enhanced atomic interaction that interferes with the measurement. Therefore, it is preferable to modulate at a frequency not equivalent to the Larmor precession rate for compact devices.

3.7 Sensitivity Analysis: AM vs. FM

The AM scheme provides an ideal benchmark to assess the optimum sensitivity achievable using FID. Although there is potential for further optimisation, it is unlikely to

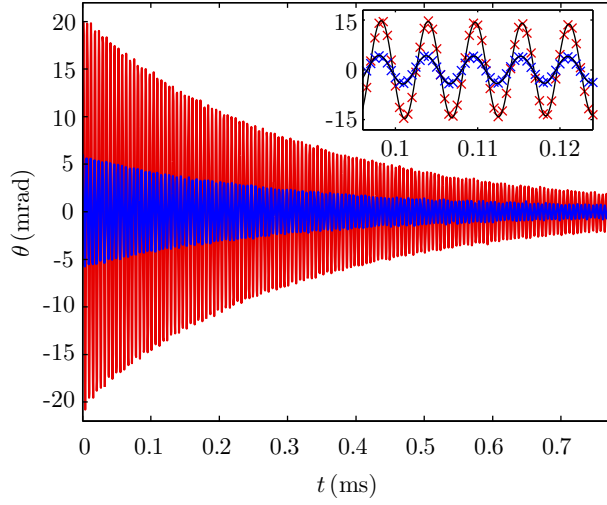


Figure 3.26: Typical FID data collected using the AM (red) and FM (blue) configurations in a $50 \mu\text{T}$ magnetic field. The inset shows approximately $30 \mu\text{s}$ of data to enhance visualisation of the fit with respect to the raw data.

yield significant improvements in the overall sensitivity. Therefore, the primary motivation of this section is to demonstrate the performance of FM with respect to the AM technique, which is of particular interest considering the increased scalability of a device based on FM. Experimental parameters such as the pump duration, repetition rate, input polarisation, and beam width were kept consistent to ensure a valid comparison between both techniques. Figure 3.26 shows two different FID traces collected using the AM and FM configurations in a magnetic field of $|\vec{B}| \simeq 50 \mu\text{T}$, transverse to the beam propagation direction. The precession frequency is relatively high at $\omega_L/2\pi \simeq 175 \text{ kHz}$; therefore, the inset in Fig. 3.26 has been included to improve visibility of the raw traces and corresponding nonlinear fit. Any DC offsets in the raw signals are a consequence of imperfect balancing of the polarimeter, and this can be added to the fit model as an extra parameter. Alternatively, since we are only interested in the part of the signal oscillating at ω_L , a bandpass Butterworth filter can be applied in the software to smooth the previously recorded data as well as eradicate any DC offsets or slowly varying terms. As performed previously, the raw data was processed post-acquisition by fitting the data to the model given in Eq. (3.2). The relevant experimental parameters were extracted including: signal amplitude A_θ (proportional to the initial magnetisa-

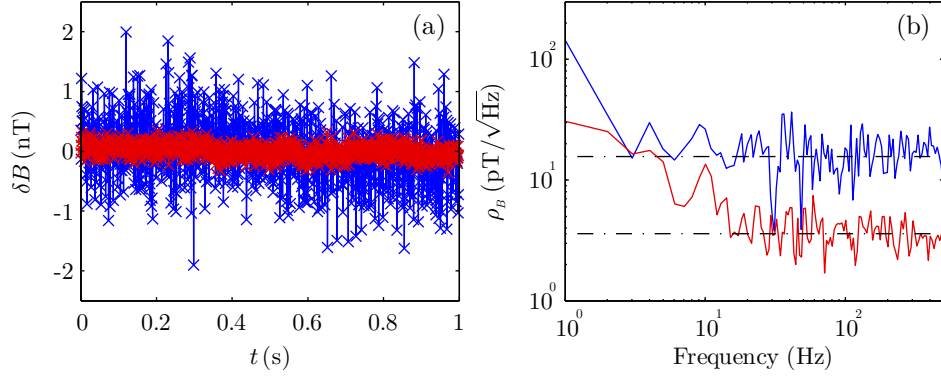


Figure 3.27: (a) Magnetic field fluctuations recorded over a period of 1 s using the FID technique with AM (red) and FM (blue). The DC component of approximately $50 \mu\text{T}$ has been subtracted from the data. The total RMS errors were measured to be 115 pT and 534 pT using AM and FM, respectively. (b) Noise spectrum of the time domain magnetic field data. The dot-dashed lines indicate the noise floors calculated to be $3.4 \text{ pT}/\sqrt{\text{Hz}}$ for the AM scheme and $15.6 \text{ pT}/\sqrt{\text{Hz}}$ using FM, with a Nyquist limited bandwidth of 500 Hz .

tion M_0), angular Larmor frequency ω_L , damping rate γ_2 , and initial phase ϕ_0 , which are all important in our analysis of the sensitivity of the device. The RMS errors in the FID data were calculated to be $\sigma_\theta \simeq 76 \mu\text{rad}$ and $\sigma_\theta \simeq 65.1 \mu\text{rad}$ for the AM and FM techniques, respectively. The reduction in noise is simply due to the larger TIA gain used in the polarimeter for the FM technique to increase the SNR.

The FID signal trains for each configuration were recorded over a period of 1 s with extraction of the precession frequencies and appropriate conversion producing the magnetic field data shown in Fig. 3.27(a). The DC component has been subtracted from both data sets so that the magnetic field fluctuations of both schemes could be easily compared. The sensitivity of both magnetometer's can be estimated using the noise spectrum of the magnetic signal as provided in Fig. 3.27(b) showing noise floors of $3.4 \text{ pT}/\sqrt{\text{Hz}}$ and $15.6 \text{ pT}/\sqrt{\text{Hz}}$ for a measurement time $T = 1 \text{ ms}$ using the AM and FM implementations, respectively. Logarithmic binning was used on the spectra by applying the arithmetic mean on data residing in each frequency bin. These noise floors coincide reasonably well with the anticipated sensitivities estimated from the CRLB which were measured to be $3.7 \text{ pT}/\sqrt{\text{Hz}}$ using AM and $16 \text{ pT}/\sqrt{\text{Hz}}$ for the FM technique. The difference in sensitivity between the two systems is primarily a consequence

of less efficient optical pumping in the FM regime as the maximum light power available from the VCSEL is an order of magnitude less than that of a diode laser. The lower level of spin coherence generated is easily observed in Fig. 3.26 by comparing the signal amplitude gained with both techniques.

Chapter 4

Waveform Tracking with a FID Magnetometer

FID OPMs are now routinely used to perform DC magnetic field measurements in experiments ranging from searches for electric dipole moments [93] to tests of quantum limits of sensing [33]. Equally attractive is their use to perform AC measurements that also benefit from miniaturised instrumentation; this regime however, has yet to be explored. In this chapter we propose and demonstrate the FID magnetometer's capability in executing DC and AC measurements, and exemplify its use in tracking time-varying magnetic signals in a static bias field of similar strength to that of the Earth's ($\sim 50 \mu\text{T}$). The experimental results and content in the forthcoming sections are adapted from [31], by Hunter *et al.* The sensor implements a microfabricated vapour cell, thus is amenable for miniaturisation with the added advantages of increasing spatial resolution of potential sensor networks, reducing power consumption, improving portability and lowering the cost of fabrication whilst retaining competitiveness with existing technologies [13]. Although the microfabricated nature of these vapour cells sets a fundamental limit on the optimum sensitivity achievable, it also introduces large improvements in the sensor bandwidth by virtue of the rapid spin decoherence that facilitates a quick atomic response to rapidly fluctuating fields [16]. The FID implementation is subject to certain technical limitations that are investigated in detail;

for example, we assess the impacts that atomic spin relaxation and a finite detection time have on the frequency response of the device. Also, nonlinearities induced by sufficiently strong time-varying magnetic signals are observed and modelled in terms of Bessel functions of the first kind. We discuss this in the context of potential readout errors that can occur in the presence of prominent FM effects that introduce numerous frequency components into the FID spectrum. This increases the difficulty of frequency extraction using traditional digital signal processing techniques such as DFTs or fitting algorithms; therefore, places an upper limit on the sensor’s dynamic range with regards to AC magnetic field perturbations that can be reliably reconstructed.

4.1 Experimental Methodology

Specific details of the magnetometer’s operation are discussed extensively in the previous chapter, with an experimental schematic illustrated in Fig 3.3. The AM configuration was adopted with a sensor head comprising of a MEMS Cs vapour cell. The alkali number density is optimised based on the SNR and transverse relaxation rate to achieve maximum magnetometer precision; further increase of the alkali density provides a way to enhance the atomic bandwidth at the expense of degraded sensitivity [16]. The sampling procedure in FID measurements has a crucial impact on the sensor bandwidth. To reiterate, FID magnetometry is implemented in two sequential steps, the first step being optical pumping in which the atoms are prepared in a well-defined spin orientation through their interaction with resonant or near-resonance light. In the second step, probing, direct detection of the free evolution of the spins allows a measurement of the strength of the magnetic field $|\vec{B}|$. The pumping and probing sequence is shown in Fig. 3.2(a) with the pump stage lasting a time interval T_p , and the detection phase extending over a time T_r , so that the total single-measurement time is $T = 1/f_d = T_p + T_r$, where f_d is the sensor repetition rate. Measurements are performed inside a three-layer μ -metal shield to reduce ambient magnetic fields to several nT and suppress technical noise contributions including line noise, allowing a reliable characterisation of the sensor’s frequency response. Two sets of Helmholtz coils

are placed inside the shield to produce a measurement field along the most sensitive axis, orthogonal to the beam propagation axis. The first is driven by a DC current supply (powered by a 12 V car battery) that was designed to generate a stable and uniform bias field that can surpass the Earth’s magnetic field. The second set of coils are used for modulation purposes and consist of a single turn, with a resistor placed in series to control the range of producible magnetic fields available when driven by an arbitrary function generator which has a maximum voltage of 10 V. The time constant of the RL circuit was measured to be short enough that no roll-off was observed up to the MHz range.

The presence of N₂ buffer gas yields a broadened optical spectrum consisting of two merged peaks, with slight overlap between the ground state resonances for this particular vapour cell. The magnetometer precision is improved by tuning the laser frequency to the $F = 3 \rightarrow F'$ absorption line as in previous experiments. The extended spin lifetime reduces the atomic bandwidth; however, this is significantly outweighed by the large sensitivity enhancement. Each experiment employs synchronous optical pumping for a duration $T_p \simeq 330 \mu s$, while the probing time T_r was set according to the specific experiment as described in the forthcoming sections. Pumping was performed at the maximum power available of around 6 mW while the probe power was set to $200 \mu W$, with the beam area kept consistent at 2.5 mm^2 . An elevated pump power is required to maximise the induced spin coherence through optical pumping as discussed in Section 3.5.2. As adopted previously, detection of spin precession was performed using a balanced polarimeter to analyse polarisation rotation in the transmitted light. An initial transient, instigated by the difference in absorption between the two ports of the polarimeter, is typically observed at the start of each FID signal and is simply removed before processing the data. The acquired FID signal trains are post-processed, predominantly using a fitting routine (see Section 3.3), to extract the precession frequency of the atoms and track their response to any externally applied field perturbations. Alternative estimators can also be implemented, for instance the time series can be analysed in the frequency domain; from the estimated frequency of the spectral peak and the field-dependence of the Larmor rate, the strength of the

field can be inferred. Our experiments are performed at two cell temperatures, 85 °C and 100 °C, and from the damped sinusoid fit the power broadened magnetic linewidths were estimated to be 2.8 kHz and 4.3 kHz, respectively. This has important implications when considering the achievable bandwidth and sensitivity, which are widely utilised and closely interlinked performance indicators for these atomic sensors.

4.2 Waveform Reconstruction of AC Magnetic Signals

In this section, we investigate the magnetometer’s capability at reproducing applied oscillating magnetic field perturbations. The repetition rate of the sensor was set to $f_d = 1$ kHz and the power broadened transverse relaxation rate was close to $\gamma_2 \simeq 2.8$ kHz. The time-varying magnetic field was inferred from the Larmor frequency of subsequent FID traces in a signal train by applying the LM algorithm to the data using the DS model provided in Eq. (3.2), as adopted in previous experiments [24]. The ensuing reconstructed signals were then fit to a sinusoidal model using the same algorithm. A 7 nT applied field oscillating at 20 Hz was sampled in 1 ms increments

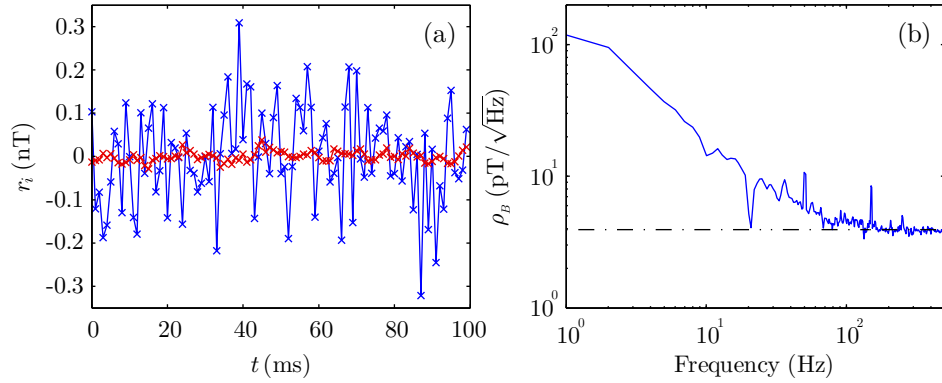


Figure 4.1: (a) An applied 7 nT sinusoidal modulation oscillating at $f_m = 20$ Hz was reconstructed by the magnetometer at a repetition rate of $f_d = 1$ kHz over a period of 25 s. Fit residuals for a 100 ms portion of the reconstructed waveform (blue crosses), and for a weighted average of 247 similar segments (red crosses). The standard deviation of the fluctuations are 112.6 pT and 11.7 pT for the single-shot and averaged waveforms, respectively. (b) Noise spectra for the single-shot measurement residuals, over a period of 1 s, converted to the frequency domain using a DFT. The dot-dashed line is an indication of the optimum sensitivity of the device at $3.9 \text{ pT}/\sqrt{\text{Hz}}$.

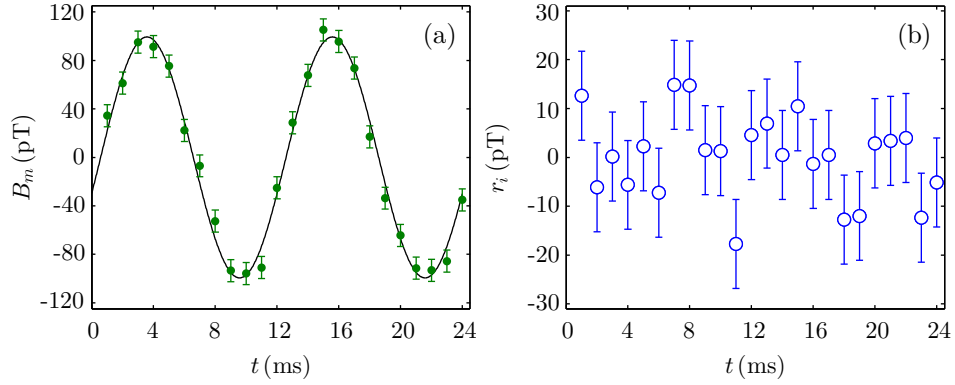


Figure 4.2: (a) Reconstructed waveform (208 averages) of a 100 pT magnetic field perturbation oscillating at 83.3 Hz (green dots), and associated fit to a sinusoidal model (black line). (b) Corresponding fit residuals that have a calculated standard deviation of 8.7 pT.

by the magnetometer over a period of 25 s. Figure 4.1(a) presents the residuals of the sinusoidal fit (blue trace) for 100 ms of the reproduced waveform. A weighted average was then implemented on 247 snapshots of similar 100 ms segments over ~ 25 s. This averaging is possible as the frequency of the modulation field is a subharmonic of the repetition rate of the sensor. The fit residuals of the corresponding waveform (red trace) demonstrate a clear improvement in the magnetic field fluctuations observed in the time domain. The best sensitivity of the device is exhibited in Fig. 4.1(b) in the form of a DFT of the single-shot fit residuals over a period of 1 s. In order to smooth out the spectrum, a running average was performed over the full 25 s data set enabling features such as line noise to be observed in the spectrum. The dip occurring at 20 Hz is due to noise suppression at the modulation frequency as a consequence of the fit. The sensitivity close to the Nyquist limited bandwidth of the sensor, defined as $f_N = f_d/2$, was calculated to be around $3.9 \text{ pT}/\sqrt{\text{Hz}}$. The magnetometer's impressive sensitivity is further emphasised in Fig. 4.2(a) showing the signal reconstruction of a smaller 100 pT magnetic field perturbation. Each data point in Fig. 4.2(a) was an average of 208 points in order to distinguish the oscillation from noise; therefore, the expected fluctuations in the residuals would be approximately 8.6 pT if one multiplies the measured sensitivity by the square root of the measurement bandwidth, calculated as $1/(208 \times 1 \text{ ms}) \simeq 4.8 \text{ Hz}$. This closely resembles the measured RMS deviation of

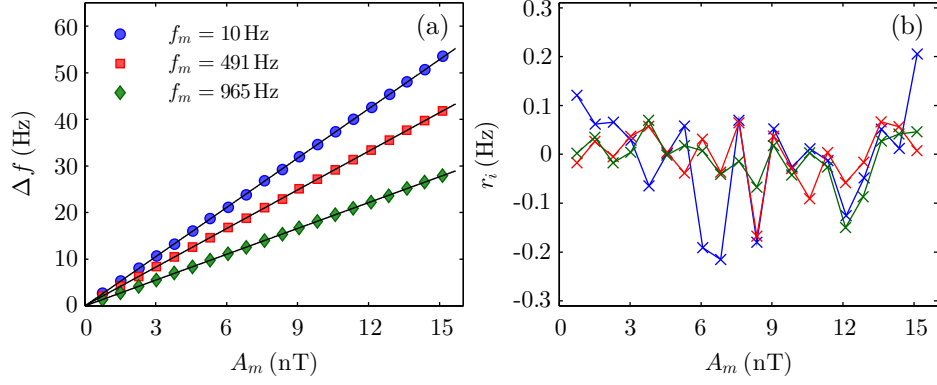


Figure 4.3: (a) Linearity of the detector observed by measuring the peak-to-peak frequency deviation at a range of field modulation amplitudes using $f_m = 10$ Hz (blue), $f_m = 491$ Hz (red), and $f_m = 965$ Hz (green). The solid lines are linear fits to the data. The data at $f_m = 965$ Hz resides beyond the Nyquist limited bandwidth and is aliased back into the detection band. (b) Linear fit residuals.

8.7 pT calculated from the fit residuals in Fig. 4.2(b).

FM can significantly distort the spectrum of a FID signal thus one may consider using a low modulation amplitude to characterise the frequency response of the sensor. Figure 4.3(a) shows the peak-to-peak frequency deviation observed as the amplitude of the AC field was varied using three different modulation frequencies. Oscillating frequency components beyond half the repetition rate of the magnetometer are aliased in accordance with the Nyquist theorem. The modulation coil was calibrated using the magnetometer's DC response by incrementally increasing the static magnetic field. The conversion from coil voltage to magnetic field can then be determined empirically from the straight line dependence. The absence of FM effects is highlighted by the lack of trends in the straight line fit residuals, shown in Fig. 4.3(b), which are several orders of magnitude smaller than the applied oscillation. The reduced gradients at higher frequencies indicate that the reconstructed signal diverges from the true waveform as a consequence of the magnetometer's inherent frequency response. After appropriate scaling to magnetic field with respect to the gradient, the standard deviations were calculated to be 30.8 pT, 21.1 pT, and 27.7 pT for the $f_m = 10$ Hz, $f_m = 491$ Hz, and $f_m = 965$ Hz data sets, respectively.

A characterisation of the FID magnetometer's frequency response for various

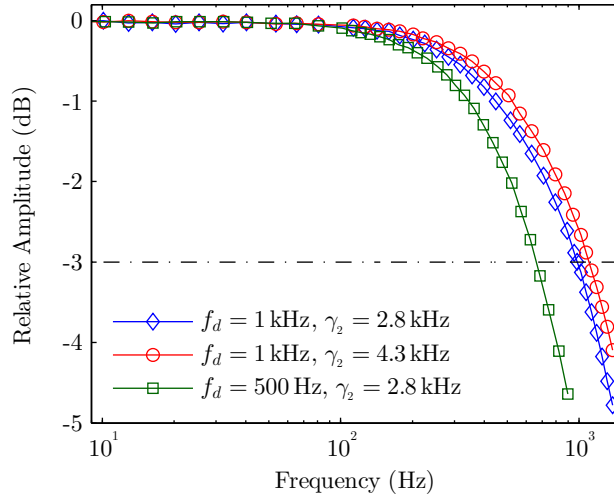


Figure 4.4: Frequency response of a FID magnetometer using different experimental parameters as noted in the legend. Data points with frequencies above the Nyquist limit are folded back within the detectable bandwidth through aliasing. Interpolation has been utilised as a guide for the eye allowing extraction of the (-3 dB) bandwidths, estimated to be 671 Hz (green), 975 Hz (blue), and 1.1 kHz (red). The observed response is a consequence of the subtle interplay between the spin decoherence and repetition rates of the sensor.

experimental parameters is shown in Fig. 4.4(a). An oscillating B -field of amplitude $A_m \simeq 7$ nT was administered with the modulation coils at a range of frequencies. Data was collected for different repetition and damping rates in an attempt to understand the independent effects of these experimental parameters on the frequency response of the system. As anticipated, clear attenuation of the reconstructed waveforms occur at higher frequencies as a consequence of the subtle interplay between the repetition rate and spin-coherence lifetime. Sharp discontinuities in the time domain can lead to truncation artefacts that increase the spectral linewidth of a single FID signal resulting in an enhancement of the the overall sensor bandwidth, as seen in Fig. 4.4(a); the data taken at $f_d = 1$ kHz and $\gamma_2 = 2.8$ kHz experienced significant truncation in comparison to the other data sets. The detection window can be thought of as a rectangular function in the time domain whose corresponding Fourier transform pair is a sinc function; therefore, reducing the probing time will inevitably increase the width of the sinc function. These truncation artefacts are commonplace in FID spectra, especially in

NMR measurements, and are often seen as a disadvantage in this application due to the loss in spectral resolution [75]. As well as improving the bandwidth of the sensor, signal truncation can also increase the magnetometer precision by improving the CRLB which is optimised at $T_r = 2/\gamma_2$ [24].

4.3 Technical Considerations

The effects shown in Fig. 4.5 demonstrate that an oscillating field will cause the Larmor frequency to evolve within a single detection window, giving rise to a frequency modulated signal. This can still be adequately described by the traditional FID model with the addition of a time-dependent frequency term,

$$M_x(t) = A e^{-\gamma_2 t} \sin\left(\omega_0 t + \phi_0 + \gamma \int_0^t B(\tau) d\tau\right), \quad (4.1)$$

where $B(t)$ is the oscillating component of the magnetic signal. If we consider single tone modulation, $B(t) = A_m \cos(\omega_m t + \phi_m)$, then Eq. (4.1) becomes,

$$M_x(t) = A e^{-\gamma_2 t} \sin[\omega_0 t + \phi_0 + \beta \sin(\omega_m t + \phi_m)], \quad (4.2)$$

where $\beta = \gamma A_m / \omega_m$ is the modulation index (or depth) assuming a flat frequency response. This expression can be further simplified using the Jacobi-Anger expansion [94],

$$M_x(t) = A e^{-\gamma_2 t} \sum_{n=-\infty}^{\infty} J_n(\beta) \sin[(\omega_0 + n\omega_m) t + \phi_0 + n\phi_m], \quad (4.3)$$

where $J_n(\beta)$ is a Bessel function of the first kind. It can be clearly seen from Eq. (4.3) that multiple frequency components would begin to appear in the FID spectrum at large modulation depths.

A strong oscillating field was supplied to the modulation coils, as seen in the top plot of Fig. 4.5(a), that introduces distinctive FM features into the FID spectrum. Figure 4.5(b) shows several snapshots of the ensuing FID spectra together with their

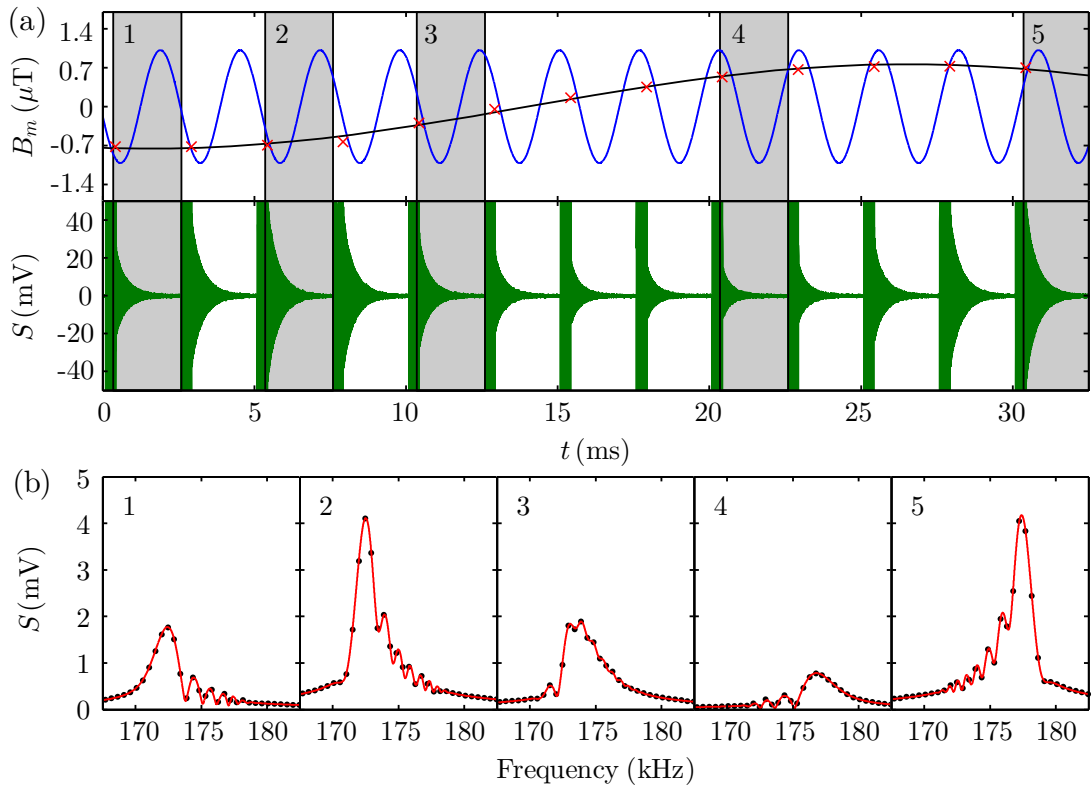


Figure 4.5: (a) Top: oscillating component of the magnetic field (blue line) generated by the modulation coils, aliased reconstructed waveform (red crosses), and corresponding fit to a sinusoidal model (black line). Bottom: time series of a FID signal train (green trace). (b) Snapshots of frequency modulated FID spectra (black dots) and their associated best fits converted to the frequency domain (red lines). The numbers (top left) refer to the corresponding time domain signals that are highlighted by a grey background.

associated fits to the model described in Eq. (4.3). Zero-padding interpolation was applied to the spectra of the time domain fits to enhance visualisation of the correspondence between the data and fit model in the frequency domain. The temperature of the vapor cell was 85°C and the repetition rate was set to $f_d = 400$ Hz allowing the spin polarisation to fully equilibrate. Almost a full oscillation occurs within a single FID cycle giving rise to an aliased waveform if one tracks the frequency of the spectral peak, as evidenced by Fig. 4.5(a). This is a common feature of data acquisition systems and is typically rectified with the application of an anti-aliasing filter to eliminate these high frequency components; this is not an ideal solution for the FID magnetometer as

the precession signal would also be attenuated. In fact, the true frequency of an aliased waveform can be inferred by adjusting the repetition rate slightly and observing the frequency variation in the reconstructed signal. It can also be noticed that even at these high modulation depths the correlation between the actual and reconstructed signal amplitudes are relatively close when considering the sensor’s frequency response. These high frequency oscillations will cause the lineshape of the FID spectra to be contingent on the phase of the respective magnetic signal. For example, the sharp initial change in magnetic field experienced by the magnetometer (see snapshot 4) leads to a larger spread in frequencies and dramatically reduced FID amplitude. This is a consequence of the magnetic field measurement being weighted by signal damping, placing emphasis on the initial portion of the FID signal. Introducing such complexity into the FID spectrum will inevitably increase the difficulty of the magnetometer read-out process especially if multiple sidebands share similar amplitudes (see snapshot 3). The model in Eq. (4.3) thus provides an understanding of the sensor’s capabilities in accurately reconstructing an AC magnetic signal.

4.4 Unshielded Operation

Unshielded operation is an important requirement in many magnetic sensing applications including detecting unexploded ordnance, archaeological prospecting, and geophysical surveying. This is difficult to achieve for the most sensitive SERF magnetometers in which the ambient magnetic field has to be nullified to avoid saturating the sensor. Scalar OPMs, such as the FID magnetometer discussed in this work, are advantageous as they have an extensive dynamic range that surpasses that of the Earth’s field and exhibit considerably superior bandwidth, at the expense of reduced sensitivities limited by spin-exchange collisions. The upper dynamic range limit has not been observed experimentally for this implementation, nevertheless it will be subject to technical limitations in both signal sampling and the atomic response. For example, the sampling rate was set to $f_s = 2$ MHz for many experiments conducted throughout this work, equivalent to around 11 samples per cycle in the Earth’s field ($\omega_L/2\pi \simeq 175$ kHz

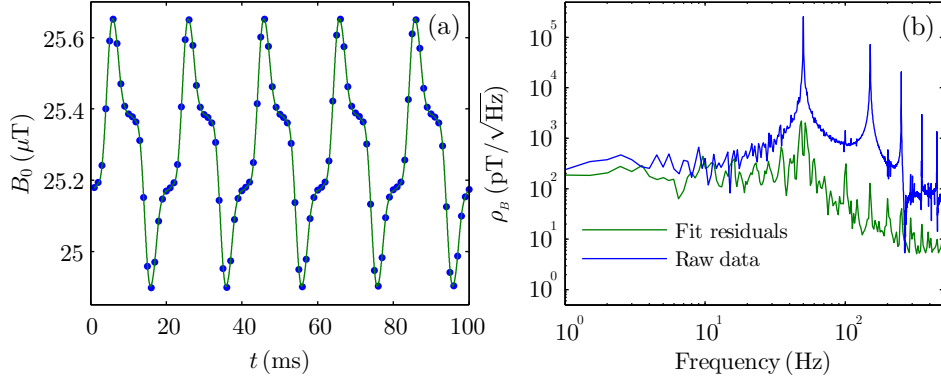


Figure 4.6: (a) Time-varying magnetic signal (blue dots) reconstructed with a FID magnetometer in an unshielded environment, and associated fit (green line) to the model in Eq. (4.4). The periodic waveform is a manifestation of noise from the power lines oscillating at 50 Hz and associated harmonics. (b) Noise spectrum of the raw waveform (blue) and fit residuals (green).

for Cs). This technical limitation can be circumvented using FPGAs with their high sampling capabilities; however, complex mathematical procedures are difficult and inefficient to implement on these hardware devices. For the FID magnetometer, the lower dynamic range limit is restricted by the detection time, the sensitivity of which can be optimised based on the transverse relaxation rate as discussed in Section 3.3.5. The smallest detectable signal will be on the order of 150 nT, equivalent to the detection of one precession cycle for a probe time $T_r = 2$ ms. This should not be misinterpreted as the magnetometer sensitivity, typically defined as the smallest magnetic field fluctuation observable. Such a limitation will seldom be an issue as the FID configuration is well suited as a scalar sensor operating in μT -level bias fields, as necessary in many unshielded applications.

Figure 4.6(a) shows the first 100 ms of a waveform reconstructed in an unshielded environment using the FID magnetometer. The relaxation rate of the sensor was measured from the fitted damping rate to be 2.8 kHz, and the driving frequency was set to 1 kHz resulting in a Nyquist limited bandwidth of 500 Hz. The unshielded magnetic

field signal B_{us} was tracked for 5 s and modelled using the following expression,

$$B_{us} = \sum_{n=0}^{N_h-1} B_n \sin[(2n+1)\omega_0 t + \phi_n], \quad (4.4)$$

where B_n and ϕ_n are the amplitude and phase of the n^{th} odd harmonic, $\omega_0/2\pi$ is the fundamental frequency, and N_h is the total number of odd harmonics. It is clearly evident that the FID magnetometer has the ability to reconstruct complex waveforms composed of multiple frequency components as long as they reside within the sampling bandwidth. A subsidiary magnetic field was applied using two-axis field coils to tune the precession rate close to the synchronous modulation frequency, set to $\omega_m/2\pi = 87.5$ kHz. It is possible to operate the magnetometer without field compensation; however, this served to align the field direction closer to the most sensitive axis to increase the measurement precision. The fundamental frequency was measured to be $\omega_0/2\pi = 50.1$ Hz, corresponding well with that expected from noise produced by the power lines. A total of six harmonics were used in the fit model, and the amplitude of the first three harmonics were estimated to be 270 nT, 109 nT, and 22.1 nT. A DFT was applied to the raw magnetic field trace and the associated fit residuals to produce the noise spectra shown in Fig. 4.6(b). It can be seen from the residuals that the fit suppresses the noise peaks by around two orders of magnitude, although slight residual trends do still exist. The model in Eq. (4.4) does not account for low frequency drifts, or the much smaller amplitude even harmonics that are present; nonetheless, it can be seen that the optimal sensitivity of the device is around $8 \text{ pT}/\sqrt{\text{Hz}}$ at higher frequencies which is close to that expected when operating in a shielded environment when comparing to Fig. 4.1(b). The reduction in baseline sensitivity at the high frequency range is most likely attributed to the measurement field not being perfectly aligned perpendicular to the beam propagation axis. Line noise such as that seen in Fig. 4.6 is ubiquitous in modern day society, and is a real problem in most sensing applications. For example, much of the signal content in an MCG measurement resides close to the fundamental noise peak which will be orders of magnitude higher in amplitude, especially considering the extensive electrical equipment one would expect in the medical environment. These

Chapter 4. Waveform Tracking with a FID Magnetometer

technical noise sources will also be subject to large fluctuation which is problematic as a consistent measurement platform is critical for medical diagnosis. Applying multiple sensors in a gradiometric measurement circumvents these issues as both sensors should experience the same ambient field that cancels after subtraction, whilst spatially dependent fields emanating from a localised source should remain.

Chapter 5

Suppression of Operational Systematics

In this chapter, we implement a Ramsey-style detection mode to observe spin precession and decoherence dynamics in-the-dark. Similar readout methods have been previously employed to measure ground state coherences [95, 96], derived from the experiments performed by Franzen in 1959 [66]. The basic principle involves optically pumping an atomic ensemble into a highly polarised state, switching the light off, and subsequently inferring the spin phase at the instant a readout pulse is applied after a set delay time following the pump stage. This phase-sensitive measurement enables an accurate determination of the magnetic field in which AC Stark shifts have been effectively suppressed. The intrinsic spin dynamics can also be monitored by superimposing the results gained at a series of different delay times. This technique is adopted to measure depolarisation in the ground state manifold for a series of miniaturised Cs vapour cells. Power broadening introduced by residual optical pumping during readout is eliminated allowing inference of the relaxation rate that is intrinsic to the sensor head itself. The data quality is compared to another commonly used method based on extrapolating to zero-light power [68]. We compare our experimental observations to theoretical predictions based on the dimensions, buffer gas content and temperature of each sensor head. This enables an in-depth analysis of its performance as a magnetometer and

provides a benchmark for optimisation during cell fabrication.

5.1 Probing In-The-Dark

5.1.1 Principle of operation

The underlying principle of the PITD experiments is predicated on nondestructively detecting the free propagation of preoriented atomic spins and, in turn, avoiding systematic effects that are induced by the light-atom interaction during readout. A schematic of the experimental arrangement used to implement this detection mode is depicted in Fig. 5.1 comprising a FID magnetometer operated in the AM configuration as adopted previously (see Section 3.2), with some slight modifications. The intensity signal is monitored using a calibrated photodiode that acts as the trigger for signal processing of the FID traces, whilst additionally enabling monitoring of the laser intensity during each phase of the experiment. The sensor repetition rate is set low enough that the Zeeman sublevel populations can fully thermalise prior to the upcoming pump stage. The half-wave plate and Glan-Thompson polariser combination ensure purity in the lasers linearly polarised output that is aligned along the desired axis of the electro-optic modulator (EOM). This switches the light polarisation from circular to linear for optimum performance during the optical pumping and detection stages respectively, as opposed to previous instances in which elliptically polarised light was utilised. Circularly polarised components are a source of vector light shift along the beam axis that materialises as a fictitious magnetic field, known as the AC Stark shift [90]. Electing to use a linearly polarised probe should minimise this effect; however, complete light shift suppression is difficult in practice as it requires an extremely pure linear polarisation and precise alignment of the beam propagation and polarisation axes with respect to the transverse magnetic field [97]. Active alignment of the magnetic field direction is not performed in these experiments hence light shifts are still present. Additionally, further contributions can arise due to the beams interaction with various optical elements, including the glass windows of the vapour cell, that introduce ellipticity into the light polarisation [98]. Light shift cancellation is possible using other methods

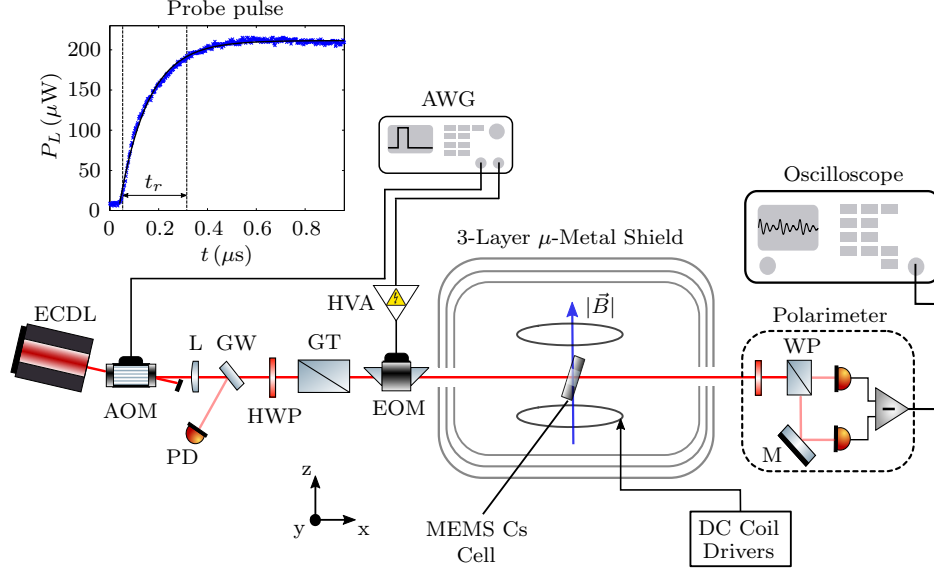


Figure 5.1: Experimental set-up for an amplitude modulated FID magnetometer employing a MEMS Cs vapour cell containing N_2 buffer gas at a pressure of approximately 212 Torr. The EOM switches the light polarisation between circular and linear during the pump and probe stages, respectively. An arbitrary waveform generator produces the modulation waveforms necessary for Ramsey-type detection. The rise time of the AOM pulses were calculated to be $t_r \simeq 260$ ns as seen in the upper-right corner plot. (ECDL, external cavity diode laser; EOM, electro-optic modulator; HVA, high voltage amplifier; WP, Wollaston prism; MEMS, microelectromechanical system.)

such as a two-color configuration [99, 100], or astutely detuning the laser frequency with respect to the collisionally broadened optical spectrum as described in Section 3.4.3. In these cases, this requires either adding a degree of complexity to the system or compromising the best sensitivity achievable with use of a nonoptimal laser frequency. The presence of AC Stark shifts is useful in these experiments as it serves to demonstrate the suppression experienced when implementing a Ramsey-like detection scheme. The modulation waveforms supplied to both the AOM and EOM are easily synchronized as they are sourced from the same waveform generator. The EOM supply voltage is switched synchronously with each pump-probe cycle; a high voltage amplifier (HVA200) then elevates this voltage to the desired level necessary to induce a circularly polarised output after the light traverses the EOM. The high voltage amplifier has a bandwidth of around 1 MHz thus greatly exceeds the sensor repetition rate¹. Thermal

¹As a secondary experiment, one could use the light polarisation as a source of perturbation by modulating resonantly at the Larmor rate, with continuous pumping power.

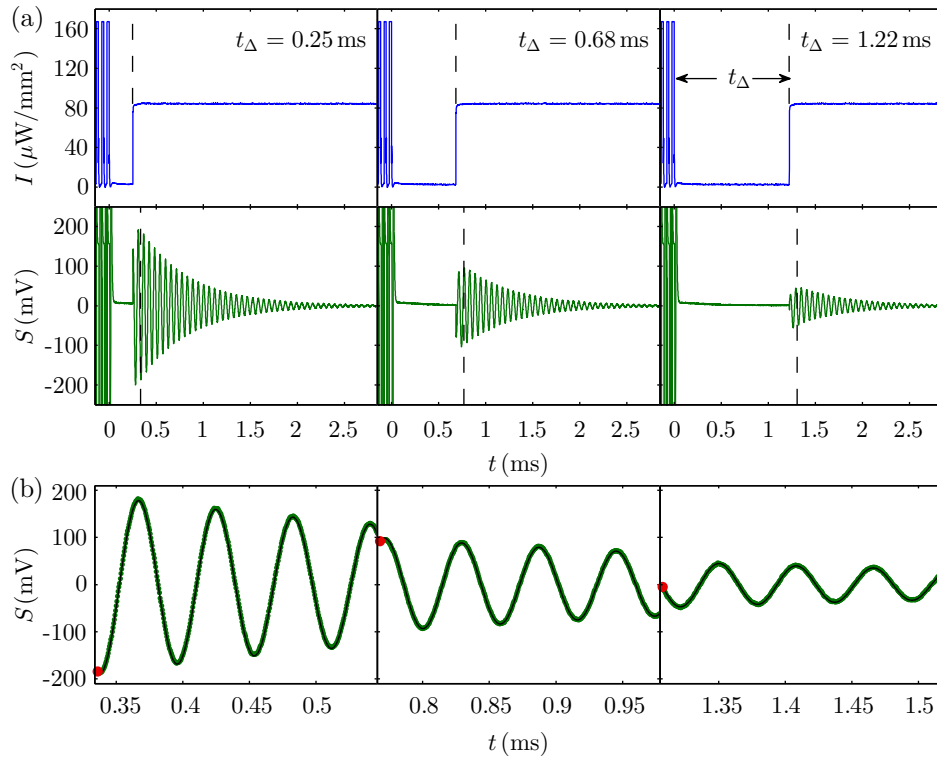


Figure 5.2: Selection of three signals showing (a) Top: the laser intensity measured after the AOM, set to approximately zero for a delay time t_Δ after optical pumping. The peak pumping intensity was measured to be $2.4 \text{ mW}/\text{mm}^2$, contrary to that shown as the signal was saturated during the pump stage. For illustrative purposes, only a small portion of the pump stage was shown. Bottom: ensuing FID traces measured by the polarimeter. Data prior to the dashed line is excluded to improve the fitting quality. (b) Initial $210 \mu\text{s}$ portion of the fitted FID traces. The red dot symbolises the first data point of the fit used to infer the spin state at the instant the probe was switched on.

drifts can cause significant alterations in the static birefringence of the lithium niobate crystals that compose the EOM and is often the prime contribution to technical $1/f$ noise. This issue can be resolved with careful beam alignment as the EOM comprises two perpendicularly oriented crystals, enabling cancellation of this effect up to a temperature sensitivity of less than $1 \text{ mrad}/^\circ\text{C}$.

Figure 5.2 demonstrates the concept of PITD. The Cs spins are oriented into a specific quantum state by synchronously pumping the atomic ensemble, using a strong circularly polarised laser beam, for a duration T_p that extends to at least a single relaxation period in order to generate a large degree of spin coherence. In analogy to

Ramsey spectroscopy, the electric field amplitude is set to zero for a finite duration after pumping, denoted as the delay time t_{Δ} , permitting the spin coherence to evolve freely in-the-dark in the presence of a controllable static field. An oscillation in the phase of the ground state population at the set Larmor frequency will occur during this time interval as well as decoherence due to various spin relaxation phenomena. The top plots show the laser intensity signals monitored before striking the vapour cell for a selected subset of delay times. The peak pump intensity was consistent with previous experiments at $I_p \simeq 2.4 \text{ mW/mm}^2$. This is not represented in Fig. 5.2(a) as emphasis is placed on observing the probe power with high voltage resolution, resulting in saturation of the signal during the pump stage. Once the sample is polarised, observation of the spin precession is performed after a delay time t_{Δ} at a probe intensity of approximately $I_r \simeq 80 \text{ }\mu\text{W/mm}^2$. During this readout period the atoms will become subject to the systematic effects induced by the probe. The typical rate of absorption for these vapour cells was determined experimentally (see Section 3.5.2) to be in the kHz-regime. The rise time of the readout pulses were measured to be $t_r \simeq 260 \text{ ns}$, thus are adequately short as to avoid residual optical pumping effects from negating the validity of the technique. The intensity of the linearly polarised light interacting with the atoms during the dark phase is less than $2 \text{ }\mu\text{W/mm}^2$. Oscillation and decoherence in the occupation of the Zeeman manifolds will alter the birefringent properties of the sample, observable in the induced rotation angle of the linearly polarised probe after the laser intensity is elevated. This will be represented in the ensuing FID traces that are measured by the polarimeter during readout as presented in the bottom plots in Fig. 5.2(a) for the chosen subset of delay times. By fitting the appropriate theoretical model to these signals, one can deduct the quantum state of the atomic ensemble at the exact moment the probe beam was switched on through extrapolation as symbolised by the red dots in Fig. 5.2(b). It is then possible to reconstruct the evolution of the spin coherence in its entirety in a nondestructive manner by incrementally varying the delay time and applying this procedure to a series of FID traces in a signal train. For technical reasons the magnetic field was set to $5 \text{ }\mu\text{T}$ for these experiments as this enables a large portion of the precession signal to be reconstructed in sufficiently small increments of

t_{Δ} ². This was limited by the repetition rate of the sensor and buffer size of the oscilloscope³. Signal samples that trail the dashed line in the bottom plots in Fig. 5.2(a) were removed to improve the fitting quality. The quantity of truncated points is kept consistent for each trace that is processed and the delay time is adjusted accordingly. As discussed in Section 3.3.3, the implemented DS model does not perfectly resemble the experimental data. The distorted lineshape and multiple harmonics evident in the FID spectrum will most likely be a source of systematic error during the fit, that may be influenced by the changing SNR evident at different delay times or probe intensities. The nature of how these systematic effects propagate through the reconstructed precession signal is fairly convoluted; therefore, a more complete understanding of the spin dynamics with an adjusted model is desirable. It will be seen in later sections that these errors are the limiting factor in the measurement accuracy but still reflect a vast improvement in comparison to the light shift that would be experienced at equivalent probe powers.

5.1.2 Optical pumping spin dynamics

The premise of achieving an accurate measurement using this technique relies on the fact that the spin dynamics remain consistent during optical pumping so that the occupational phase of the Zeeman sublevel population is well defined. This should indeed be the case when operating with fixed system parameters. Unfortunately, the pumping induced spin state of the atoms will depend on various experimental conditions including the laser frequency detuning, cell temperature and light polarisation that all impact the optical pumping efficiency and can drift over time. Also, similar to the source of heading errors, misalignment in the sensor orientation with respect to the measurement field can effect the distribution of atomic population among the ground state manifold. Experimental $1/f$ noise is somewhat controllable with refined electronics including PID feedback loops; however, the latter orientation-based issue is more difficult to circum-

²The time steps in the delay time t_{Δ} must be shorter than half a Larmor period to ensure adherence to the Nyquist limit.

³The repetition frequency is set according to the relaxation rate and the buffer size of the oscilloscope limits the longest acquisition time that can be used at a chosen sample rate.

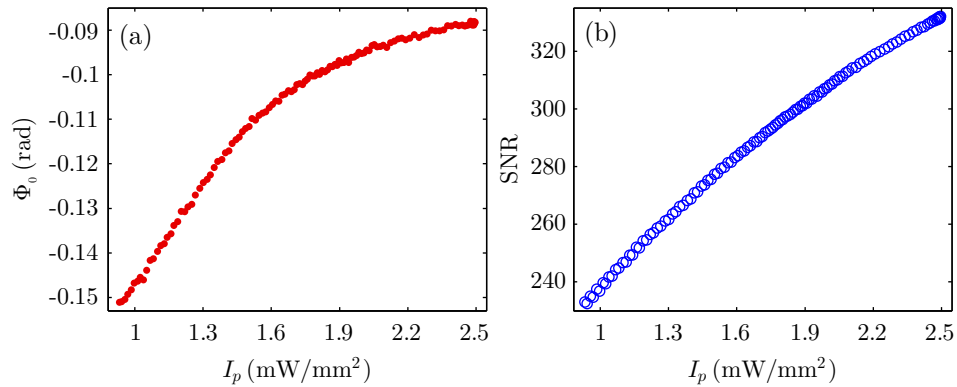


Figure 5.3: (a) Dependence of the peak optical pump intensity on the spin angle measured directly after the pump stage, using the FID traces monitored during readout and extrapolating with a DS model. (b) SNR of the FID signals acquired in the readout phase.

vent as one would need to monitor the pumping induced spin phase with regularity to ensure it has not shifted, which could place limitations on the sensor bandwidth.

In Fig. 5.3(a) we monitor the direction of the spin vector for varying pump intensities at the moment the light was switched off. A digital high-pass filter was applied to the FID signal train post-acquisition which vastly improves the overall quality of the nonlinear fit. The response of the filter does shift the phase of the FID traces by a small amount and this has been accounted for in the data shown in Fig. 5.3(a). It can be seen that there is an upward trend on the initial spin phase as the pump intensity is increased, with clear signs of saturation demonstrated at higher optical powers. This behaviour can be explained classically by considering the impact that the magnetic field has on the macroscopic spin vector during optical pumping. The static field will induce a slight torque on the spins magnetic moment if the light-atom interaction is sufficiently weak, causing it to diverge away from the optical pumping axis. The influence of the magnetic field then becomes negligible when strong pumping is applied accounting for the saturation behaviour observed in Fig. 5.3(a), as the spin vector becomes well aligned with the beam propagation direction. In allusion to previous discussions, one could attribute this trend as an artificial phase response arising due to systematics in the fitting routine at different SNRs. Although possible, the estimated initial phase exhibits more distinctive saturation behaviour in comparison to the measured SNR,

shown in Fig. 5.3(b), that perhaps suggests this is not the case. Also, these systematic effects are particularly discernible at lower SNRs which is not representative of the signals considered in this instance. Another noticeable observation is that the spin angle does not seem to be saturating at exactly zero phase. This could be attributable to many factors, the most probable being that the beam propagation direction is not exactly oriented perpendicularly to the applied magnetic field as there is no active alignment in this system. Consequently, the steady state atomic population induced after pumping would have small residual components residing outside the stretched state resulting in a shift in the saturated spin angle. Also, any ellipticity introduced into the beam prior to interaction with the atoms could effect the atomic polarisation in a similar way. Another potential source is that the aforementioned systematic effects could cause an overall phase offset in every fitted FID trace in the signal train.

PITD leads to some particularly interesting observations when tuning the laser frequency to a different hyperfine transition as seen in Fig. 5.4. There is approximately a π phase difference between the reconstructed precession signals which is a possible indication that different hyperfine manifolds are being probed depending on the frequency detuning⁴. As seen in the literature [69, 70], light narrowing can produce large signal enhancement and reduced relaxation rates when implementing buffer gas cells with an adequately broadened optical spectrum. This phenomenon is based on the assumption that tuning the laser frequency close to the $F = 3 \rightarrow F'$ transition recycles atoms that decay into the $F = 3$ ground state and, in turn, enables almost complete transfer of atomic population to the stretched state in the $F = 4$ manifold (see Section 2.4.2). The small overlap between the ground state resonances then allows one to simultaneously probe the $F = 4$ ground state with a weak light-atom interaction. This is not resembled in the precession signals presented in Fig. 5.3 as one would expect the phase to remain constant when alternating between these two transitions as, theoretically, the $F = 4$ manifold is probed in both scenarios. Additionally, although there is noticeable signal enhancement when utilising the $F = 3 \rightarrow F'$ transition, the measured decoherence rates for both signals were strikingly similar. Therefore, one can conclude that power

⁴Both hyperfine ground states precess in opposite direction thus are π out-of-phase.

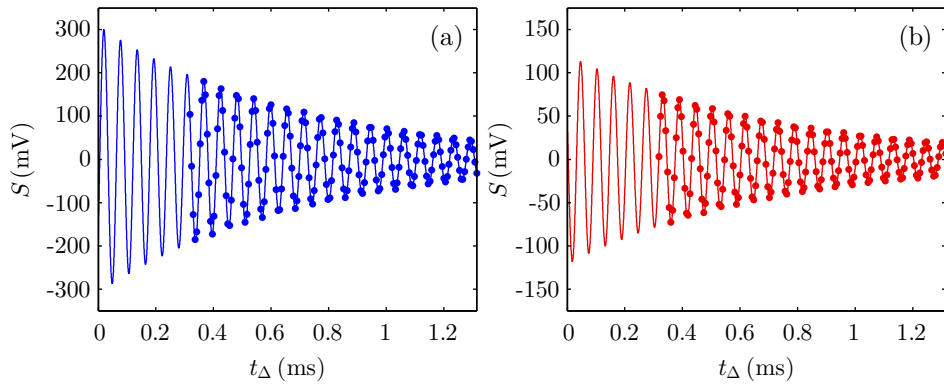


Figure 5.4: Precession signals (dots) measured by PITD and associated fit to a DS model (solid line) using a laser detuning that is (a) slightly blue-detuned from the $F = 3 \rightarrow F'$ transition, and (b) slightly red-detuned from the $F = 4 \rightarrow F'$ resonance. Collisional broadening has merged the excited state hyperfine manifolds resulting in two resolvable and slightly overlapping resonances. It can be seen that approximately a π phase flip occurs when alternating between these transitions. The relaxation rates were estimated to be 1.46 kHz and 1.42 kHz for the signals in (a) and (b), respectively.

broadening is indeed being suppressed as a result of adopting this Ramsey-style detection technique, and there is no suppression of spin-exchange collisions. In light of this, it is fair to surmise that no light narrowing is occurring as spin-exchange suppression is a pre-eminent feature of this phenomenon. Implementing the $F = 3 \rightarrow F'$ transition does lower the spin relaxation rate when adopting traditional detection methods as discussed in Section 3.6.1. This will simply be a consequence of the weaker interaction strength of this particular transition, resulting in lower levels of power broadening than would be experienced if one was to utilise the $F = 4 \rightarrow F'$ transition at an equivalent probe power. The observed signal enhancement is another recurring trait hence the extensive use of this transition with its superior sensitivity; however, the source of this improvement is still unknown. A model that accounts for factors such as collisional broadening of the optical spectrum, relative frequency detuning, and ellipticity in the light beam would be required to fully understand how the spin dynamics relate to the observed signal amplitude.

5.1.3 Light-shift suppression

In this section, we supply evidence that the systematic effects induced by the light-atom interaction during detection can be effectively suppressed with the Ramsey-like detection method described previously. As a proof of principle, several precession signals were reconstructed by PITD using a series of different laser powers during the readout phase as seen in Fig. 5.5. The same arbitrary waveform was applied to separately vary both the delay time t_{Δ} and probe power, with the ensuing signal train acquired over a 5 s period. This provided around three FID traces per set of experimental parameters that formed an average based on the measured estimators. Unfortunately, this was the maximum acquisition time available at a sample rate of 2 MHz given the buffer size of the oscilloscope. Longer time series are more prone to $1/f$ noise contributions particularly as the EOM was not temperature controlled. As eluded to before, this can be compensated for using a digital high-pass filter post-acquisition to eradicate these DC offsets or, alternatively, an additional offset parameter included in the fit model.

There are several indicators suggesting that the light-induced systematic effects have been highly suppressed, the most notable being the similarity in the fitted Larmor frequencies estimated for each signal shown in Fig. 5.5. The maximum frequency deviation between the reconstructed signals was only 1.4 Hz, equivalent to around 0.4 nT, and the largest difference between the measured damping rates was 98 Hz. It is also important to note that the observed trends did not correlate with the anticipated light shift or power broadening behaviours; however, the deviations are larger than the calculated errors for each estimator suggesting that there are some systematic effects present. Based on the lack of perceivable trends in the calculated estimators, these are likely not a consequence of the light-atom interaction but instead arise due to the systematics associated with the fitting routine itself as detailed in previous sections. Also, these reconstructed precession signal will be subject to higher levels of fluctuation generated by low frequency drifts.

Numerous FID traces are necessary to fully reconstruct the precession signals seen in Fig. 5.5, requiring long acquisition times. These signals can be extremely useful in

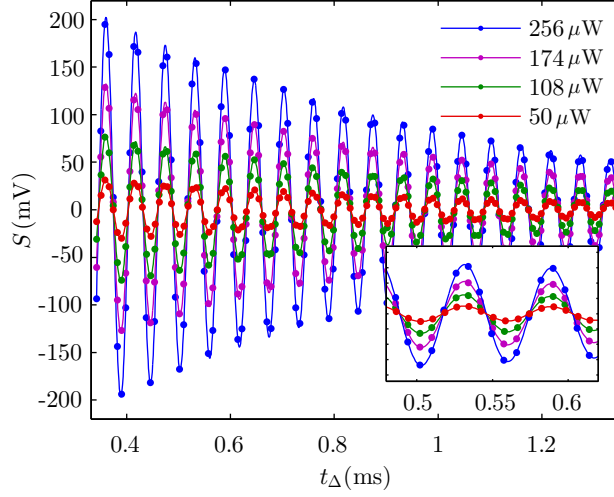


Figure 5.5: Reconstructed precession signal (dots) and corresponding fit to a DS model (solid lines) using the PITD detection scheme with different readout powers as noted in the legend. The maximum difference in the Larmor and relaxation rates were measured to be 1.4 Hz and 98 Hz, respectively.

the characterisation of intrinsic relaxation rates as discussed in later sections; however, this mode of operation would not be very practical for commercial magnetometers as the bandwidth would be severely limited. To circumvent this issue, one can utilise the fact that the phase of the atomic spins after optical pumping should remain constant if the system parameters are not altered. One can approximate the integer number of cycles that have taken place during the chosen delay time using the following expression,

$$\hat{N}_c = \|\omega'_L t_\Delta\| \quad (5.1)$$

where \hat{N}_c is the number of cycles rounded to the nearest integer, and ω'_L is the light-shifted precession rate measured from the FID trace during readout. By compensating for the fractional component left over, we can accurately determine the magnetic field as follows,

$$B_0 = \frac{\hat{N}_c + \Delta\phi/2\pi}{\gamma t_\Delta}, \quad (5.2)$$

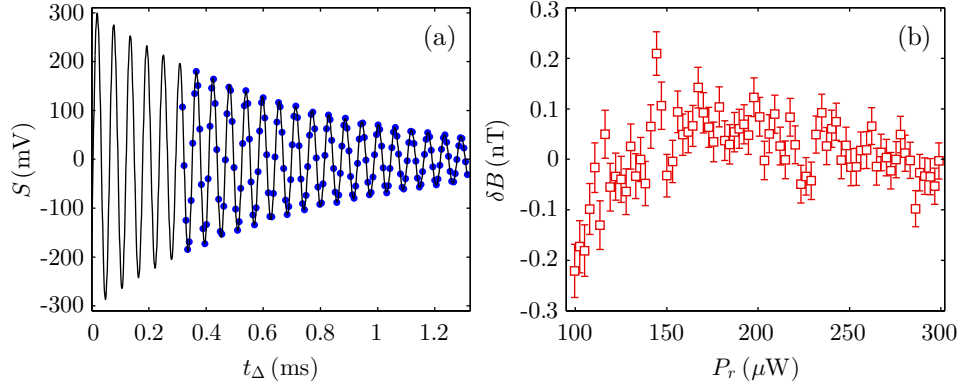


Figure 5.6: (a) Reconstructed precession signal (blue dots) measured with a readout power of $210 \mu\text{W}$, and associated fit to a DS model (black line) used to infer the phase after optical pumping. (b) Dependence of magnetic field, calculated using Eq. (5.2), on the readout power for a delay time of $t_\Delta = 0.63 \text{ ms}$ using the DS model to extract the signal phase ϕ_0 . The DC component has been subtracted from the data.

where $\Delta\phi$ is the phase difference between the pumping induced spin angle Φ_0 and the initial phase ϕ_0 measured at the moment the readout pulse is applied. Tracking the value of ϕ_0 thus serves as an indirect method of inferring the external field strength. We have seen already that synchronously driving the atomic ensemble ensures consistency in the degree of coherence generated; therefore, precise control of experimental parameters will be crucial in maintaining fixed operating conditions for this technique. There are noticeable similarities of this implementation to magnetometers that operate in free-running mode, in the sense that magnetic field variations are measured indirectly from the spin precession phase [101].

The spin angle Φ_0 generated by optical pumping is calculated by extrapolating the fitted DS model to the end of the pump stage as seen in Fig. 5.6(a). Figure 5.6(b) then shows the phase values ϕ_0 tracked during readout whilst simultaneously varying the probe power in subsequent pump-probe cycles. The DS model fit was used to calculate the signal phase ϕ_0 of each FID trace. Both data sets in Fig. 5.6 were acquired consecutively to ensure consistent operating conditions throughout the measurement. The converted magnetic field demonstrates a predominantly flat dependence with readout power; however, there does seem to be some systematics present especially at lower intensities that yield reduced SNRs. The RMS fluctuation was measured to be 73 pT

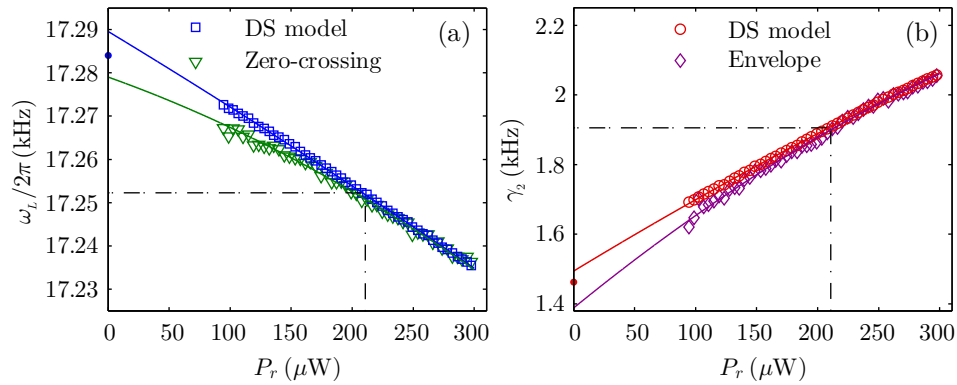


Figure 5.7: (a) Precession rates measured with frequency extraction based on ZCs (green) and the DS model fit (blue). (b) Damping rates measured from the DS fit (red) and the signal envelopes (purple). The solid lines in both plots are fits to an empirical second order polynomial model. The dots at zero-light power indicate the precession and damping rates measured from the reconstructed signal in Fig. 5.6(a). The measured estimators were extracted from the same FID traces utilised for the data presented in Fig. 5.6(b).

which is around twice the calculated error. The sensitivity to light shift is on the same order of magnitude to that experienced in a previous experiment adopting a specific frequency detuning as a means of cancelling the AC Stark effect (see Section 3.4.3); the RMS fluctuation was 43 pT in this case. One may argue that these results are a consequence of minimal light shift being present as we are considerably detuned from the $F = 4 \rightarrow F'$ transition. Figure 5.7(a) alleviates these concerns as it conveys the estimated precession rates from the same FID traces used to generate the data in Fig. 5.6(b), using alternative frequency extraction techniques. It can be seen that the light shift causes around a 10 nT linear decrease in the Larmor frequency over the same range of probe powers. The sign of the gradient is attributed to the laser frequency being blue-detuned with respect to the $F = 4 \rightarrow F'$ transition. The horizontal dashed line indicates the precession rate that is actually detected during readout at the probe power used to reconstruct the signal shown in Fig. 5.6(a), and is based on an empirical second order polynomial fit. It can be seen that extrapolating to zero-light power with this phenomenological model provides different results for both frequency estimation methods which is a clear symptom of the protruding systematics that incur when extracting the precession rate. The blue data point shown at zero-light power is equiva-

lent to the frequency measured from the reconstructed precession signal in Fig. 5.6(a), and it is clear to see that there is reasonable agreement with the empirical polynomial fits. Figure 5.6(b) exhibits the extensive power broadening that occurs during readout, contingent on the strength of light-atom interaction. The damping rates were extracted by first applying the DS fit model as in previous cases, and also using the exponential envelopes (see Section 3.3.7) in the FID trace as a means of comparison. This was in attempt to try and decouple other free-parameters from influencing the damping estimation. It can be seen that both techniques provide similar results but tend to diverge at low probe intensities when SNR is considerably reduced. The relaxation rate measured from the reconstructed precession signal in Fig. 5.6(a) is symbolised by the red data point at zero-light power. As with the precession rate, it can be noticed that the value lies between the damping rates at zero-light power, calculated from the empirical second order polynomial fits for each damping estimation method.

5.1.4 Sensitivity analysis

We have discussed in detail the possibility of suppressing systematic errors that are induced by the light-atom interaction during readout by adopting the PITD detection mode. This technique relies on the optically pumped spin state being well-known and consistent. The phase information at the end of the pump stage is then utilised to infer the magnetic field strength based on the phase of the FID signal at the instant the readout pulse was applied, as seen in Eq. (5.2). As is the case with any estimator, the best precision that we can calculate the initial phase during readout is governed by the CRLB condition (see Appendix C.2) given by,

$$\sigma_{\phi_0}^2 \geq \frac{8}{(A/\sigma)^2 N} C_1, \quad (5.3)$$

where A/σ is the SNR, N is the number of samples, and C_1 is a corrective factor accounting for signal damping defined as,

$$C_1 = \frac{N(1-z^2)}{4} \left[1 + \frac{(1-z^{2N})z^2(z^2+z^{2N}) - 2N(1-z^2)z^2z^{2N}}{-N^2z^{2N}(1-z^2)^2 + z^2(1-z^{2N})^2} \right]. \quad (5.4)$$

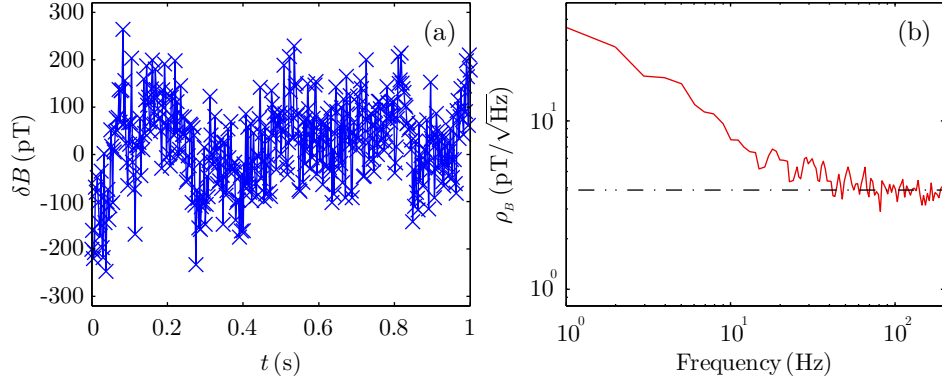


Figure 5.8: (a) Magnetic field fluctuations measured by a FID magnetometer implementing detection based on PITD, using a readout intensity of $I_r \simeq 80 \mu\text{W}/\text{mm}^2$ and the delay time $t_\Delta = 0.63$ ms. The initial phase of subsequent FID traces were estimated during readout and converted to a field measurement using Eq. (5.2). (b) Associated noise spectra calculated by applying the DFT on the magnetic field time series. The dashed line symbolises the noise floor, calculated to be $3.8 \text{ pT}/\sqrt{\text{Hz}}$.

Assuming the initial spin state Φ_0 is well-defined, Eq. (5.2) can be used to convert this phase error into an estimation of the magnetic field noise in the following way,

$$\sigma_B^2 = \frac{2C_1}{\pi^2 \gamma^2 t_\Delta^2 (A/\sigma)^2 N}. \quad (5.5)$$

If the noise is white then the associated noise density can be inferred from Eq. (3.18) by taking into account the bandwidth, dictated by the total measurement time $T = T_p + T_r + t_\Delta$ where T_p and T_r are the pump and readout durations, respectively. This is of course assuming a flat noise spectrum and does not consider any $1/f$ technical noise that may be present in the system.

Figure 5.8 depicts a time series tracking the magnetic field fluctuations over a period of 1 s. This information was gathered by extracting the initial phase from each FID trace in the signal train, estimated by fitting a DS model, and converting to magnetic field using Eq. (5.2). The spin state after optical pumping was determined from previous experiments that utilised identical operating conditions⁵, aside from the repetition rate that was set to $f_d = 400$ Hz to increase the sensor bandwidth. A DFT was applied

⁵A precession signal was fully reconstructed by varying the delay time and tracking the initial phase during readout. The pumping induced spin phase was then calculated using extrapolation.

to assess the distribution of noise over the detection bandwidth. The noise floor in the upper frequency range was measured to be $3.8 \text{ pT}/\sqrt{\text{Hz}}$. Also, calculation of the CRLB condition using Eq. (5.5) yielded a noise density of $1.9 \text{ pT}/\sqrt{\text{Hz}}$ based on the estimated SNR and damping rate. This is competitive with the previously adopted detection mode and has the added advantage of being a more accurate measurement technique. Distinct low frequency drifts are present which is to be expected when considering previously gained noise spectra. This type of noise is often technical and can arise from numerous sources, such as variations in the light polarisation primarily attributed to the temperature dependent static birefringence of the EOM. The noise could also be caused by magnetic field transients that penetrate through the three layer μ -metal shield. However, this is not probable as there is no evidence of line noise that was previously determined to have an amplitude exceeding 200 nT at 50 Hz when placed in the same location as the shield⁶ (see Section 4.4). The probe intensity was kept at $80 \mu\text{W}/\text{mm}^2$ although further enhancement in the bandwidth is achievable by elevating the laser power to broaden the magnetic resonance, thereby reducing the required probe duration. The exact nature of how this affects the devices sensitivity will be determined by the enhancement in SNR and degradation in the spin relaxation rate, which both impact the precision of extracting the phase information from a FID trace. A delay time of $t_\Delta = 0.712 \text{ ms}$ was adopted in this analysis which includes $85 \mu\text{s}$ of truncated data that is discarded at the start of the signal to improve the fitting quality. This delay time was chosen based on some preliminary experiments that included a coarse sensitivity optimisation at the chosen probe power. A full investigation on the optimum precision achievable from this technique has still to be performed and would require exploring the coupled parameter space that includes readout power and delay time. There is the obvious inverse relationship between t_Δ and field sensitivity as denoted in Eq. (5.5). However, spin depolarisation during the dark phase will influence the SNR achieved at different delay time intervals. The dependence on t_Δ is analogous to that experienced by coherent population trapping based atomic clocks implementing Ramsey interrogation techniques. In these cases, the clock stability is inversely proportional to

⁶The shielding factor will not exceed 10^3 for the 3-layer μ -metal shield used in these experiments

the time between the state preparation and detection pulses as this dictates the width of the Ramsey fringes with a FWHM equivalent to $1/2 t_{\Delta}$ [102,103].

5.2 Measurement of Intrinsic Spin Lifetime

We have already seen that PITD is an effective method of suppressing the operational systematics induced by the light-atom interaction. In this section, we employ this technique to detect the decoherence mechanisms intrinsic to the sensor head under different experimental conditions. The results are compared to another commonly adopted method based on extrapolating to zero-light power [68]. The experimental arrangement used throughout these coherence rate measurements is identical to that utilised in the previous section. The narrow band laser light was manually red-detuned relative to the collisionally shifted $F = 4 \rightarrow F' = 3$ transition for each cell characterisation to avoid spin-exchange suppression that may occur due to light narrowing (see Section 2.4.2). In each case the detuning was optimised based on the SNR at the lowest cell temperature analysed (50°C), hence varied depending on each cell tested as their spectroscopic properties differ. This did not coincide with the peak of the absorption spectrum as dispersive detection based on polarimetry was employed. The laser frequency prior to, and after, each cell characterisation was measured precisely using a wavelength meter (Bristol) and its stability monitored by observing the voltage level in an auxiliary spectroscopy arrangement consisting of a Cs reference cell. As the utilised laser frequency does not reside on the absorption peak, variations in light intensity can be easily misinterpreted as frequency drifts. No active locking of the laser frequency was performed as the output was found to be sufficiently stable over long time periods, although any sizeable drifts would be corrected using the wavelength meter⁷.

5.2.1 Ground state coherence measurement techniques

The intrinsic decoherence rate γ_{20} of the ground state manifold was first deduced by extrapolating to zero-light power. The measurement process is analogous to the AC

⁷Constant monitoring of the laser frequency with the wavelength meter was not possible as the device was only available for short time periods.

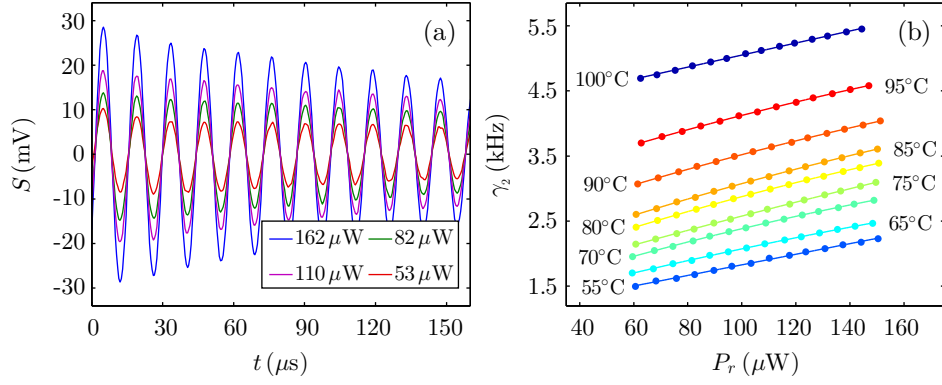


Figure 5.9: Measurement of the intrinsic relaxation rates by extrapolating to zero-light power. The nitrogen gas pressure in this particular vapour cell was estimated to be 1080 Torr based on the optical spectrum. (a) First 160 μs portion for a subset of four FID traces in a signal train acquired at different probe powers in a magnetic field of $20 \mu\text{T}$. (b) Power broadening behaviour measured at various cell temperatures by extracting the damping rates (dots) from each FID trace in the signal train. The data were fit to an empirical second order polynomial (solid line) to extract γ_{20} . Spin-exchange collisions are the primary contributing factor driving the temperature dependence in this configuration.

Stark shift characterisation performed in Section 3.4.3. This involves incrementally scanning a range of probe powers, as seen in Fig. 5.9(b) for the high pressure cell at various temperatures. The beam area was kept consistent with previous experiments at around 2.5 mm^2 , measured using a beam profiler and extracting the $1/e^2$ widths. The magnetic field was resonantly tuned to achieve the maximum FID amplitude at the chosen synchronous modulation frequency of 70 kHz, resulting in a bias field of around $20 \mu\text{T}$. This was applied approximately transverse to the beam propagation axis using a set of Helmholtz coils, although no active alignment of the magnetic field axis was performed during these experiments. Optical rotation in the linear probe was detected using a polarimeter, and the ensuing FID signal trains were acquired on an oscilloscope over 5 s measurement periods at a sample rate of 2 MS/s. The repetition rate was set such that the atomic population could rethermalise prior to the next pumping cycle to avoid memory effects in the spin polarisation. A digital high-pass Butterworth filter with a cutoff frequency of 10 kHz was applied to the signal train post-acquisition to eliminate DC offsets and slowly varying terms, thus vastly improving the

fitting quality. The reduced chi-squared statistic for most of the DS model fits applied in these experiments were close to $X_r^2 = 1$ indicating that the theoretical model is a good representation of the observed FID data. This appears to be a recurring feature when adequately frequency detuned away from the $F = 3 \rightarrow F' = 3$ transition that potentially distorts what should be a typical Lorentzian magnetic resonance lineshape. A selection of post-filtered FID traces observed at different readout powers are shown in Fig. 5.9(a). Each FID trace in the signal train is processed using a fitting routine to extract the damping rate, equivalent to the decoherence experienced by the Cs atoms. The estimated relaxation rates at different probe powers and cell temperatures have been formalised in Fig. 5.9(b) providing insight into the different mechanisms effecting decoherence in the atomic ensemble. For example, the probe power dependence of the transverse relaxation rates is a consequence of residual optical pumping effects during readout that broaden the magnetic resonance⁸. The temperature dependence is mainly influenced by spin-exchange collisions that increase in frequency as the vapour cell is heated. Other depolarising contributions such as wall and buffer gas collisions will also rise at elevated temperatures; however, spin-exchange tends to be the dominant mechanism in these thermal vapour cells. The damping rate can vary nonlinearly at higher probe powers, attributed to the creation of spin alignment in the atomic ensemble during readout. In instances such as these γ_{20} is inferred from a phenomenological second order polynomial fit that is extrapolated to zero-light power as demonstrated in [68], by Scholtes *et. al.*

An alternative technique is also presented, predicated on Ramsey-style detection, that monitors the evolving ground state manifold in-the-dark. The proposed method was discussed thoroughly in the previous section, although emphasis was placed on improving the accuracy of the sensor by suppressing AC Stark shifts as opposed to eliminating power broadening effects. The experimental procedure involves reducing the light intensity to approximately zero for a delay time t_Δ after optically pumping the sample into a highly polarised state. Subsequently applying a readout pulse enables one

⁸In other words, the polarised spins are oriented along the beam propagation direction during readout thereby destroying coherence as they precess in the ambient magnetic field.

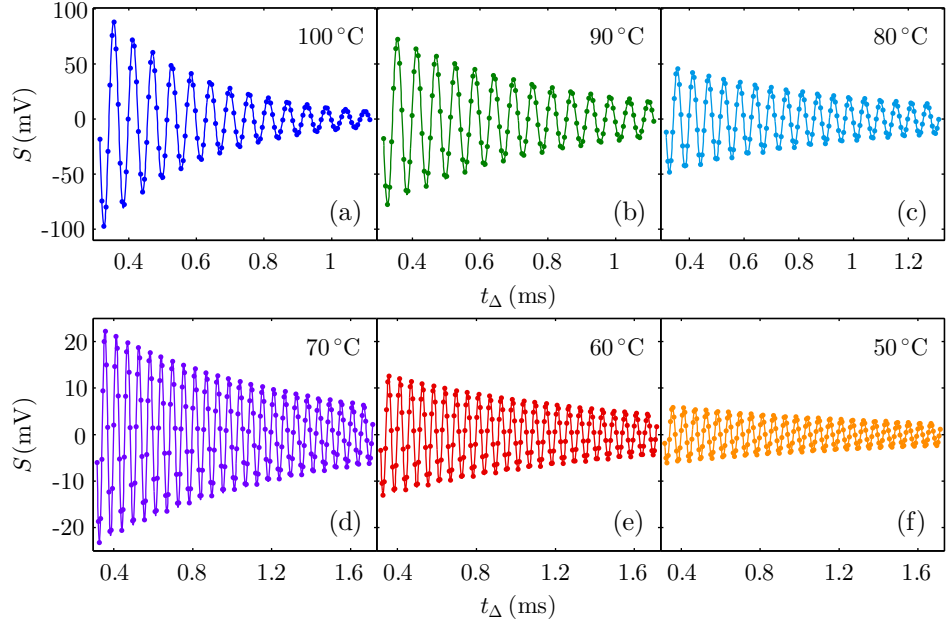


Figure 5.10: Precession signals (dots) acquired in-the-dark using Ramsey-style detection, and associated fit to a DS model (line). A readout power of $200 \mu\text{W}$ was implemented and the magnetic field was set to around $5 \mu\text{T}$. Various temperatures were analysed ranging from $50\text{-}100 \text{ }^{\circ}\text{C}$ as seen in (a)-(f) respectively, in a cell with a buffer gas pressure estimated to be 210 Torr.

to observe the spin phase at the instant the light was switched back on, by extrapolating to the start of a DS model fit. Varying t_{Δ} thus serves as a method of tracing the spin precession in a manner that is not influenced by the light-atom interaction during readout, with the exponential envelope of the ensuing damped oscillation yielding a measurement of γ_{20} . This process is shown in Fig. 5.10 for measurements performed at various cell temperatures ranging from $50\text{-}100 \text{ }^{\circ}\text{C}$. Similar to the results in Fig. 5.9(b), the spin coherence decays more rapidly as the cell temperature rises, primarily due to the elevated frequency of spin-exchange collisions at higher atomic densities. This also significantly improves the signal amplitude although saturation is evident at higher temperatures when the vapour becomes optically thick⁹.

⁹A medium is deemed optically thick if on average a photon cannot propagate through the sample without being absorbed.

5.2.2 Buffer gas pressure estimation

An assembly of seven vapour cells of similar geometry, based on 1.5 mm thick silicon wafers (see Section 2.2.1), were investigated. The cells are sourced from a series of wafers that were fabricated independently from one another thus there are some fluctuations in the cavity dimensions depending on the mask applied during photolithography in each iteration. Depolarising wall collisions are predominantly influenced by the smallest dimension, in this case defined by the thickness which was consistent for each cell tested. Wet etching is used to form the cell cavities, that are subsequently filled with a caesium azide (CsN_3) solution. The glass surface is anodically bonded in vacuum to the silicon wafer, after which UV photolysis decomposes the gaseous nitrogen from the pure caesium metal. The nitrogen gas pressure is elevated by increasing the light dose, although saturation is eventually reached after long exposure thereby restrict-

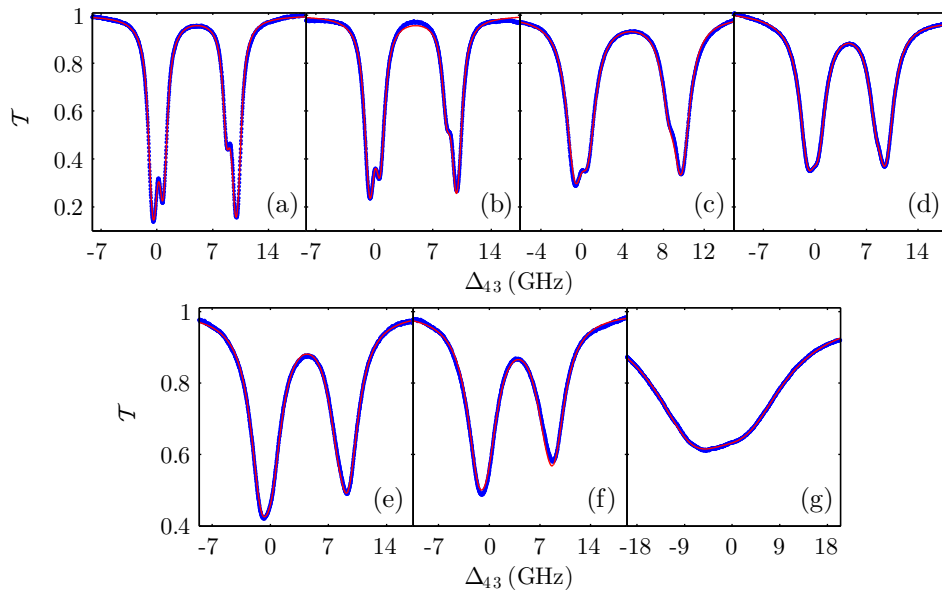


Figure 5.11: Experimentally acquired optical spectra (blue) and corresponding fit to a Voigt profile (red) for a selection of microfabricated Cs vapour cells containing different quantities of N_2 at a temperature of 85°C . The frequency axis is measured with respect to the $F = 4 \rightarrow F' = 3$ transition of a Cs reference cell. The buffer gas pressures are estimated from the broadening and shift values calculated from each nonlinear fit, and were measured to be 54.9 Torr, 66.5 Torr, 89.4 Torr, 117 Torr, 155 Torr, 210 Torr, and 1080 Torr for the spectra shown in (a)-(g), respectively.

ing the maximum available N_2 content when bonding in vacuum. Many MEMS cells contain enough buffer gas to fully merge all resonant transitions resulting in a single homogeneously broadened absorption peak as seen in Fig. 5.11(g). This requires exceeding atmospheric pressure and bonding in a nitrogen atmosphere in a process known as “backfilling”. This method enables the user to offset the buffer gas pressure in a controllable manner.

The quantity of N_2 present is determined from the optical spectrum (see Section 2.2.3) by measuring the collisionally induced broadening and shift imposed on the resonant transitions. Resonance spectra for each test cell at a temperature of 85°C is shown in Fig. 5.11 along with the corresponding fit to a Voigt profile. These were used to extract the parameters relevant in the pressure estimation, composed of a weighted average of the independent calculations measured from both the broadening and shift¹⁰. To avoid power broadening of the optical resonances, the laser power was reduced to around $10\ \mu\text{W}$ and the waveform was averaged on the oscilloscope to improve SNR. This selection of vapour cells was chosen based on their spectroscopic properties to yield an adequate range of buffer gas pressures for our analysis. Unfortunately, the range between 210-1080 Torr could not be explored due to unavailability of vapour cells fabricated at these pressures. The analysis of the optical spectrum from any given vapour cell is extremely useful in inferring its limitations as a magnetic sensor. This will be evident in the forthcoming sections that investigate the spin relaxation characteristics inherent to the vapour cell, in the absence of operational systematics that broaden the magnetic resonance.

5.2.3 Transverse relaxation rate measurements

The intrinsic damping rates γ_{20} extracted by extrapolating to zero-light power and adopting PITD are shown in Figs. 5.12(a) and 5.12(b), respectively. The measurements were performed in increments of 5°C over the temperature range $50\text{-}100^\circ\text{C}$ for each of the characterised cells with N_2 pressures extending from 55-1080 Torr. The data gathered from each vapour cell was compared to the relaxation rate model given

¹⁰The nitrogen number density can be inferred from the buffer gas pressure using the ideal gas law.

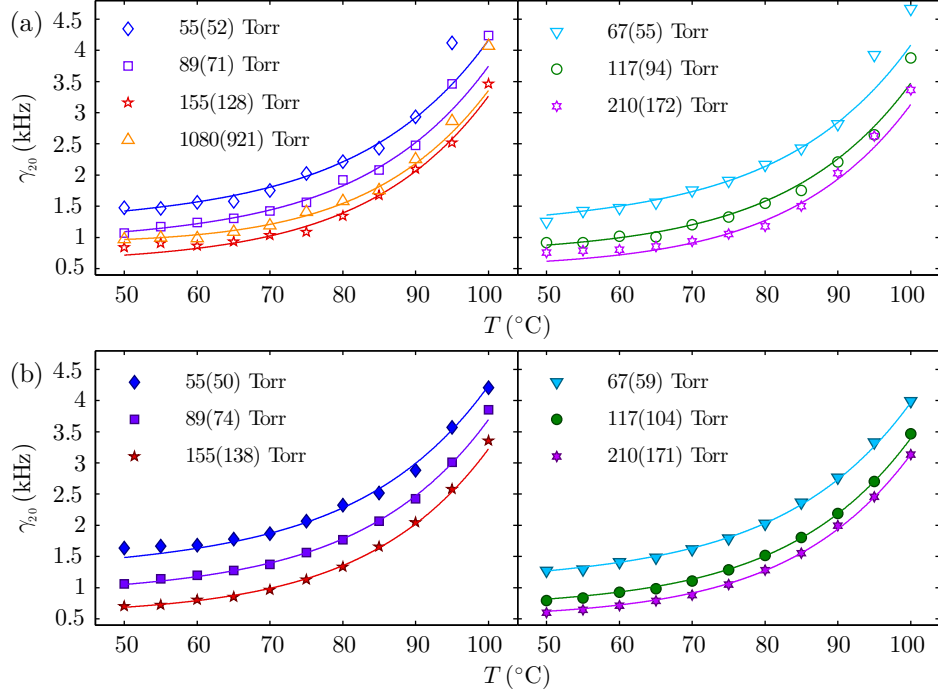


Figure 5.12: Intrinsic transverse decoherence rate as a function of temperature for various vapour cells of similar geometries and different N_2 number densities, measured by (a) extrapolating to zero-light power and (b) PITD using Ramsey-style detection. The buffer gas pressure estimation for each cell is noted in the legend. The first measurement was gained using spectroscopy whereas the value inside the brackets was determined by fitting the relaxation rate model provided in Eq. (2.56), represented by the solid lines, and leaving the N_2 gas pressure as a free parameter. A cylindrical cell geometry was assumed with the radius set equal to the thickness of the vapour cell at 1.5 mm. Statistical error bars are smaller than the marker sizes.

in Eq. (2.56) using a nonlinear fit with the buffer gas pressure left as a free parameter. The legend denotes the estimated N_2 gas pressures measured from the previously acquired optical spectra in Fig. 5.11 for each cell, and using the model in Eq. (2.56) as represented by the bracketed pressure values. Unfortunately, technical issues with the laser source limited the frequency tuning range at the time of testing hence the high-pressure cell, that experiences a vastly larger optical broadening and shift than the other cells characterised, was not tested using the PITD technique. The basis for comparison of estimating the N_2 content within each cell is predicated on the analysis of its spectral properties which is susceptible to potential systematics. The complicated

nature of the Voigt profile and corresponding nonlinear fit can sometimes hinder reproducibility of these measurements. For example striking different regions of the vapour cell can cause significant deviations in the fitted broadening or shift, as localised azide residual blocks the beam path thereby slightly altering the appearance of the resonance structure. The high pressure vapour cell, with a spectrum consisting of a single merged resonance, was particularly prone to variations due to the limited frequency scanning range of the laser.

Principally, there is clear divergence between the buffer gas predictions based on the relaxation rate model and the results gained from the optical spectra presented in Fig. 5.11. There are numerous plausible explanations for these discrepancies, including in the Cs spectroscopy measurements themselves as mentioned previously. The relaxation rate model is reliant on a list of experimentally acquired constants describing various interaction properties of Cs in the presence of N₂ gas [1]. These are all subject to considerable measurement uncertainties that potentially skew the theoretical model in different ways leading to errors of around 10-20% depending on the experimental parameters. The model in Eq. (2.56) should only be considered as a coarse estimation of the observed behaviour especially as a cylindrical cell cavity was assumed to yield an analytical solution for the geometrical dependence. It should be noted that the standard tolerance in the thickness of silicon wafers during fabrication is $\pm 25 \mu\text{m}$ which would account for fluctuations but not the systematic effects observed here. The model predictions are fairly sensitive to such geometrical variations especially for these miniaturised cells. It is thus no surprise that the relaxation rate model systematically underestimates the observed pressure by varying amounts between 6-25% and 9-19% in Figs. 5.12(a) and 5.12(b) respectively, with respect to the measurements based on the optical spectra. Even with the obvious systematics present, it can be seen that the general trends in Figs. 5.12(a) and 5.12(b) are indicative of the expected model behaviour. In particular, the coherence measurements based on PITD were particularly impressive and experienced less fluctuation compared to the technique that utilises extrapolation to zero-light power. The strong nonlinear dependence when scanning probe power in some instances caused the process of extrapolating to zero-light power to become more

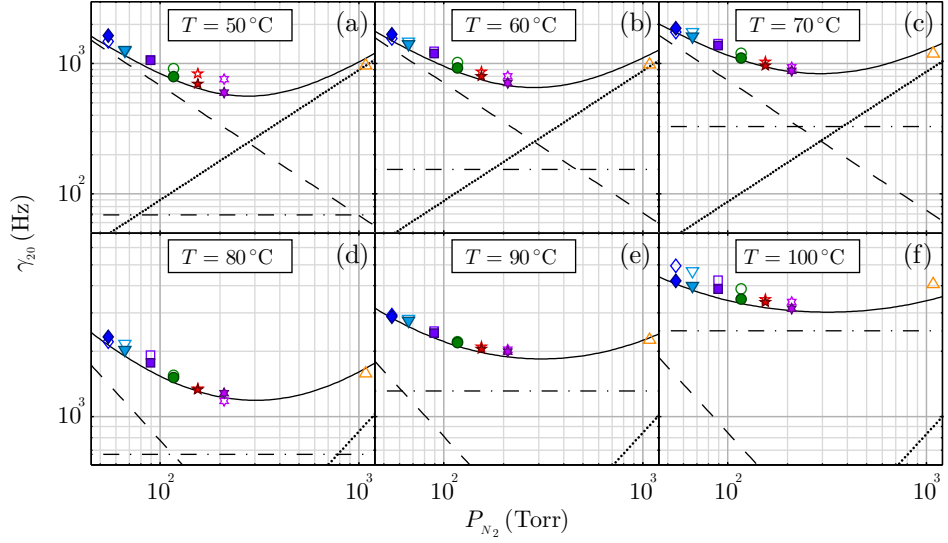


Figure 5.13: Intrinsic transverse decoherence rate as a function of pressure at various vapour cell temperatures, measured by extrapolating to zero-light power (open symbols) and PITD (full symbols). The pressures were determined from the optical spectra analysed for each cell. The black lines symbolise the model predictions for the wall (dashed), buffer gas (dotted), and spin-exchange (dot-dashed) contributions to spin relaxation. The solid black lines represents the total transverse spin relaxation accumulated from all contributions, which should resemble the measured data. A cylindrical cell geometry was assumed with the radius set equal to the thickness of the vapour cell at 1.5 mm. Statistical error bars are smaller than the marker sizes.

delicate and highly susceptible to fluctuation when considering different ranges. For example, the reduced SNR's achieved at low temperatures and probe powers could considerably influence the final estimation of γ_{20} . Contrastingly, the readout power for the PITD measurements was kept constant at around $200 \mu\text{W}$ thus the SNR was far superior in most cases, even at the lowest analysed temperature of 50°C as seen in Fig. 5.10(f). The Cs vapour becomes optically thick at high atomic densities resulting in large deviations from the anticipated behaviour at elevated temperatures as seen in Fig. 5.12(a). PITD measurements should be independent of probe power hence demonstrate a far lower sensitivity to this effect, evidenced in Fig. 5.12(b).

Figure 5.13 shows the relaxation rate data measured from each vapour cell as a function of N_2 gas pressure at a series of different temperatures for both measurement techniques discussed previously. The data is compared to the intrinsic relaxation rate

model provided in Eq. (2.56) without any free parameters. Each mechanism contributing to spin decoherence is represented separately by a series of dashed (or dotted) lines in each plot, as well as the accumulated transverse lifetime denoted by the solid line. It can be seen that the spin-exchange contribution is dominant at higher temperatures, and is negligible at lower temperatures in which case wall or buffer gas collisions become the primary decoherence mechanism depending on the gas pressure. Both measurement techniques yield similar results at intermediate temperatures which provides supplementary evidence that PITD is indeed suppressing systematics induced by the light-atom interaction, and further verifies the validity of the acquired relaxation rate measurements. The data agree reasonably well with the theoretical predictions especially when implementing the PITD method which follows the curves well at all investigated temperatures. Contrastingly, extrapolating to zero-light power performs inconsistently at both low and high temperatures as evidenced in Figs. 5.13(a) and 5.13(f), respectively. Thus, it is fair to surmise based on the quality of both data sets that PITD is a more robust way of inferring the intrinsic lifetime of the ground state manifold. Inspecting the results gained at 50 °C, one can confirm based on the theoretical predictions that the minimum intrinsic lifetime occurs at a buffer gas pressure of 276 Torr for this cell geometry. The pressure at which this minimum occurs is only slightly temperature dependent with the maximum calculated to be 318 Torr at 100 °C.

Chapter 6

Conclusion and Outlook

To summarise, microfabricated Cs vapour cell technology was utilised as the primary sensing element in a series of magnetometry measurements. Both AM and FM were adopted independently in a FID setting to monitor the free Larmor precession of the atomic spins in the time domain. We seen that actively driving this precession using synchronous modulation provided consistent results even at higher bias fields where single-pulse optical pumping becomes increasingly inefficient. We used a balanced polarimeter to observe optical rotation, as opposed to absorption-based detection, resulting in significant noise reduction and signal enhancement attributed to the differential measurement. The best sensitivity performance of both modulation techniques was investigated producing sensitivity spectra with noise floors of $3.4 \text{ pT}/\sqrt{\text{Hz}}$ and $15.6 \text{ pT}/\sqrt{\text{Hz}}$ using AM and FM, respectively. This correlated closely with the CRLB noise densities calculated based on the SNR and damping rate achieved using each technique. The less efficient optical pumping in the FM regime translates into a smaller SNR that directly impacts the sensor precision as described in Eq. (3.17). There is still potential for optimisation of the FID magnetometer particularly when implementing FM. For example, an extensive characterisation of the ideal spectroscopic properties of the sensor head was performed to ascertain the optimal buffer gas pressure that maximises the spin lifetime based on the MEMS cell dimensions. Also, acquiring and processing data with FPGAs could lift the sampling rate restriction that limits the precision of the model independent ZC frequency extraction technique. There are additional

opportunities for enhancement in how the magnetometer is driven; for example, the input polarisation, beam width, and frequency detuning could all be further optimised. Additionally, the gain characteristics of the TIA in the balanced polarimeter should be tailored to the optical power output of the VCSEL and precession frequency, which could provide improvements in SNR. VCSEL technology is still a field of considerable interest giving rise to constant improvements in the maximum output power possible. This could be another avenue for improving the FM system that has the potential to rival that of the AM configuration, with a considerably higher degree of scalability. Sinusoidal modulation was used as preliminary experiments displayed a larger SNR; however, with the correct modulation parameters a square waveform could increase the optical pumping efficiency [13].

A potential packaged device will contain a limited number of components, including a VCSEL, focusing lens, quarter-wave plate, Cs cell, PBS, and two photodiodes. Thicker Cs cells will increase the spin-coherence lifetime and reduce the required cell temperature; this will improve the sensitivity performance and potentially power consumption. PBSs smaller than $2 \times 2 \times 2 \text{ mm}^3$ are possible, which is ideal for the beam sizes typically considered here if a focussing lens is applied. The photodiodes will likely be attached directly to each channel of the PBS and would be of similar dimensions. The smallest component is the VCSEL in a die format; machine placement of these devices is difficult especially as a specific orientation, with respect to the fast axis of the quarter-wave plate, is required to adequately balance the polarimeter detection system. Heater tracks can be placed directly on the Cs cells with a particular pattern that eradicates spurious magnetic fields from applied currents. RF heating with a frequency considerably above the Larmor precession frequency and off-resonant laser heating are also possible alternatives. A straightforward control system could be implemented on FPGA for data acquisition, real-time processing, and to control the modulation input to the VCSEL; a feedback loop and sweep will maximise the FID amplitude in the synchronous regime. Single-pulse optical pumping will provide an estimate of the required modulation frequency and can also be used as the primary modulation technique at low bias fields. If the experimental parameters are fully optimised, a cm-scale packaged

device with pT-level sensitivities should be possible in the FM implementation.

Waveform tracking of time-varying magnetic signals was also performed using the FID mechanism, demonstrating excellent reconstruction of sinusoidal oscillations. The impressive sensitivity of the magnetometer was further epitomized by reproducing a 100 pT modulation showing that this novel approach to signal reconstruction can provide reliable and accurate detection of weak oscillations in Earth's field conditions. There are clear and obvious limitations in extracting broad spectral information from a periodic measurement; however, it was shown that the FID magnetometer can detect a superposition of discrete frequencies as long as they reside within the Nyquist limited bandwidth. This was achieved experimentally in an unshielded environment in which multiple harmonics that constitute line noise were detected. The bandwidth of the sensor can be extended through signal truncation which also enhances the precision of frequency extraction in accordance with the minimised CRLB condition. Additional improvements in sensor bandwidth are gained by raising the transverse relaxation rate through mechanisms such as spin-exchange collisions or power broadening; however, this will also degrade the sensitivity. A high amplitude field oscillation was applied to demonstrate the FM sidebands that can appear in FID spectrum; the corresponding behaviour was modelled using Bessel functions of the first kind. The design simplicity, scalability and all-optical nature of this OPM is attractive for numerous applications, including MCG that requires a flat response in the low frequency range (typically < 100 Hz). The FID technique also benefits from minimal cross-talk due to the absence of RF coils which is beneficial in many applications that demand magnetic source localisation with sensor networks.

It was demonstrated that one can suppress both the light shift and power broadening induced by the light-atom interaction using PITD detection, to vastly improve the accuracy of the magnetometer. The method is based on measuring the spin precession in-the-dark by switching the light intensity to zero for a set delay time after optical pumping, and subsequently monitoring the signal phase during readout. The technique's low sensitivity to varying light intensities was shown by monitoring the signal phase, and reconstructing precession signals, at different probe powers. System-

atic errors in extracting the Larmor rate from each FID signal do still exist, although it is not unreasonable to assume that these systematics could be eradicated so that the device accuracy is level with its own precision. The sensitivity of this detection mode was found to be competitive with previous implementations at $3.8 \text{ pT}/\sqrt{\text{Hz}}$ with minimal optimisation. The technique was also adopted for ground state coherence measurements that aided in measuring the intrinsic spin relaxation properties of the sensor head. This characterisation is extremely useful in determining the target buffer gas pressure when fabricating the vapour cells, to extend the spin lifetime for optimal sensitivity performance. It was discovered that a N_2 pressure approaching 300 Torr is ideal for the 1.5 mm thick vapour cells utilised throughout this work at an operational temperature of 85°C . Pressures exceeding an atmosphere merge even the ground state hyperfine resonances such that the optical spectrum comprises a single peak which is extremely useful in simplifying the procedure of locking on to the absorption line. These vapour cells also perform well as a magnetometer as the relaxation rates are fairly low, especially if one can implement light narrowing to suppress spin-exchange collisions which should be easier with the increased spectral overlap.

Appendices

Appendix A: Alkali-metal properties

A.1 Alkali number density

The saturated number density \mathcal{N} for an alkali vapour can be estimated from the relation [1],

$$\mathcal{N} = \frac{1}{T} 10^{21.866 + A - B/T} \quad (\text{A.1.1})$$

where A and B are density parameters that depend on the atomic species and vapour phase, and T is the sample temperature in Kelvin. As provided in Ref [104], the density parameters for Cs are given as: $A = 4.711$ and $B = 3999$ in the solid phase; and $A = 4.165$ and $B = 3830$ in the liquid phase. It is also important to note that Cs requires less heating than other atomic species, such as Rb, to reach equivalent vapour pressures and has a lower melting point at $T_m = 28.44^\circ\text{C}$ [61].

Appendix B: Atomic theory

B.1 Reduced dipole matrix element

The strength of an interaction coupling near-resonant light to an atom is characterised by the dipole matrix element in the following way [39],

$$C_{FF'}^2 d^2 = \sum_{m_F, m'_F} |\langle F m_F | d_q | F' m'_F \rangle|^2, \quad (\text{B.1.1})$$

where $\langle F m_F | d_q | F' m'_F \rangle$ denotes the matrix element describing the transition between the hyperfine sublevels, $|F m_F\rangle$ and $|F' m'_F\rangle$ with a summation performed over all m_F Zeeman states [40]. We can factor out the angular dependence, m_F , using the Wigner-Eckhart theorem allowing the dipole matrix element to be written in terms of the Wigner 3- j symbol and reduced matrix element $\langle F || \hat{d} || F' \rangle$ as follows [39],

$$\langle F m_F | d_q | F' m'_F \rangle = \langle F || \hat{d} || F' \rangle (-1)^{F'+m_F-1} \sqrt{2F+1} \begin{pmatrix} F' & 1 & F \\ m'_F & q & -m_F \end{pmatrix} \quad (\text{B.1.2})$$

where d_q is the component of the dipole operator \hat{d} described in the spherical basis, and q is the integer change in m_F during the transition (for example $q = 0$ when using linearly polarised light) [44]. Equivalently one can express Eq. (B.1.2) as a product of the reduced matrix element and Clebsch-Gordan coefficient. We can further reduce the matrix element by factoring out the F dependence using the Wigner 6- j symbol [39],

$$\langle F || \hat{d} || F' \rangle = \langle J || \hat{d} || J' \rangle (-1)^{F'+J+1+I} \sqrt{(2F'+1)(2J+1)} \begin{Bmatrix} J & J' & 1 \\ F' & F & I \end{Bmatrix}. \quad (\text{B.1.3})$$

Repeating this procedure once more then $\langle J || \hat{d} || J' \rangle$ can be reduced to,

$$\langle J || \hat{d} || J' \rangle = \langle L || \hat{d} || L' \rangle (-1)^{J'+L+1+S} \sqrt{(2J'+1)(2L+1)} \begin{Bmatrix} L & L' & 1 \\ J' & J & S \end{Bmatrix}, \quad (\text{B.1.4})$$

where we define $d = \langle L || \hat{d} || L' \rangle$. The reduced matrix element $\langle J || \hat{d} || J' \rangle$ in Eq. (B.1.4) can be calculated using the decay rate of the atomic transition [41],

$$\Gamma_0 = \frac{k^3}{3\pi\epsilon_0\hbar} \frac{2J+1}{2J'+1} |\langle J || \hat{d} || J' \rangle|^2. \quad (\text{B.1.5})$$

As Γ_0 is a known quantity, this enables a determination of the reduced matrix element d . Thus, the quantity $C_{FF'}$ can be calculated simply from the combination of Wigner 3- j and 6- j symbols and their corresponding prefactors.

B.2 Numerical approximation of the Voigt profile

The Voigt profile is described by the convolution of the Lorentzian and Gaussian functions and can be expressed in the analytical form provided in Eq. (2.14). This is a difficult model to fit computationally hence the following numerical approximation can be made [47],

$$\mathcal{V}_a(\Delta_{FF'}) = c_l(d)\mathcal{L}(\Delta_{FF'}) + c_g(d)\mathcal{G}(\Delta_{FF'}) \quad (\text{B.2.1})$$

where we have introduced the dimensionless parameter $d = (\Gamma_l - \Gamma_g)/(\Gamma_l + \Gamma_g)$. The coefficients $c_l(d)$ and $c_g(d)$ are given by the relations [47],

$$c_l(d) = 0.68188 + 0.61293d - 0.1838d^2 - 0.11568d^3, \quad (\text{B.2.2})$$

$$c_g(d) = 0.3246 - 0.61825d + 0.17681d^2 + 0.11568d^3 \quad (\text{B.2.3})$$

The width of the Voigt profile can be approximated to within 0.01% using the Olivero-Longbothum formula given by [48],

$$\Gamma_v = 0.5346 \Gamma_l + \sqrt{0.2166 \Gamma_l^2 + \Gamma_g^2} \quad (\text{B.2.4})$$

Appendix C: Signal processing

C.1 Signal Noise Estimation Algorithm

Consider a discrete signal S_n that is corrupted by Gaussian white noise ε_n with a behaviour modelled by the function f_n ,

$$S_n = f_n + \varepsilon_n \quad n = 0, \dots, N - 1 \quad (\text{C.1.1})$$

where N is the number of collected samples. The variance in the noise ε_n is defined in the following way,

$$\text{Var}(\varepsilon_n) = E[\varepsilon_n^2] - E[\varepsilon_n]^2 = E[\varepsilon_n^2] = \sigma^2, \quad (\text{C.1.2})$$

based on the assumption that $E[\varepsilon_n] = 0$ which is valid for noise that is normally distributed with zero mean. Applying the definition for the numerical derivative, $x_n^{(1)} = x_{n+1} - x_n$, it can be shown that second derivative of the noise ε_n is given by,

$$\varepsilon_n^{(2)} = \varepsilon_{n+2} + \varepsilon_n - 2\varepsilon_{n+1}, \quad (\text{C.1.3})$$

where $x_n^{(i)}$ denotes the i^{th} derivative of the function x_n . Using Eqs. (C.1.2) and (C.1.3), and exploiting the linearity of the expectation value the variance in the quantity $\varepsilon_n^{(2)}$ can be expressed as,

$$\text{Var}(\varepsilon_n^{(2)}) = E[\varepsilon_{n+2}^2] + E[\varepsilon_n^2] + 4E[\varepsilon_{n+1}^2] = 6\sigma^2. \quad (\text{C.1.4})$$

We can define the variance in the second derivative of the signal as,

$$\text{Var}(S_n^{(2)}) = \text{Var}(f_n^{(2)}) + \text{Var}(\varepsilon_n^{(2)}) + 2\text{Cov}(f_n^{(2)}\varepsilon_n^{(2)}). \quad (\text{C.1.5})$$

For high sampling rates in which the data points are closely spaced, the variance $\text{Var}(f_n^{(2)})$ and covariance $\text{Cov}(f_n^{(2)}\varepsilon_n^{(2)})$ are negligible; therefore, utilising Eqs. (C.1.4) and (C.1.5), one can calculate the noise variance σ^2 in the discrete signal S_n from its

second derivative using the expression [61],

$$\sigma^2 = \frac{\text{Var}(S_n^{(2)})}{6} = \frac{\text{Var}(S_{n+2} + S_n - 2S_{n+1})}{6}. \quad (\text{C.1.6})$$

C.2 Cramer-Rao Lower Bound

The Cramér-Rao lower bound (CRLB) condition establishes the highest precision of extracting a parameter from a signal based on a specified model [81–83]. This can be expressed in terms of the variances as listed below for the free-parameters of a damped sinusoid,

$$\sigma_A^2 \geq \sigma^2 Q_1(z, N), \quad (\text{C.2.1})$$

$$\sigma_{\phi_0}^2 \geq \frac{Q_1(z, N)}{(A/\sigma)^2}, \quad (\text{C.2.2})$$

$$\sigma_{\omega_L}^2 = \sigma_{\gamma_2}^2 \geq \frac{Q_2(z, N)}{(A/\sigma)^2}, \quad (\text{C.2.3})$$

with σ_A , σ_{ω_L} , σ_{ϕ_0} and σ_{γ_2} representing the error for the signal amplitude, frequency, initial phase and damping rate respectively, and σ is the noise level. The functions $Q_1(z, N)$ and $Q_2(z, N)$ are defined as [82],

$$Q_1 = 2(1 - z^2) \left[1 + \frac{(1 - z^{2N})z^2(z^2 + z^{2N}) - 2N(1 - z^2)z^2z^{2N}}{-N^2z^{2N}(1 - z^2)^2 + z^2(1 - z^{2N})^2} \right], \quad (\text{C.2.4})$$

$$Q_2 = \frac{2(1 - z^2)^3(1 - z^{2N})}{z^2(1 - z^{2N})^2 - N^2z^{2N}(1 - z^2)^2}, \quad (\text{C.2.5})$$

where $z = e^{-\gamma_2/f_s}$, with the relaxation and sampling rates denoted by γ_2 and f_s , respectively. In the limit of high sample rate these expressions can be simplified to,

$$Q_1(z, N \rightarrow \infty) = \frac{8}{N} C_1, \quad (\text{C.2.6})$$

$$Q_2(z, N \rightarrow \infty) = \frac{24}{N^3} C_2, \quad (\text{C.2.7})$$

Chapter 6. Conclusion and Outlook

The corrective factors C_1 and C_2 take into account the signal decay and approach unity in the limit of no damping.

Bibliography

- [1] S. J. Seltzer, “Developments in alkali-metal atomic magnetometry,” Ph.D. dissertation, Princeton University, 2008.
- [2] D. Budker and D. F. J. Kimball, *Optical magnetometry*. Cambridge University Press, 2013.
- [3] R. Wyllie, M. Kauer, G. Smetana, R. Wakai, and T. Walker, “Magnetocardiography with a modular spin-exchange relaxation-free atomic magnetometer array,” *Physics in Medicine & Biology*, vol. 57, no. 9, p. 2619, 2012.
- [4] H. Xia, A. Ben-Amar Baranga, D. Hoffman, and M. Romalis, “Magnetoencephalography with an atomic magnetometer,” *Applied Physics Letters*, vol. 89, no. 21, p. 211104, 2006.
- [5] Y. Zhang, Y. Tavrín, H.-J. Krause, H. Bousack, A. Braginski, U. Kalberkamp, U. Matzander, M. Burghoff, and L. Trahms, “Applications of high-temperature squids,” *Applied Superconductivity*, vol. 3, no. 7-10, pp. 367–381, 1995.
- [6] H. Becker, “From nanotesla to picotesla a new window for magnetic prospecting in archaeology,” *Archaeological Prospection*, vol. 2, no. 4, pp. 217–228, 1995.
- [7] M. Dougherty, K. Khurana, F. Neubauer, C. Russell, J. Saur, J. Leisner, and M. Burton, “Identification of a dynamic atmosphere at Enceladus with the Cassini magnetometer,” *Science*, vol. 311, no. 5766, pp. 1406–1409, 2006.

Bibliography

- [8] A. Youdin, D. Krause Jr, K. Jagannathan, L. Hunter, and S. Lamoreaux, “Limits on spin-mass couplings within the axion window,” *Physical Review Letters*, vol. 77, no. 11, p. 2170, 1996.
- [9] D. Budker and M. Romalis, “Optical magnetometry,” *Nature Physics*, vol. 3, no. 4, p. 227, 2007.
- [10] W. E. Bell and A. L. Bloom, “Optical detection of magnetic resonance in alkali metal vapor,” *Physical Review*, vol. 107, no. 6, p. 1559, 1957.
- [11] J. Kitching, S. Knappe, V. Shah, P. Schwindt, C. Griffith, R. Jiménez, J. Preusser, L.-A. Liew, and J. Moreland, “Microfabricated atomic magnetometers and applications,” in *Frequency Control Symposium, 2008 IEEE International*. IEEE, 2008, pp. 789–794.
- [12] S. Knappe, P. Schwindt, V. Gerginov, V. Shah, L. Liew, J. Moreland, H. Robinson, L. Hollberg, and J. Kitching, “Microfabricated atomic clocks and magnetometers,” *Journal of Optics A: Pure and Applied Optics*, vol. 8, no. 7, p. S318, 2006.
- [13] R. Jiménez-Martínez, W. C. Griffith, Y.-J. Wang, S. Knappe, J. Kitching, K. Smith, and M. D. Prouty, “Sensitivity comparison of M_x and frequency-modulated Bell–Bloom Cs magnetometers in a microfabricated cell,” *IEEE Transactions on Instrumentation and Measurement*, vol. 59, no. 2, pp. 372–378, 2010.
- [14] C. N. Johnson, P. Schwindt, and M. Weisend, “Multi-sensor magnetoencephalography with atomic magnetometers,” *Physics in Medicine & Biology*, vol. 58, no. 17, p. 6065, 2013.
- [15] J. Kitching, S. Knappe, P. D. Schwindt, V. Shah, L. Hollberg, L.-A. Liew, and J. Moreland, “Power dissipation in a vertically integrated chip-scale atomic clock,” in *Frequency Control Symposium and Exposition, 2004. Proceedings of the 2004 IEEE International*. IEEE, 2004, pp. 781–784.

Bibliography

- [16] R. Jiménez-Martínez, W. C. Griffith, S. Knappe, J. Kitching, and M. Prouty, “High-bandwidth optical magnetometer,” *Journal of the Optical Society of America B*, vol. 29, no. 12, pp. 3398–3403, 2012.
- [17] M. Auzinsh, D. Budker, D. Kimball, S. Rochester, J. Stalnaker, A. Sushkov, and V. Yashchuk, “Can a quantum nondemolition measurement improve the sensitivity of an atomic magnetometer?” *Physical Review Letters*, vol. 93, no. 17, p. 173002, 2004.
- [18] D. Budker, D. F. Kimball, D. Kimball, and D. P. DeMille, *Atomic physics: an exploration through problems and solutions*. Oxford University Press, USA, 2004.
- [19] M. Fleischhauer, A. Matsko, and M. Scully, “Quantum limit of optical magnetometry in the presence of AC Stark shifts,” *Physical Review A*, vol. 62, no. 1, p. 013808, 2000.
- [20] S. Groeger, G. Bison, J.-L. Schenker, R. Wynands, and A. Weis, “A high-sensitivity laser-pumped M_x magnetometer,” *The European Physical Journal D-Atomic, Molecular, Optical and Plasma Physics*, vol. 38, no. 2, pp. 239–247, 2006.
- [21] S. Seltzer and M. Romalis, “High-temperature alkali vapor cells with antirelaxation surface coatings,” *Journal of Applied Physics*, vol. 106, no. 11, p. 114905, 2009.
- [22] H. Dang, A. Maloof, and M. Romalis, “Ultrahigh sensitivity magnetic field and magnetization measurements with an atomic magnetometer,” *Applied Physics Letters*, vol. 97, no. 15, p. 151110, 2010.
- [23] J. Allred, R. Lyman, T. Kornack, and M. Romalis, “High-sensitivity atomic magnetometer unaffected by spin-exchange relaxation,” *Physical Review Letters*, vol. 89, no. 13, p. 130801, 2002.
- [24] D. Hunter, S. Piccolomo, J. Pritchard, N. Brockie, T. Dyer, and E. Riis, “Free-induction-decay magnetometer based on a microfabricated Cs vapor cell,” *Physical Review Applied*, vol. 10, p. 014002, 2018.

Bibliography

- [25] V. Gerginov, S. Krzyzewski, and S. Knappe, “Pulsed operation of a miniature scalar optically pumped magnetometer,” *Journal of the Optical Society of America B*, vol. 34, no. 7, pp. 1429–1434, 2017.
- [26] A. Weis, “Optically pumped alkali magnetometers for biomedical applications,” *Europhysics News*, vol. 43, no. 3, pp. 20–23, 2012.
- [27] I. Kominis, T. Kornack, J. Allred, and M. Romalis, “A subfemtotesla multichannel atomic magnetometer,” *Nature*, vol. 422, no. 6932, p. 596, 2003.
- [28] J. Nenonen, J. Montonen, and T. Katila, “Thermal noise in biomagnetic measurements,” *Review of Scientific Instruments*, vol. 67, no. 6, pp. 2397–2405, 1996.
- [29] T. Sander, J. Preusser, R. Mhaskar, J. Kitching, L. Trahms, and S. Knappe, “Magnetoencephalography with a chip-scale atomic magnetometer,” *Biomedical Optics Express*, vol. 3, no. 5, pp. 981–990, 2012.
- [30] R. Wyllie, M. Kauer, R. T. Wakai, and T. G. Walker, “Optical magnetometer array for fetal magnetocardiography,” *Optics Letters*, vol. 37, no. 12, pp. 2247–2249, 2012.
- [31] D. Hunter, R. Jiménez-Martínez, J. Herbsommer, S. Ramaswamy, W. Li, and E. Riis, “Waveform reconstruction with a Cs based free-induction-decay magnetometer,” *Optics Express*, vol. 26, no. 23, pp. 30 523–30 531, 2018.
- [32] Z. D. Grujić, P. A. Koss, G. Bison, and A. Weis, “A sensitive and accurate atomic magnetometer based on free spin precession,” *European Physical Journal D*, vol. 69, no. 5, p. 135, 2015.
- [33] D. Sheng, S. Li, N. Dural, and M. Romalis, “Subfemtotesla scalar atomic magnetometry using multipass cells,” *Physical Review Letters*, vol. 110, no. 16, p. 160802, 2013.
- [34] W. E. Bell and A. L. Bloom, “Optically driven spin precession,” *Physical Review Letters*, vol. 6, no. 6, p. 280, 1961.

Bibliography

- [35] S. Afach, G. Ban, G. Bison, K. Bodek, Z. Chowdhuri, Z. D. Grujić, L. Hayen, V. H elaine, M. Kasprzak, K. Kirch *et al.*, “Highly stable atomic vector magnetometer based on free spin precession,” *Optics Express*, vol. 23, no. 17, pp. 22 108–22 115, 2015.
- [36] M. Fox, *Quantum optics: an introduction*. Oxford University Press, 2006, vol. 15.
- [37] C. J. Foot, *Atomic physics*. Oxford University Press, 2005, vol. 7.
- [38] A. Borna, T. R. Carter, J. D. Goldberg, A. P. Colombo, Y.-Y. Jau, C. Berry, J. McKay, J. Stephen, M. Weisend, and P. D. Schwindt, “A 20-channel magnetoencephalography system based on optically pumped magnetometers,” *Physics in Medicine and Biology*, vol. 62, no. 23, p. 8909, 2017.
- [39] D. A. Steck, “Cesium D line data,” *available online at <http://steck.us/alkalidata>*, 2010.
- [40] P. Siddons, C. S. Adams, C. Ge, and I. G. Hughes, “Absolute absorption on rubidium D lines: comparison between theory and experiment,” *Journal of Physics B: Atomic, Molecular and Optical Physics*, vol. 41, no. 15, p. 155004, 2008.
- [41] R. Loudon, *The quantum theory of light*. Oxford University Press, 2000.
- [42] T. Udem, J. Reichert, R. Holzwarth, and T. H ansch, “Absolute optical frequency measurement of the cesium D₁ line with a mode-locked laser,” *Physical Review Letters*, vol. 82, no. 18, p. 3568, 1999.
- [43] L. Young, W. Hill III, S. Sibener, S. D. Price, C. Tanner, C. Wieman, and S. R. Leone, “Precision lifetime measurements of Cs $6p\ ^2P_{1/2}$ and $6p\ ^2P_{3/2}$ levels by single-photon counting,” *Physical Review A*, vol. 50, no. 3, p. 2174, 1994.
- [44] R. Jim enez Mart inez, “Microfabricated spin polarized atomic magnetometers,” Ph.D. dissertation, University of Colorado, 2013.
- [45] S. Appelt, A. B.-A. Baranga, C. Erickson, M. Romalis, A. Young, and W. Happer, “Theory of spin-exchange optical pumping of ^3He and ^{129}Xe ,” *Physical Review A*, vol. 58, no. 2, p. 1412, 1998.

Bibliography

- [46] J. P. McGilligan, “Micro-fabricated diffractive optics for quantum sensors and atomic clocks,” Ph.D. dissertation, University of Strathclyde, 2017.
- [47] Y. Liu, J. Lin, G. Huang, Y. Guo, and C. Duan, “Simple empirical analytical approximation to the Voigt profile,” *Journal of the Optical Society of America B*, vol. 18, no. 5, pp. 666–672, 2001.
- [48] J. J. Olivero and R. Longbothum, “Empirical fits to the Voigt line width: A brief review,” *Journal of Quantitative Spectroscopy and Radiative Transfer*, vol. 17, no. 2, pp. 233–236, 1977.
- [49] P. Miéville, S. Jannin, L. Helm, and G. Bodenhausen, “NMR of insensitive nuclei enhanced by dynamic nuclear polarization,” *Chimia-International Journal for Chemistry*, vol. 65, no. 4, p. 260, 2011.
- [50] M. Vengalattore, J. Higbie, S. Leslie, J. Guzman, L. Sadler, and D. Stamper-Kurn, “High-resolution magnetometry with a spinor Bose-Einstein condensate,” *Physical Review Letters*, vol. 98, no. 20, p. 200801, 2007.
- [51] A. Matsko, I. Novikova, M. Scully, and G. Welch, “Radiation trapping in coherent media,” *Physical Review Letters*, vol. 87, no. 13, p. 133601, 2001.
- [52] B. Lancor and T. Walker, “Effects of nitrogen quenching gas on spin-exchange optical pumping of ^3He ,” *Physical Review A*, vol. 82, no. 4, p. 043417, 2010.
- [53] T. Scholtes, S. Pustelny, S. Fritzsche, V. Schultze, R. Stolz, and H.-G. Meyer, “Suppression of spin-exchange relaxation in tilted magnetic fields within the geophysical range,” *Physical Review A*, vol. 94, no. 1, p. 013403, 2016.
- [54] T. E. Dyer and N. L. Brockie, “Vapor cell and method for making same,” May 2 2017, US Patent 9,639,062.
- [55] L.-A. Liew, J. Moreland, and V. Gerginov, “Wafer-level filling of microfabricated atomic vapor cells based on thin-film deposition and photolysis of cesium azide,” *Applied Physics Letters*, vol. 90, no. 11, p. 114106, 2007.

Bibliography

- [56] S. Woetzel, V. Schultze, R. IJsselsteijn, T. Schulz, S. Anders, R. Stolz, and H.-G. Meyer, “Microfabricated atomic vapor cell arrays for magnetic field measurements,” *Review of Scientific Instruments*, vol. 82, no. 3, p. 033111, 2011.
- [57] G. A. Pitz, D. E. Wertepny, and G. P. Perram, “Pressure broadening and shift of the cesium D₁ transition by the noble gases and N₂, H₂, HD, D₂, CH₄, C₂H₆, CF₄, and ³He,” *Physical Review A*, vol. 80, no. 6, p. 062718, 2009.
- [58] A. Andalkar and R. Warrington, “High-resolution measurement of the pressure broadening and shift of the Cs D₁ and D₂ lines by N₂ and He buffer gases,” *Physical Review A*, vol. 65, no. 3, p. 032708, 2002.
- [59] E. Bernabeu and J. Alvarez, “Shift and broadening of hyperfine components of the first doublet of cesium perturbed by foreign gases,” *Physical Review A*, vol. 22, no. 6, p. 2690, 1980.
- [60] A. Couture, T. Clegg, and B. Driehuys, “Pressure shifts and broadening of the Cs D₁ and D₂ lines by He, N₂, and Xe at densities used for optical pumping and spin exchange polarization,” *Journal of Applied Physics*, vol. 104, no. 9, p. 094912, 2008.
- [61] S. Piccolomo, “Chip-scale atomic magnetometer,” Ph.D. dissertation, University of Strathclyde, 2016.
- [62] I. Hughes and T. Hase, *Measurements and their uncertainties: a practical guide to modern error analysis*. Oxford University Press, 2010.
- [63] G. Breit and I. Rabi, “Measurement of nuclear spin,” *Physical Review*, vol. 38, no. 11, p. 2082, 1931.
- [64] H. De Freitas, M. Oria, and M. Chevrollier, “Spectroscopy of cesium atoms adsorbing and desorbing at a dielectric surface,” *Applied Physics B*, vol. 75, no. 6-7, pp. 703–709, 2002.

Bibliography

- [65] W. C. Griffith, S. Knappe, and J. Kitching, “Femtotesla atomic magnetometry in a microfabricated vapor cell,” *Optics Express*, vol. 18, no. 26, pp. 27 167–27 172, 2010.
- [66] W. Franzen, “Spin relaxation of optically aligned rubidium vapor,” *Physical Review*, vol. 115, no. 4, p. 850, 1959.
- [67] F. Franz and C. Volk, “Electronic spin relaxation of the $4^2S_{1/2}$ state of K induced by K-He and K-Ne collisions,” *Physical Review A*, vol. 26, no. 1, p. 85, 1982.
- [68] T. Scholtes, S. Woetzel, R. IJsselsteijn, V. Schultze, and H.-G. Meyer, “Intrinsic relaxation rates of polarized Cs vapor in miniaturized cells,” *Applied Physics B*, vol. 117, no. 1, pp. 211–218, 2014.
- [69] S. Appelt, A. B.-A. Baranga, A. Young, and W. Happer, “Light narrowing of rubidium magnetic-resonance lines in high-pressure optical-pumping cells,” *Physical Review A*, vol. 59, no. 3, p. 2078, 1999.
- [70] T. Scholtes, V. Schultze, R. IJsselsteijn, S. Woetzel, and H.-G. Meyer, “Light-narrowed optically pumped M_x magnetometer with a miniaturized Cs cell,” *Physical Review A*, vol. 84, no. 4, p. 043416, 2011.
- [71] R. Kawabata, K. Fukuda, and A. Kandori, “Improvement of an optically pumped magnetometer using a combination of D_1 and D_2 transitions,” *Japanese Journal of Applied Physics*, vol. 51, no. 8R, p. 082404, 2012.
- [72] V. Schultze, T. Scholtes, R. IJsselsteijn, and H.-G. Meyer, “Improving the sensitivity of optically pumped magnetometers by hyperfine repumping,” *Journal of the Optical Society of America B*, vol. 32, no. 5, pp. 730–736, 2015.
- [73] S. Groeger, G. Bison, and A. Weis, “An improved laser pumped cesium magnetometer using hyperfine repumping,” in *Quantum Electronics Conference, 2005. EQEC'05. European*. IEEE, 2005, p. 199.
- [74] H. G. Dehmelt, “Modulation of a light beam by precessing absorbing atoms,” *Physical Review*, vol. 105, no. 6, p. 1924, 1957.

Bibliography

- [75] N. E. Jacobsen, *NMR spectroscopy explained: simplified theory, applications and examples for organic chemistry and structural biology*. John Wiley & Sons, 2007.
- [76] S. Colombo, V. Dolgovskiy, T. Scholtes, Z. D. Grujić, V. Lebedev, and A. Weis, “Orientational dependence of optically detected magnetic resonance signals in laser-driven atomic magnetometers,” *Applied Physics B*, vol. 123, no. 1, p. 35, 2017.
- [77] W. Happer, “Optical pumping,” *Reviews of Modern Physics*, vol. 44, no. 2, p. 169, 1972.
- [78] E. W. Weisstein, “Discrete fourier transform,” 2004, MathWorld—a Wolfram web resource.
- [79] S. Rochester and D. Budker, “Atomic polarization visualized,” *American Journal of Physics*, vol. 69, no. 4, pp. 450–454, 2001.
- [80] M. Auzinsh, D. Budker, and S. Rochester, *Optically polarized atoms: understanding light-atom interactions*. Oxford University Press, 2010.
- [81] A. Moschitta and P. Carbone, “Cramér–Rao lower bound for parametric estimation of quantized sinewaves,” *IEEE Transactions on Instrumentation and Measurement*, vol. 56, no. 3, pp. 975–982, 2007.
- [82] Y.-X. Yao and S. M. Pandit, “Cramér–Rao lower bounds for a damped sinusoidal process,” *IEEE Transactions on Signal Processing*, vol. 43, no. 4, pp. 878–885, 1995.
- [83] C. Gemmel, W. Heil, S. Karpuk, K. Lenz, C. Ludwig, Y. Sobolev, K. Tullney, M. Burghoff, W. Kilian, S. Knappe-Grüneberg *et al.*, “Ultra-sensitive magnetometry based on free precession of nuclear spins,” *The European Physical Journal D*, vol. 57, no. 3, pp. 303–320, 2010.
- [84] T. Addabbo, R. Biondi, S. Cioncolini, A. Fort, F. Rossetti, and V. Vignoli, “A zero-crossing detection system based on FPGA to measure the angular vibrations

Bibliography

- of rotating shafts,” *IEEE Transactions on Instrumentation and Measurement*, vol. 63, no. 12, pp. 3002–3010, 2014.
- [85] P. Royer del Barrio, M. Á. Sánchez Marcos, M. López Vallejo, and C. A. López Barrio, “Area-efficient linear regression architecture for real-time signal processing on FPGAs,” in *Proceedings of 26th Conference on Design of Circuits and Integrated Systems*, 2011.
- [86] J. G. Proakis, *Digital signal processing: principles algorithms and applications*. Pearson Education India, 2001.
- [87] R. Aghazadeh, H. Lesani, M. Sanaye-Pasand, and B. Ganji, “New technique for frequency and amplitude estimation of power system signals,” *IEE Proceedings-Generation, Transmission and Distribution*, vol. 152, no. 3, pp. 435–440, 2005.
- [88] V. Shah and M. Romalis, “Spin-exchange relaxation-free magnetometry using elliptically polarized light,” *Physical Review A*, vol. 80, no. 1, p. 013416, 2009.
- [89] B. H. McGuyer, Y.-Y. Jau, and W. Happer, “Method for suppressing light shift in optical pumping systems,” Nov. 2 2010, US Patent 7,825,736.
- [90] B. Mathur, H. Tang, and W. Happer, “Light shifts in the alkali atoms,” *Physical Review*, vol. 171, no. 1, p. 11, 1968.
- [91] G. Bao, A. Wickenbrock, S. Rochester, W. Zhang, and D. Budker, “Suppression of the nonlinear Zeeman effect and heading error in earth-field-range alkali-vapor magnetometers,” *Physical Review Letters*, vol. 120, no. 3, p. 033202, 2018.
- [92] S. Seltzer, P. Meares, and M. Romalis, “Synchronous optical pumping of quantum revival beats for atomic magnetometry,” *Physical Review A*, vol. 75, no. 5, p. 051407, 2007.
- [93] S. Afach, C. A. Baker, G. Ban, G. Bison, K. Bodek, Z. Chowdhuri, M. Daum, M. Fertl, B. Franke, P. Geltenbort *et al.*, “Measurement of a false electric dipole moment signal from ^{199}Hg atoms exposed to an inhomogeneous magnetic field,” *The European Physical Journal D*, vol. 69, no. 10, p. 225, 2015.

Bibliography

- [94] H. Korsch, A. Klumpp, and D. Witthaut, “On two-dimensional Bessel functions,” *Journal of Physics A*, vol. 39, no. 48, p. 14947, 2006.
- [95] M. Shuker, O. Firstenberg, Y. Sagi, A. Ben-Kish, N. Davidson, and A. Ron, “Ramsey-like measurement of the decoherence rate between Zeeman sublevels,” *Physical Review A*, vol. 78, no. 6, p. 063818, 2008.
- [96] H.-L. Ke, P.-X. Miao, S.-Y. Yang, J.-H. Tu, J. Hao, L.-L. Zhu, B. Yang, J. Wang, W. Yang, J.-Z. Cui *et al.*, “Temperature dependent relaxation lifetime T_1 , T_2 measurements of the spin-polarized ^{87}Rb atoms,” *Optik*, vol. 180, pp. 517–525, 2019.
- [97] K. Jensen, V. Acosta, J. Higbie, M. Ledbetter, S. Rochester, and D. Budker, “Cancellation of nonlinear Zeeman shifts with light shifts,” *Physical Review A*, vol. 79, no. 2, p. 023406, 2009.
- [98] D. F. J. Kimball, J. Dudley, Y. Li, and D. Patel, “In situ measurement of light polarization with ellipticity-induced nonlinear magneto-optical rotation,” *Physical Review A*, vol. 96, no. 3, p. 033823, 2017.
- [99] K. Kim, S. Begus, H. Xia, S.-K. Lee, V. Jazbinsek, Z. Trontelj, and M. V. Romalis, “Multi-channel atomic magnetometer for magnetoencephalography: A configuration study,” *NeuroImage*, vol. 89, pp. 143–151, 2014.
- [100] A. P. Colombo, T. R. Carter, A. Borna, Y.-Y. Jau, C. N. Johnson, A. L. Dagle, and P. D. Schwindt, “Four-channel optically pumped atomic magnetometer for magnetoencephalography,” *Optics Express*, vol. 24, no. 14, pp. 15 403–15 416, 2016.
- [101] G. Bison, “Development of an optical cardio-magnetometer,” Ph.D. dissertation, Université de Fribourg, 2004.
- [102] V. Shah and J. Kitching, “Advances in coherent population trapping for atomic clocks,” in *Advances in Atomic, Molecular, and Optical Physics*. Elsevier, 2010, vol. 59, pp. 21–74.

Bibliography

- [103] J. Kitching, S. Knappe, and E. A. Donley, “Atomic sensors—a review,” *IEEE Sensors Journal*, vol. 11, no. 9, pp. 1749–1758, 2011.
- [104] C. Alcock, V. Itkin, and M. Horrigan, “Vapour pressure equations for the metallic elements: 298–2500K,” *Canadian Metallurgical Quarterly*, vol. 23, no. 3, pp. 309–313, 1984.